ACCURACY ASSESSMENT OF POLAR MOTION AND UNIVERSAL TIME (UT1) OBSERVED BY VLBI AT SUB-DIURNAL PERIODS

VLBI İLE GÜN-İÇİ PERİYOTLARDA İZLENEN KUTUP GEZİNMESİ VE EVRENSEL ZAMANIN (UT1) DOĞRULUK DEĞERLENDİRMESİ

MEHMET FİKRET ÖCAL

ASSIST. PROF. DR. KAMİL TEKE

Supervisor

Submitted to
Graduate School of Science and Engineering of Hacettepe University
as a Partial Fulfilment to the Requirements
for the Award of the Degree of Master of Science
in Geomatics Engineering

2019

This work titled "**Accuracy Assessment of Polar Motion and Universal Time (UT1) Observed by VLBI at Sub-diurnal Periods**" by **MEHMET FİKRET ÖCAL** has been approved as a thesis for the Degree of **Master of Science in Geomatics Engineering** by the Examining Committee Members mentioned below.

Prof. Dr. Mualla YALÇINKAYA
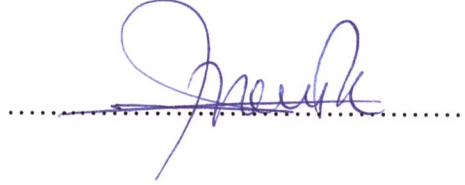
Head

Assist. Prof. Dr. Kamil TEKE

Supervisor

Prof. Dr. Bahadır AKTUĞ

Member

Assist. Prof. Dr. Metin NOHUTCU

Member

Assist. Prof. Dr. Gonca OKAY AHİ

Member

This thesis has been approved as a thesis for the Degree of **Master of Science in Geomatics Engineering** by Board of Directors of the Institute of Graduate School of Science and Engineering on ...... / ..... /.......

Prof. Dr. Menemşe GÜMÜŞDERELİOĞLU

Director of the Institute of

Graduate School of Science and Engineering

To Bâde . . .

ETHICS

In this thesis study, prepared in accordance with the spelling rules of Institute of Graduate School of Science and Engineering of Hacettepe University,

I declare that

- all the information and documents have been obtained in the base of the academic rules

- all audio-visual and written information and results have been presented according to the rules of scientific ethics

- in case of using others works, related studies have been cited in accordance with the scientific standards

- all cited studies have been fully referenced

- I did not do any distortion in the data set

- and any part of this thesis has not been presented as another thesis study at this or any other university.

31/05/2019

MEHMET FİKRET ÖCAL

YAYINLANMA VE FİKRİ MÜLKİYET HAKLARI BEYANI

Enstitü tarafından onaylanan lisansüstü tezimin/raporumun tamamını veya herhangi bir kısmını, basılı (kağıt) ve elektronik formatta arşivleme ve aşağıda verilen koşullarla kullanıma açma iznini Hacettepe üniversitesine verdiğimi bildiririm. Bu izinle Üniversiteye verilen kullanım hakları dışındaki tüm fikri mülkiyet haklarım bende kalacak, tezimin tamamının ya da bir bölümünün gelecekteki çalışmalarda (makale, kitap, lisans ve patent vb.) kullanım hakları bana ait olacaktır.

Tezin kendi orijinal çalışmam olduğunu, başkalarının haklarını ihlal etmediğimi ve tezimin tek yetkili sahibi olduğumu beyan ve taahhüt ederim. Tezimde yer alan telif hakkı bulunan ve sahiplerinden yazılı izin alınarak kullanması zorunlu metinlerin yazılı izin alarak kullandığımı ve istenildiğinde suretlerini Üniversiteye teslim etmeyi taahhüt ederim.

Yükseköğretim Kurulu tarafından yayınlanan *"Lisansüstü Tezlerin Elektronik Ortamda Toplanması, Düzenlenmesi ve Erişime Açılmasına İlişkin Yönerge"* kapsamında tezim aşağıda belirtilen koşullar haricince YÖK Ulusal Tez Merkezi / H. Ü. Kütüphaneleri Açık Erişim Sisteminde erişime açılır.

- ☐ Enstitü / Fakülte yönetim kurulu kararı ile tezimin erişime açılması mezuniyet tarihimden itibaren 2 yıl ertelenmiştir.

- ☐ Enstitü / Fakülte yönetim kurulu gerekçeli kararı ile tezimin erişime açılması mezuniyet tarihimden itibaren .... ay ertelenmiştir.

- ☐ Tezim ile ilgili gizlilik kararı verilmiştir.

31/05/2019

MEHMET FİKRET ÖCAL

ABSTRACT

ACCURACY ASSESSMENT OF POLAR MOTION AND UNIVERSAL TIME (UT1) OBSERVED BY VLBI AT SUB-DIURNAL PERIODS

Mehmet Fikret ÖCAL

Master of Science, Department of Geomatics Engineering
Supervisor: Assist. Prof. Dr. Kamil TEKE
May 2019, 138 pages

Earth rotation parameters (ERP): polar motion coordinates and Universal Time (UT1) have a significant impact basically on the terrestrial and celestial reference system relations, orbit determination, and deep-space navigation. Very Long Baseline Interferometry (VLBI) is the only space-based geodetic technique that can monitor both Earth rotation parameters and nutation offsets simultaneously. International VLBI Service for Geodesy and Astrometry (IVS) organizes VLBI observations for 1-2 hours or 24 hours called as Intensive or Standard sessions, respectively. Intensive sessions are carried out for UT1 determination only by 2-3 VLBI stations on a daily basis. However, Standard sessions, that are suitable for monitoring Earth rotation parameters, are performed by 5-8 VLBI stations twice a week. IVS suggests a parametrization for UT1 determination from the analysis of Intensive sessions that contain 15-55 observations. In fact, the estimation of the tropospheric delay in short time intervals during the Intensive session analysis is not possible due to few observations. In order to increase the accuracy of UT1 determination from the analysis of the Intensive sessions, troposphere signal delays and troposphere gradients derived from the analysis of the Global Navigation Satellite Systems (GNSS) observations are involved in the analysis of the VLBI Intensive sessions between 2008 and 2018 in this study. Statistical comparisons show that length-of-day (LOD) values obtained from the proposed analysis strategies of this thesis (NewUT1) are 2-3μs/day more accurate than those of IVS standard analysis. NewUT1 series are daily updated at Hacettepe University servers for the use of researchers globally. On the other hand, the major reason for ERP variations at semi-diurnal and diurnal periods is ocean tides. International Earth Rotation and Reference System Service (IERS) recommended a model for predicting these variations derived from geodynamical models nearly twenty-five

years ago. However, the International Association for Geodesy (IAG) propounded the necessity for the development of a new model based on the state-of-the-art space/satellite geodetic techniques. For this reason, the other research objective of this thesis is modeling the sub-daily ERP variations due to ocean tides by analyzing the VLBI Standard sessions between 2000 and 2018. For this purpose, time series of ERP are decomposed into sine and cosine functions at tidal periods using least squares (LS), singular value decomposition (SVD), and complex demodulation (CD) solution methods. Estimated tidal amplitudes from different solution methods are compared with those of IERS model and also between each other using the metrics of phasors, Fourier transform, and time series. Amplitudes estimated from least squares method have the best agreement with those of IERS recommended model. Furthermore, tidal amplitude estimation software with a graphical user interface called TIDEST is developed in the MATLAB environment in order to provide easy-use for the estimation of tidal amplitudes from ERP time series within the study.

ÖZET

VLBI İLE GÜN-İÇİ PERİYOTLARDA İZLENEN KUTUP GEZİNMESİ VE EVRENSEL ZAMANIN (UT1) DOĞRULUK DEĞERLENDİRMESİ

Mehmet Fikret ÖCAL

Yüksek Lisans, Geomatik Mühendisliği Bölümü
Tez Danışmanı: Dr. Öğr. Üyesi Kamil TEKE
Mayıs 2019, 138 sayfa

Kutup gezinmesi koordinatları ve Evrensel Zamanı (UT1) içeren Yer dönme parametreleri (ERP), temel olarak yersel ve göksel referans sistemleri arasındaki ilişki, yörünge belirleme ve derin-uzay navigasyonu üzerinde önemli bir etkiye sahiptir. Çok Uzun Baz Enterferometresi (VLBI) hem Yer dönme parametreleri hem de nutasyon ofsetlerini eş zamanlı izleyebilen tek uzay-tabanlı jeodezik tekniktir. Uluslararası Jeodezi ve Astrometri için VLBI Servisi (IVS) 1-2 saatlik veya 24 saatlik, sırasıyla yoğun ve standart oturumlar adı verilen, VLBI gözlemlerini organize eder. Yoğun oturumlar UT1 belirlenmesi amacıyla 2-3 VLBI istasyonu ile günlük olarak gerçekleştirilirler. Bununla birlikte, Yer dönme parametreleri'nin izlenmesine uygun olan standart oturumlar, 5-8 VLBI istasyonu ile haftada iki defa icra edilirler. IVS, 15-55 gözlem içeren yoğun oturumların analizinden UT1 belirlenmesi için bir analiz parametrizasyonu önermiştir. Esasen yoğun oturumların analizi sırasında troposfer gecikmeleri'nin kısa zaman aralıklarında kestirimi az sayıda ölçü olması sebebiyle mümkün değildir. Bu çalışma kapsamında, yoğun oturumların analizinden UT1 belirleme doğruluğunun artırılabilmesi için, Küresel Navigasyon Uydu Sistemleri (GNSS) gözlemlerinin analizinden elde edilen troposfer sinyal gecikmeleri ve troposfer gradyanlarının 2008-2018 yılları arasındaki VLBI yoğun oturumlarının analizlerine dahil edilmiştir. İstatistiksel karşılaştırmalar, bu tezde önerilen analiz stratejisi ile elde edilen gün-uzunluğu (LOD) değerlerinin (YeniUT1), IVS standart analizindekilere göre 2-3μs/gün daha doğru olduğunu göstermiştir. YeniUT1 serileri, Hacettepe Üniversitesi sunucularında dünya çapındaki araştırmacıların kullanımı için günlük olarak güncellenmektedir. Diğer yandan, ERP'nin yarı-günlük ve günlük periyotlardaki değişimlerin en büyük sebebi okyanus gel-gitleridir. Uluslararası

Yer Dönme ve Referans Sistemleri Servisi (IERS) bu değişim- lerin tahmin edilmesi için, yirmibeş yıl önce jeodinamik modellerden türetilen bir model önermiştir. Fakat, Uluslararası Jeodezi Birliği (IAG) modern uzay/uydu jeodezisi tekniklerine dayanan yeni bir model geliştirilmesinin gerekliliğini ileri sürmüştür. Bu sebeple, bu tezin diğer bir hedefi, okyanus gel-gitleri kaynaklı gün-içi, ERP değişimlerini 2000-2018 yılları arasındaki VLBI standart oturumlarının anali ile modellenmesidir. Bu amaçla, ERP zaman serileri, en küçük kareler (LS), tekil değer ayrışımı (SVD) ve kompleks demodülasyon (CD) çözüm metodları kullanılarak gel-gitsel periyotlardaki sinüs ve kosinüs fonksiyonlarına ayrıştırılmıştır. Farklı metodlar ile kestirilen gel-gitsel genlikler, IERS modeli genlikleri ve birbirleri arasında, fazör, Fourier transformu ve zaman serileri metrikleri ile karşılaştırılmıştır. En küçük kareler metodu ile kestirilen genlikler, IERS önerilen modelininkileri ile en iyi uyuma sahiptir. Buna ek olarak, ERP zaman serilerinden gel-gitsel genlik kestirimi için TIDEST adı verilen, bir grafik kullanıcı arayüzü ile gel-gitsel genlik kestirimi yazılımı, bu çalışma kapsamında MATLAB ortamında geliştirilmiştir.

ACKNOWLEDGEMENTS

Mehmet Fikret ÖCAL
May 2019, Ankara

CONTENTS

LIST OF TABLES

LIST OF FIGURES

LIST OF ABBREVIATIONS

ANTEX . . . . Antenna Exchange Format

ARP . . . . Antenna Reference Point

BCRS . . . . Barycentric Celestial Reference System

BPSK . . . . Binary Phase Shift Keying

CD . . . . Complex Demodulation

CDDIS . . . . Crustal Dynamics Data Information System

CDMA . . . . Code Division Multiple Access

CEP . . . . Celestial Ephemeris Pole

CIO . . . . Celestial Intermediate Origin

CIP . . . . Celestial Intermediate Pole

CIRS . . . . Celestial Intermediate Reference System

CODE . . . . Center for Orbit Determination in Europe

CONT . . . . Continuous VLBI Campaign

CRF . . . . Celestial Reference Frame

CRS . . . . Celestial Reference System

CTP . . . . Conventional Terrestrial Pole

DCB . . . . Differential Code Bias

DORIS . . . . Doppler Orbitography and Radiopositioning Integrated by Satellite

ECEF . . . . Earth-centered Earth-fixed

ECMWF . . . . . . European Centre for Medium-Range Weather Forecasts

EOP . . . . Earth Orientation Parameters

ERA . . . . Earth Rotation Angle

ERP . . . . Earth Rotation Parameters

ESA . . . . European Space Agency

ESOC . . . . European Space Operations Centre

FDMA . . . . Frequency Division Multiple Access

FES . . . . Finite Element Solution

FTP . . . . File Transfer Protocol

GAST . . . . Greenwich Apparent Sidereal Time

GCRS . . . . Geocentric Celestial Reference System

GLONASS .... Globalnaya Navigatsionnaya Sputnikovaya Sistema (Global Navigation Satellite Systems)

GMF .... Global Mapping Function

GMST .... Greenwich Mean Sidereal Time

GNSS .... Global Navigation Satellite Systems

GPS .... Global Positioning System

GRT .... General Relativity Theory

IAG .... International Association of Geodesy

IAU .... International Astronomical Union

ICRF .... International Celestial Reference Frame

ICRS .... International Celestial Reference System

IERS .... International Earth Rotation and Reference Systems Service

IGS .... International GNSS Service

IMF .... Isobaric Mapping Function

INT .... Intensive Sessions

ITRF .... International Terrestrial Reference Frame

ITRS .... International Terrestrial Reference System

IVS .... International VLBI Service for Geodesy and Astrometry

J2000.0 .... 2000 January 1d 12h, called as standart or fundamental epoch

JPL .... Jet Propulsion Laboratory

LLR .... Lunar Laser Ranging

LOD .... Length of Day

LS .... Least Squares

MF .... Mapping Function

MJD .... Modified Julian Date

NASA .... National Aeronautics and Space Administration

NGS .... National Geodetic Survey

NMF .... Niell Mapping Function

NNR .... No Net Rotation

NNS .... No Net Scale

NNT .... No Net Translation

NOAA .... National Oceanic and Atmospheric Administration

NRO .... Non-rotating Origin

NMW .... Numerical Weather Model

OTL .... Ocean Tidal Loading

PCO .... Phase Center Offset

PCV .... Phase Center Variations

PPP .... Precise Point Positioning

PWLO .... Piece-wise Linear Offset

SINEX .... Solution Independent Exchange Format

SLR .... Satellite Laser Ranging

SNR .... Signal to Noise Ratio

STEC .... Slant Total Electron Content

SVD .... Singular Value Decomposition

TAI .... International Atomic Time

TCB .... Barycentric Coordinate Time

TDT .... Terrestrial Dynamic Time

TIDEST .... Tidal Constituent Estimation Software

TIO .... Terrestrial Intermediate Origin

TIRS .... Terrestrial Intermediate Reference System

TRF .... Terrestrial Reference Frame

TRS .... Terrestrial Reference System

TT .... Terrestrial Time

USNO .... United States Naval Observatory

UT .... Universal Time

UTC .... Universal Time Coordinated

VieVS .... Vienna VLBI and Satellite Software

VLBI .... Very Long Baseline Interferometry

VMF .... Vienna Mapping Function

WM .... Weighted Mean

WRMS .... Weighted Root Mean Square

ZHD .... Zenith Hydrostatic Delay

ZTD .... Zenith Total Delay

ZWD .... Zenith Wet Delay

1. INTRODUCTION

1.1. Background

The relation between Earth-fixed, equatorial, three-dimensional, Cartesian coordinate system (terrestrial reference system, TRS, e.g. Altamimi et al. 2016) and space-fixed, equatorial, three-dimensional, Cartesian coordinate system (celestial reference system, CRS, e.g. Fey, Gordon and Jacobs 2009) are expressed using Earth orientation parameters (EOP). These parameters are polar motion coordinates (x_p, y_p), nutation offsets (X, Y), and $\Delta UT1$. Polar motion coordinates are the positions of celestial intermediate pole (CIP) in a crust-fixed coordinate system. On the other hand, nutation offsets indicate space-fixed coordinates of CIP. Lastly, $\Delta UT1 = UT1 - UTC$ is described as a daily, absolute phase angle of the Earth rotation w.r.t. space about CIP. Furthermore, polar motion coordinates and $\Delta UT1$ are all named as Earth rotation parameters (ERP). The Earth orientation parameters are required for the determination of the orbital motion of satellites and planets, and studies related to deep space navigation, and positioning. Thus, precise determination of these parameters ensures a notable impact on research fields of space and Earth sciences.

International Earth Rotation and Reference System Service (IERS) is responsible for monitoring EOP. Polar motion coordinates are provided by the International services of the Global Navigation Satellite Systems (GNSS), Satellite/Lunar Laser Ranging (SLR/LLR), Doppler Orbitography and Radiopositioning Integrated by Satellite (DORIS), and Very Long Baseline Interferometry (VLBI) to the IERS. Earth orientation center (EOC) of IERS updates Earth rotation parameter series (e.g. IERS 14 C04, Bizouard et al. 2018) achieved from inter-technique combinations of daily or weekly normal equation systems of all space geodetic techniques.

Several important studies focusing on modeling and theory of ERP may be given as Yoder, Williams and Parke (1981); Wahr and Bergen (1986); Moritz and Mueller (1987); Chao et al. (1991); Ray et al. (1994); Kantha, Stewart and Desai (1998); Defraigne and Smits (1999); Gross (2009) in chronological order. They presented that Earth rotation parameters are oscillating because of fluctuations of the Earth's angular momentum on account of the tidal movements of Earth's fluid envelope i.e. oceans and atmosphere. Furthermore, estimations of the EOP from GNSS and VLBI observations carried out by Robertson et al. (1985); Rothacher et al. (1999); Sovers, Fanselow and Jacobs (1998); Steigenberger et al. (2011) show that the estimation errors of these parameters are about 100-150 μas and 5-10 μs, for polar motion and UT1-UTC, respectively.

VLBI (Schuh and Behrend, 2012) observes radio-waves emitted from distant galaxies (5-7 billion light years away from our galaxy) so-called quasars (quasi-stellar radio sources). Details about the observation model of this technique may be found in Sovers, Fanselow and Jacobs (1998); Teke et al. (2012); Schuh and Böhm (2013). VLBI is fundamental and unique space geodetic technique that can monitor the full set of EOP simultaneously. In other words, monitoring long term variations of $\Delta UT1$ and nutation offsets can only be performed via the VLBI technique. Because of the high correlation between GNSS satellite orbital parameters with these parameters, GNSS technique could not be used for determination of $\Delta UT1$ and nutation offsets (Rothacher et al., 1999). However, besides VLBI, Length-of-Day (LOD), which is a derivative of $\Delta UT1$ w.r.t. time, can be monitored by GNSS, SLR/LLR, and DORIS. International VLBI Service for Geodesy and Astrometry (IVS, Schuh and Behrend 2009) is organizing VLBI observations for 1 to 2 hours long named as Intensive sessions, 24-hours Standard sessions (rapid turn-around), and 24-hours long, 15-days continuously campaigns (CONT). Due to the fact that $\Delta UT1$ is the most rapidly changing parameter among EOP (Luzum and Nothnagel, 2010), VLBI Intensive sessions containing 15-55 observations are carried out for monitoring UT1 on a daily basis. Besides, 24-hours Standard VLBI sessions are performed for every Mondays and Thursdays and suitable for ERP determination. Additionally, CONT campaigns are carried out for discovering the cutting edge VLBI observations.

1.2. Research Objectives

This thesis comprises two major research objectives. First one is to increase Universal Time (UT1) estimation accuracy of the VLBI Intensive sessions by incorporating troposphere signal delays estimated from GNSS PPP method into the analysis as suggested by Teke et al. (2015). The troposphere is one of the largest and rapidly changing error sources in the space geodetic techniques' observations. For several geodetic observatory sites, VLBI and GNSS receivers are co-located. The International GNSS Service (IGS, Dow, Neilan and Rizos 2009) is offering troposphere zenith signal delays and troposphere gradients derived from GNSS observations in 5-min intervals for every day. Using this troposphere delay obtained from co-located GNSS stations in the analysis of the VLBI Intensive sessions would expected to increase the accuracy of UT1 determination owing to the lack of observations in the Intensive sessions. Duration of the observation is limiting factor for the estimation accuracy of Intensive sessions. In other words, as the number of estimated parameters increases, the estimation accuracy of particular parameters would be decreased for these sessions with fewer observations. In addition to this, for the parameter estimation of VLBI observation, choosing a priori values of the estimated parameters properly has a significant effect on the estimation accuracy of the parameters. Thus, reduction of GNSS derived troposphere delays

and gradients from VLBI observations in the analysis would increase the determination accuracy of the UT1. The latency of the IGS troposphere products is approximately 3-weeks. In order to decrease this latency to a few days, similar troposphere products are derived from GNSS PPP solutions using Bernese GNSS Software (Dach et al., 2015) in the context of this thesis.

The second objective of this thesis is exhibiting an alternative and better model for the high-frequency (sub-daily) Earth rotation parameter variations caused by ocean tides as a replacement of IERS 2010 recommended model. The major reason for sub-daily ERP variations is ocean tides (Moritz and Mueller, 1987). IERS 2010 conventions (Petit and Luzum, 2010) presents a sub-daily ERP variations model that is used as a priori values of ERP consisting of 41 diurnal and 30 semi-diurnal tidal constituents. This model was put forward by Ray et al. (1994) using ocean dynamics in the absence of state-of-the-art space/satellite geodetic techniques. International Association of Geodesy (IAG) recommended replacing this model using modern techniques, while several works exhibit discrepancy of the model such as Nilsson, Böhm and Schuh (2010); Artz et al. (2010) from VLBI observations and Rothacher et al. (2001); Desai and Sibois (2016) from GNSS observations. These works were performed using least squares technique so as to find amplitudes of tidal constituents. On the other hand, Böhm, Brzeziński and Schuh (2012) estimated the model amplitudes using complex demodulation method. Similar to the least squares, singular value decomposition is considered to be used in the estimation of these amplitudes. Consequently, the second aim of this thesis is to produce a better sub-daily ERP variations model as a replacement of the IERS recommended model using these three parameter estimation techniques individually. That would give a chance to compare the methods with each other. Besides, a software with a graphical user interface, that is capable for estimating such a model from ERP time series using these three parameter estimation methods, was designed in the MATLAB environment as another output of this thesis.

1.3. Thesis Outline

This thesis composed of nine chapters.

Chapter 2 briefly describes time and space reference systems, the transformation between space reference systems i.e. ITRF and GCRS based on two different conventions of IAU, and variations in the Earth's rotation. This chapter establishes a foundation for the thesis outline.

Chapter 3 consists least squares parameter estimation method used in space/satellite geodetic

techniques as well as constraining parameters, free network solution and global solution. Moreover, brief foundations for parameter estimation methods proposed for tidal constituent estimation from time series of Earth rotation parameters such as complex demodulation and singular value decomposition are presented.

Chapter 4 is related to troposphere delay modeling. In this chapter, radio-wave propagation in the neutral part of the atmosphere is introduced in detail in addition to various troposphere mapping functions, and azimuthal asymmetric troposphere delay modeling.

Chapter 5 describes the Global Navigation Satellite Systems measurement principles solely specific to GPS and GLONASS systems. Additionally, the precise point positioning technique (PPP) that is used for the troposphere delay estimation in this thesis, and PPP error correction strategies are explained. Harmonic and linear motions of crust fixed points is also introduced in this chapter.

Chapter 6 introduces observing models and data analysis of the Very Long Baseline Interferometry technique which is the fundamental space geodetic technique in the content of this thesis. Basic delay model, gravitational, vacuum and geometric delays are described in particular. Partial differentiation of the VLBI observation model w.r.t. the Earth orientation parameters are also provided.

Chapter 7 presents the methodology and results of first research objective of this thesis as increasing UT1 estimation accuracy of VLBI Intensive sessions via using GNSS troposphere delays. Troposphere delay estimation from GNSS PPP technique using Bernese Software is also presented.

Chapter 8 covers the methodology and results of the second research objective of this thesis which aims estimation of tidal constituents of the ocean tides caused Earth's rotation variations in sub-daily periods model from VLBI observations spread about 18 years of data from the beginning of the 2000 till the end of 2018. Besides, tidal estimation software called as TIDEST developed in this thesis work is explained in details.

Chapter 9 is the conclusions chapter that discuss the outcomes of two different research objectives, final thought, and proposed future works.

2. EARTH ROTATION

2.1. Time Reference Systems

Accurate time references are important for GNSS as well as VLBI space geodetic techniques due to their measurements of the signal travel time. In the ancient centuries, the only motion of the Sun was used for time referencing. Nevertheless, time scales have become more sophisticated, precise, well-defined and uniform as a result of technological progress. Operational time references are given in Table (2.1). These are based on several periodic processes related to celestial mechanics, Earth's rotation, and atomic oscillations (Sanz Subirana, Juan Zornoza and Hernández-Pajares, 2013).

Table 2.1: Operational time systems.

Periodic Process	Time
Earth's rotation	Universal Time (UT0, UT1, UT2, UTR, UTS)
	Greenwich Sidereal Time (Θ)
Atomic oscillators	International Atomic Time (TAI)
	Coordinated Universal Time (UTC)
	GNSS Reference Time
Relativity considered	Terrestrial Dynamic Time (TDT)
	Barycentric Dynamic Time (TDB)

2.1.1. Sidereal Time Systems

The Earth's rotation w.r.t. the Sun or the stars is a measure of time. Sidereal time is the hour angle belongs to the vernal equinox in the celestial frame (McCarthy and Seidelmann, 2009). However, nutation and precession lead to move of the vernal equinox. Thus, sidereal time is not an exact measure of the rotation of the Earth. Figure (2.1) shows sidereal time systems. Sidereal times are measured w.r.t. either the true vernal equinox or the mean vernal equinox. True vernal equinox is the intersection of the true ecliptic and the true equator at the date. Apparent sidereal time is effected by both nutation and precession as periodic variations due to motion of the true equinox at the observation epoch. However, mean vernal equinox is only under influence of precession.
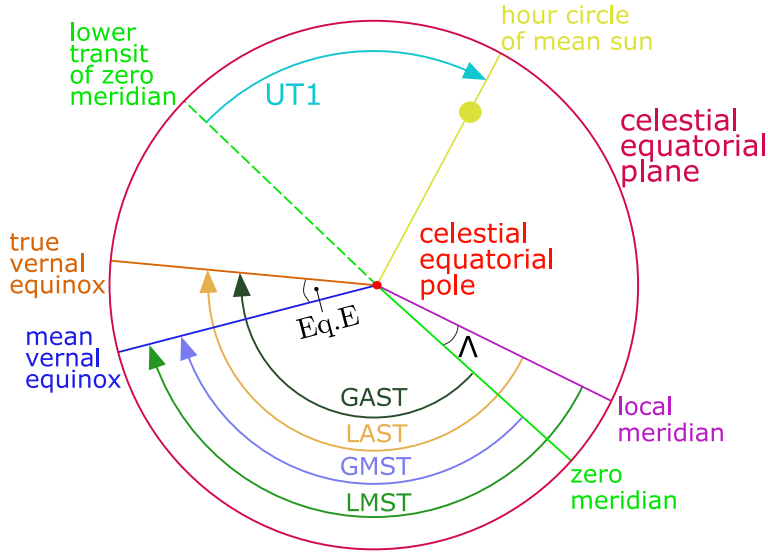
- GAST (Θ_G): Greenwich Apparent (True) Sidereal Time

- LAST: Local Apparent (True) Sidereal Time

- GMST (θ_G): Greenwich Mean Sidereal Time

- LMST: Local Mean Sidereal Time

- Eq.E: Equation of Equinox

- Λ: East longitude of local observer

Figure 2.1: Illustration of sidereal time scales.

Time passing between two sequenced transits of the equinox is called a sidereal day. However, solar (universal) time is measured w.r.t. the Sun. Hence, the solar day is longer compared to the sidereal day by approximately $3^m56.^s4$ based on Earth's orbital motion for the one-day duration. In fact, universal time (UT0) is measured as hour angle along the celestial equator from the lower transit of the Greenwich meridian to the hour circle of the mean Sun using optical astronomical techniques without considering polar motion corrections. Either sidereal or solar time is not uniform because of the variable Earth's angular velocity. Tidal excitation on Earth mass balance results in fluctuations of these time scales. For this reason, UT0 is not usable for modern applications due to its low accuracy. Besides, UT1 is improved and widely used types of universal time defined as daily absolute rotation phase angle of the Earth w.r.t. space around the celestial intermediate pole (CIP) determined using VLBI (Schuh and Behrend, 2012) space geodetic technique considering polar motion. UT2, UTR, and UTS are achieved via reducing zonal tidal harmonics on periods of seasons, less than 35-days, and between 5-days and 18.6 years from UT1, respectively. UT1 is used for space-based navigation and positioning purposes due to the fact that UT1 is one of the five Earth orientation parameters (EOP) that define the kinematic relation between terrestrial and celestial reference frames. The conversion between universal time (UT1) and Greenwich mean sidereal time (GMST) may be performed as given below (Seeber, 2003)

$$
\begin{aligned}
\theta_G = \ & 1.0027379093 \, UT1 + 6^h41^m50^s.54841 \\
+ \ & 8640184^s.812866 \, T_u + 0^s.093104 \, T_u^2 - 6^s.2 \times 10^{-6} \, T_u^3
\end{aligned}
\tag{2.1}
$$

where T_u is time span in Julian centuries from the fundamental epoch (J2000.0) to the ob-

servation day at 0^h UT (Seidelmann, 1992).

2.1.2. Dynamic Time Systems

Dynamic time systems are based on planetary movements in the solar system. There are several dynamic time systems such as ephemeris time (ET), terrestrial time (TT), TDT, TDB. Ephemeris time was derived from motion of the Earth on its orbit around the Sun using Lunar observations. The basic idea behind ET was inventing uniform time scale to replace with time scales based on variable rotation of the Earth. However, it is no longer in use, TDT and TT were recommended instead of ET in order to use in the ephemerides. TDB was the relativistic equivalent of ephemeris time for planetary ephemerides calculations. See Seidelmann and Fukushima (1992) for more information.

2.1.3. Atomic Time Systems

Due to the non-uniform nature of universal time scales (e.g. UT0, UT1, UT2, etc.), TAI was defined in order to obtain a uniform time scale. Difference between TAI and UT is continuously changing. Therefore, UTC another atomic time scale, was established to keep this difference less than 0.9 seconds. In order to remain difference within 0.9 seconds, leap seconds have been introduced to UTC. Monitoring the universal time as well as determination of leap second are performed by IERS. UTC is estimated by distributed globally on geoid about 65 different laboratories from about 250 atomic clocks and hydrogen masers. See Lewandowski et al. (2006) for realizations of UTC such as UTC(SU) from Russia. The relation between several time scales are given in following equations (Sanz Subirana, Juan Zornoza and Hernández-Pajares, 2013)

$$TAI = UTC + 1^s \times n$$

$$TAI = TDT - 32^s.184$$

$$\Delta UT1 = UT1 - UTC \tag{2.2}$$

$$|\Delta UT1| < 0^s.9$$

where n denotes the number of leap seconds for the epoch of interest (e.g. n=37 by 1 Jan 2017). GPS time is another atomic time system started when leap seconds was 19s. Thus, $GPS - UTC = n - 19^s$. There are also time systems belong to other navigation satellite systems. Glonass Time is maintained in order to keep fluctuations w.r.t. UTC(SU) less than 1 milli-second.

7

2.2. Space Reference Systems

Coordinates of an object on Earth or in space should be stated in a well-defined reference system in order for precise measurement of distance towards this object. Thus, objects on Earth or in space are defined in terrestrial and celestial reference systems, respectively.

2.2.1. Terrestrial Reference System (TRS)

The terrestrial reference system is defined conventionally as an Earth-centered, Earth-fixed (ECEF), 3-dimensional, equatorial, Cartesian coordinate system as shown in Figure (2.2). The origin of the TRS is the centre of mass of the Earth. X_{TRS} is the intersection of the mean zero (Greenwich) meridian with the equatorial plane. Z_{TRS} is in the direction of the conventional terrestrial pole (CTP). Y_{TRS} is orthogonal to the X_{TRS} and Z_{TRS} in right-handed, 3-dimensional coordinate system. The realization of TRS so-called terrestrial reference frame (TRF) contains coordinates of several points on Earth called as reference points. ITRF (ITRF2005, Altamimi et al. 2007, ITRF2008, Altamimi, Collilieux and Métivier 2011, ITRF2014, Altamimi et al. 2016, etc.) are TRF realizations performed frequently by the IERS consisting of coordinates of crust-fixed geodetic reference points of several space geodetic techniques (e.g. VLBI, GNSS, SLR/LLR and DORIS). The realization is performed with inter and intra-technique combinations of these techniques in normal equation level due to each technique has its own advantage for determination of scale, translation, and rotation of estimated TRF w.r.t. the a priori. By conventions, rotation of the axes of the estimated TRF should be aligned to those of a priori TRF through using NNR condition equations.

2.2.2. Celestial Reference System (CRS)

The celestial reference system is a quasi-inertial, 3-dimensional, equatorial Cartesian, space-fixed coordinate system defined conventionally as shown in Figure (2.2). CRS has its origin at barycentre of the Solar system (Solar system's centre of mass). The Z_{CRS} axis is orthogonal to mean equatorial plane of the fundamental (J2000.0) epoch. The X_{CRS} axis is towards to mean vernal equinox of the fundamental epoch. The Y_{CRS} axis is orthogonal to others in right-handed, 3-dimensional coordinate system (Petit and Luzum, 2010). Realization of the CRS is so-called as international celestial reference frame (ICRF1, Ma et al. 1998, ICRF2 Fey, Gordon and Jacobs 2009, ICRF3 Charlot et al. 2018) performed with the observations of VLBI containing precise coordinates (angular positions) of Quasi-Stellar Radio Sources
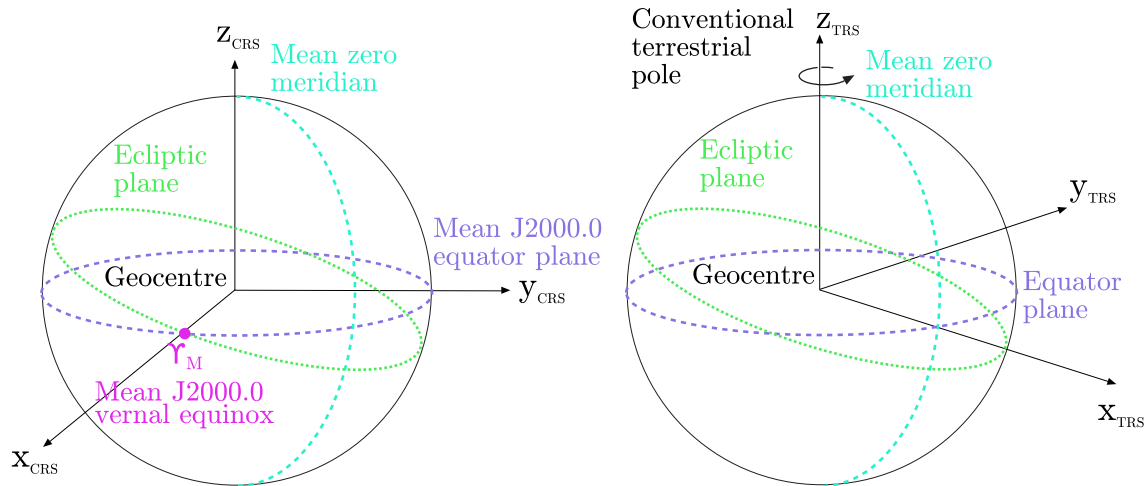
Figure 2.2: Space reference systems: Geocentric celestial reference system (left), geocentric terrestrial reference system (right).

(Quasars) in space. International Astronomical Union (IAU) defined the mean equinox and equator of the fundamental epoch in IAU1976 precession (Lieske et al., 1977) and IAU1980 nutation (Wahr, 1981b; Seidelmann, 1982) models. Thereafter, IAU resolutions in 2000 presented an enhanced CRS concept covering relativistic effects that splits CRS into barycentric celestial reference system (BCRS) and geocentric celestial reference system (GCRS). The origin of the BCRS is the centre of the mass of the Solar system as provided in IAU 2000A nutation (Mathews, Herring and Buffett, 2002) and IAU 2006 precession (Capitaine, Wallace and Chapront, 2003) models (Petit and Luzum, 2010). By convention, rotation of the axes of estimated CRF (e.g. ICRF3 Charlot et al. 2018) should be aligned to those of a priori CRF (e.g. ICRF2 Fey, Gordon and Jacobs 2009) through using NNR condition equations on the coordinates of defining sources.

2.3. Transformation Between TRS and CRS

Transformation of the coordinates between TRS and CRS are performed using EOP. These parameters correspond to the forced rotation, free rotation terms of Earth's orientation. The movement of Earth's axis of rotation in space w.r.t. space-fixed quasars contains a periodic component with 18.6-years period so-called nutation and secular component with 26000-years period named as precession. The Earth's rotation axis w.r.t. Earth's crust called polar motion. The free motion periods of polar motion is about 430 sidereal days so-called Chandler wobble and an annual term. There are two conventions of IERS defining these transforms named as Equinox-based (IAU 1976/1980 resolutions), and CIO-based (IAU 2000/2006 resolutions).

2.3.1. Equinox Based Conventions

The transformation of a quasar's coordinate from TRS to CRS as illustrated in Figure (2.3) may be carried out for epoch t using following equation (McCarthy, 1996; Sanz Subirana, Juan Zornoza and Hernández-Pajares, 2013)

$$[\mathbf{CRS}] = \mathbf{P}(t)\,\mathbf{N}(t)\,\mathbf{R_S}(t)\,\mathbf{R_M}(t)\,[\mathbf{TRS}], \tag{2.3}$$

and its inverse transform can be performed using e.g. below equation

$$[\mathbf{TRS}] = \mathbf{R_M^T}(t)\,\mathbf{R_S^T}(t)\,\mathbf{N^T}(t)\,\mathbf{P^T}(t)\,[\mathbf{CRS}]. \tag{2.4}$$

Here,

- $[\mathbf{CRS}]$ is the vector of position defined in the CRS,

- $[\mathbf{TRS}]$ is the vector of position defined in the TRS,

- $\mathbf{P}$ denotes the matrix of the precession for epoch of transformation consisting the precession angles ζ_A, θ_A, and z_A (Lieske et al., 1977) as given below

$$\mathbf{P}(t) = \mathbf{R_3}(\zeta_A)\,\mathbf{R_2}(-\theta_A)\,\mathbf{R_3}(z_A) \tag{2.5}$$

- $\mathbf{N}$ denotes the matrix of the nutation for epoch of transformation containing nutation angles ε_A, $\Delta\psi$, and $\Delta\varepsilon$ (Wahr, 1981b; Seidelmann, 1982) as follows

$$\mathbf{N}(t) = \mathbf{R_1}(-\varepsilon_A)\,\mathbf{R_3}(\Delta\psi)\,\mathbf{R_1}(\varepsilon_A + \Delta\varepsilon) \tag{2.6}$$

- $\mathbf{R_M}$ denotes the rotation matrix corresponding to polar motion for epoch of transformation uses polar coordinates of celestial ephemeris pole in terrestrial reference system (x_p, y_p) (see Figure 2.4) as given below

$$\mathbf{R_M}(t) = \mathbf{R_1}(y_p)\,\mathbf{R_2}(x_p) \tag{2.7}$$

- $\mathbf{R_S}$ denotes the matrix of the rotation corresponding Earth's rotation around the celestial ephemeris pole for epoch of transformation using Greenwich Apperent Sidereal Time (GAST: $\Theta_G = \theta_G + Eq.E = \theta_G + \Delta\psi\cos(\varepsilon_A)$) as follows

$$\mathbf{R_S}(t) = \mathbf{R_3}(-\Theta_G) \tag{2.8}$$
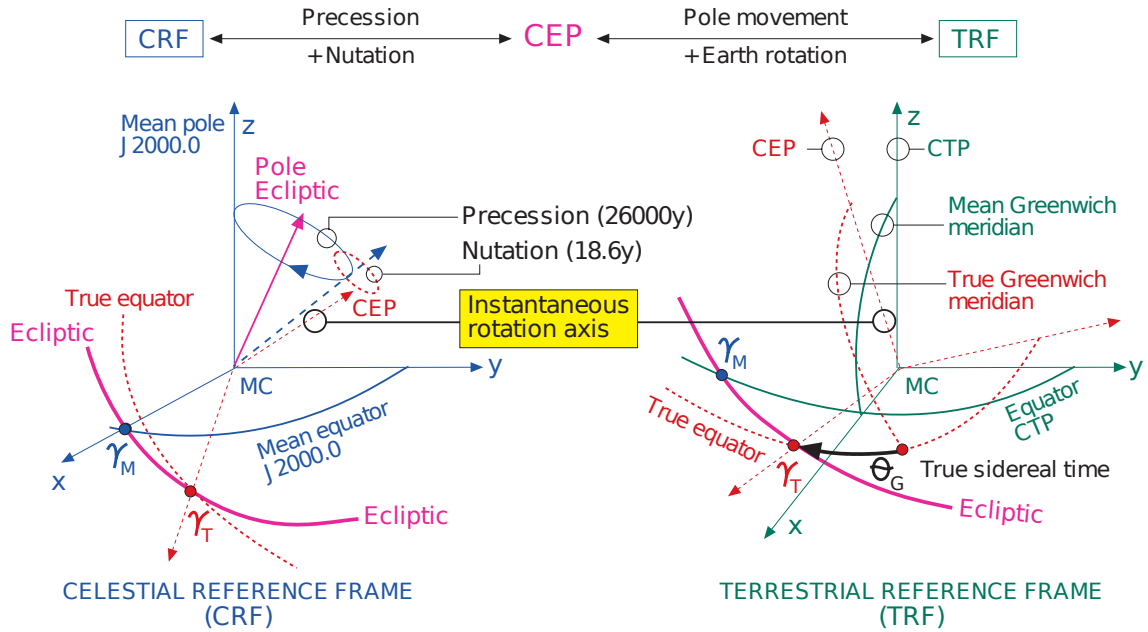
Figure 2.3: CRF-TRF transformation (Sanz Subirana, Juan Zornoza and Hernández-Pajares, 2013).
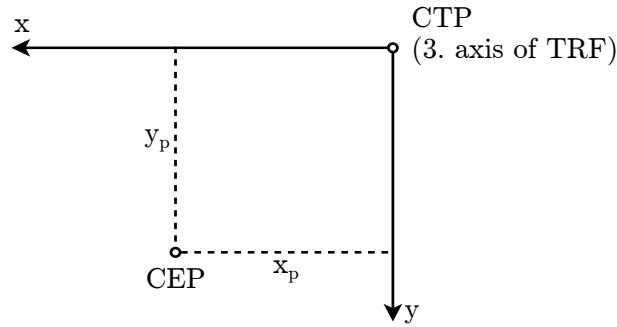
Figure 2.4: Polar motion coordinates: x_p and y_p.

2.3.2. CIO Based Conventions

CIO-based coordinate tranformation between celestial and terrestrial reference systems is based on IAU 2000A nutation (Mathews, Herring and Buffett, 2002) and IAU 2006 precession (Capitaine, Wallace and Chapront, 2003) models. Detailed information about transformation may be found in Wallace and Capitaine (2006) and Petit and Luzum (2010). Transformation from TRS to geocentric CRS is carried out as given below

$$[\mathbf{GCRS}] = \mathbf{Q}(t)\,\mathbf{R}(t)\,\mathbf{W}(t)\,[\mathbf{ITRS}], \tag{2.9}$$

and its inverse transform can be e.g. performed as follows

$$[\mathbf{ITRS}] = \mathbf{W}^{\mathbf{T}}(t)\,\mathbf{R}^{\mathbf{T}}(t)\,\mathbf{Q}^{\mathbf{T}}(t)\,[\mathbf{GCRS}] \tag{2.10}$$

where,

- [**GCRS**] is the coordinate vector defined in the GCRS,

- [**ITRS**] is the coordinate vector defined in the ITRS,

- **Q** denotes the matrix of the precession-nutation for epoch of transformation consisting spherical (polar) coordinates of the celestial intermediate pole in the GCRS (E and d) and CIO locator (s), which relates celestial intermediate system to geocentric CRS, as given below

$$\mathbf{Q}(t) = \mathbf{R_3}(-E)\,\mathbf{R_2}(-d)\,\mathbf{R_3}(E)\,\mathbf{R_3}(s),\qquad(2.11)$$

- **R** denotes the matrix of the rotation corresponding Earth Rotation Angle (ERA) between the celestial intermediate origin (CIO) and the terrestrial intermediate origin (TIO) on the celestial intermediate pole (CIP) equator, which relates terrestrial intermediate system and celestial intermediate system, as follows

$$\mathbf{R}(t) = \mathbf{R_3}(-ERA),\qquad(2.12)$$

- **W** denotes the matrix corresponding polar motion (coordinates of celestial intermediate pole, CIP, in the TRS: x_p, y_p) and TIO locator ($s^{'}$) for epoch of transformation, which relates terrestrial intermediate system to TRS, as given in following equation

$$\mathbf{W}(t) = \mathbf{R_3}(-s^{'})\,\mathbf{R_2}(x_p)\,\mathbf{R_1}(y_p).\qquad(2.13)$$

Detailed information on CIO-based transformation may be acquired in IERS conventions 2010.

2.4. Tidal Variations in Earth Rotation

2.4.1. Tidal Variations of ERP Caused by the Ocean Tides

On account of preserving angular momentum, mass redistribution (e.g. ocean tides) within the Earth and external torques applied on that system lead to vary both axis of rotation and rotation speed of the Earth (Munk and Macdonald, 1960). While the axial component of variations is leading to change the Earth rotation rate, the non-axial component is causing oscillations of the axis of rotation. The wobbling of rotation axis involves both polar motion and nutation. The distinction between polar motion and nutation was propounded at IERS 2010 conventions so that motions having frequencies within ± 0.5 cycles per sidereal day

Table 2.2: IERS coefficients of high frequency variations in Earth rotation because of ocean tides for principle diurnal and semi-diurnal tides (Petit and Luzum, 2010).

Tide	Delanunay coefficients						Period	x_p		y_p		$\Delta UT1$	
	γ	1	l'	F	D	Ω	(day)	A_k	B_k	A'_k	B'_k	A''_k	B''_k
Q_1	1	-1	0	-2	0	-2	1.1195148	6.2	26.3	-26.3	6.2	5.12	-2.50
O_1	1	0	0	-2	0	-2	1.0758059	48.8	132.9	-132.9	48.8	16.02	12.07
P_1	1	0	0	-2	2	-2	1.0027454	26.1	51.2	-51.2	26.1	5.51	-3.10
K_1	1	0	0	0	0	0	0.9972696	-77.5	-151.7	151.7	-77.5	-17.62	8.55
N_2	2	-1	0	-2	0	-2	0.5274312	-56.9	-12.9	11.1	32.9	-3.79	-1.56
M_2	2	0	0	-2	0	-2	0.5175251	-330.2	-27.0	37.6	195.9	-16.19	-7.25
S_2	2	0	0	-2	2	-2	0.5000000	-144.1	63.6	59.2	86.6	-7.55	-0.16
K_2	2	0	0	0	0	0	0.4986348	-38.5	19.1	17.7	23.1	-2.10	0.04

(cpsd) at celestial reference frame are accepted as nutation. Instead of this, at the terrestrial frame, nutation is counted on as a motion at frequencies between -1.5 and -0.5 cpsd. The difference for the viewing reference frames is the Earth's mean rotation rate (see Gross 2015 for more details).

The most remarkable physical reason for the sub-daily variations at the Earth rotation parameters (ERP) is ocean tides (Moritz and Mueller, 1987; Chao et al., 1996). The aforesaid physical excitation on polar motion and $\Delta UT1$ are modeled as harmonic functions with 71 tidal constituents, each having amplitudes, frequencies and phases based on previous work of Ray et al. (1994) at IERS conventions. The model comprises sine and cosine amplitudes, and arguments to calculate phase of harmonics at t instant for each of the 41 diurnal and 30 semi-diurnal tides (see Table 2.2 for significant tides). The phase at t epoch may be designated as

$$\xi_k(t) = \sum_{j=1}^{6} a_{kj}\alpha_j(t) \tag{2.14}$$

where a_{kj} is corresponding coefficient for k^{th} tide and j^{th} fundamental (astronomical) argument, and $\alpha_j(t)$ is the jth fundamental argument for t instant measured as Julian centuries after J2000 standard epoch (01.01.2000 12 UT) in terrestrial time (TT). These fundamental arguments were explained by Simon et al. (1994) and Petit and Luzum (2010).

The polar motion coordinates (x_p, y_p) and $\Delta UT1$ are determined with previously mentioned phase angle of harmonics, $\xi_k(t)$, and amplitudes, $A_k, B_k, A'_k, B'_k, A''_k, B''_k$ as

$$x_p(t) = \sum_{k=1}^{71} \left[A_k \sin(\xi_k(t)) + B_k \cos(\xi_k(t)) \right] \tag{2.15}$$

13

$$y_p(t) = \sum_{k=1}^{71} \left[A'_k \sin(\xi_k(t)) + B'_k \cos(\xi_k(t)) \right] \tag{2.16}$$

$$\Delta UT1(t) = \sum_{k=1}^{71} \left[A''_k \sin(\xi_k(t)) + B''_k \cos(\xi_k(t)) \right]. \tag{2.17}$$

The IERS model for sub-daily ERP because of ocean tides is now outdated. This is because number of tides and their amplitudes at the model were specified with geodynamic models in the absence of modern space geodetic techniques. As expressed in Chapter (3), estimation accuracy of any parameter is directly related to how its a priori value close to real value. Thus, revision of the present model is essentially important for achievement of current VLBI accuracy perspective (Artz et al., 2010; Nilsson, Böhm and Schuh, 2010; Nilsson et al., 2014). The great reference for estimation of model parameters from GNSS observations was exhibited by Desai and Sibois (2016). The accuracy of polar motion estimation is directly proportionate to volume of global polyhedron constructed by observing stations (Rothacher et al., 1999; Malkin, 2009). Due to the fact that, GNSS station network is huge, globally distributed and continuously working, polar motion estimation accuracy of GNSS technique is higher compared to VLBI. But, only VLBI observations are sensitive to $\Delta UT1$, and equatorial baselines can determine this parameter with high precision.

Prograde and Retrograde Polar Motions

In sub-daily time periods, orientation of the Earth rotation axis moves both clock-wise and counter way. Motions at positive frequencies are named as prograde motions in which movements of celestial intermediate pole (CIP) in Terrestrial reference frame (TRF) are in the same direction of Earth's rotation (counter clock-wise), whereas clock-wise movements of CIP in TRF are so-called as retrograde motions (negative frequencies). Decomposition of movement into prograde and retrogade parts may be carried out with Leonhard Euler formulae as (Weir, Hass and Heil, 2014)

$$A_k \cos(\xi_k(t)) = A_k \frac{e^{i\xi_k(t)} + e^{-i\xi_k(t)}}{2}, \tag{2.18}$$

$$A_k \sin(\xi_k(t)) = A_k \frac{e^{i\xi_k(t)} - e^{-i\xi_k(t)}}{2i} \tag{2.19}$$

where i is the unit imaginary number, coefficient of $e^{i\xi_k(t)}$ term belongs to prograde polar motion, and likewise coefficient of $e^{-i\xi_k(t)}$ term represents retrograde polar motion. While tides with 24-hours periods induce only prograde motion, 12-hours period tides excite both prograde and retrograde motions.

2.4.2. Long Periodic Tidal Variations of Polar Motion

Polar motion variations due to tidal excitation also occur between 9-days and 18.6-years periods so-called long periods (Petit and Luzum, 2010). Polar motion may be calculated as given below

$$\vec{p}(t) = p_x(t) - ip_y(t) = A_p e^{i\phi_p} e^{i\alpha(t)} + A_r e^{i\phi_r} e^{-i\alpha(t)} \tag{2.20}$$

where A_p, A_r denote prograde and retrograde amplitudes, and ϕ_p, ϕ_r represent prograde and retrograde phase terms, respectively. These corrections are arising from the long-period ocean tide effect modeled as spherical harmonics by Dickman and Nam (1995); Dickman and Gross (2010).

2.4.3. Zonal Tides of Earth's rotation

Yoder, Williams and Parke (1981) put forward the zonal tides of universal time (UT1), length-of-day (Δ), and Earth's rotation velocity (ω). Tidal potential of the Moon and the Sun contain zonal component parallel to equator. The zonal tide model containing 62 tidal harmonics having periods between 5.64-days to 18.6-years was developed by Yoder, Williams and Parke (1981); Wahr and Bergen (1986); Kantha, Stewart and Desai (1998); Defraigne and Smits (1999). In order to obtain the a priori values of UT1, zonal tides should also be considered (Petit and Luzum, 2010). The model values are given in Table (2.3) for several tides which have greatest amplitudes. UT2, UTS, and UTR are universal time scales obtained by reduction of several zonal tides from UT1 series of e.g. IERS 14 C04. If seasonal or all zonal tides are removed from UT1, obtained universal time is UT2 or UTS, respectively. Besides, UTR is achieved from reduction of zonal tides with periods less than 35-days from UT1. The phase angle of the kth tide at epoch t is found as below

$$\xi_k(t) = \sum_{j=1}^{5} a_{kj} \alpha_j(t) \tag{2.21}$$

where $\alpha_j(t)$ is j^{th} astronomical argument, and a_{kj} is Delaunay coefficient for k^{th} tide and j^{th} astronomical argument. Time epoch t is measured in terrestrial time frame as Julian centuries elapsed from fundamental epoch (J2000.0).

The tidal variations of UT1, LOD (Δ), and Earth's rotation velocity (ω) due to zonal tides may be computed as

$$\delta UT1(t) = \sum_{k=1}^{62} \left[C_k \sin(\xi_k(t)) + D_k \cos(\xi_k(t)) \right] \tag{2.22}$$

15

Table 2.3: IERS coefficients of zonal tides for ΔUT1 shown only for particular tides (Petit and Luzum, 2010). The periods are approximate values, and positive and negative signs of the period indicate the prograde and retrograde motions, respectively.

Delaunay coefficients					Period	δUT1 (10^{-4}s)		$\delta\Delta$ (10^{-5}s)		$\delta\omega$ (10^{-14}rad/s)	
1	l'	F	D	Ω	(days)	C_k	D_k	C'_k	D'_k	C''_k	D''_k
1	0	2	0	2	9.13	-0.9926	0.0000	6.8291	0.0000	-5.7637	0.0000
0	0	2	0	1	13.63	-3.1873	0.2010	14.6890	0.9266	-12.3974	-0.7820
0	0	2	0	2	13.66	-7.8468	0.5320	36.0910	2.4469	-30.4606	-2.0652
1	0	0	0	0	27.56	-8.4046	0.2500	19.1647	0.5701	-16.1749	-0.481
0	0	2	-2	2	182.62	-49.7174	0.4330	17.1056	0.1490	-14.4370	-0.1257
0	1	0	0	0	365.26	-15.8887	0.1530	2.7332	0.0263	-2.3068	-0.0222
0	0	0	0	2	-3399.19	7.8998	0.0000	0.1460	0.0000	-0.1232	0.0000
0	0	0	0	1	-6798.38	-1617.2681	0.0000	-14.9471	0.0000	12.6153	0.0000

$$\delta\Delta(t) = \sum_{k=1}^{62} \left[C'_k \sin(\xi_k(t)) + D'_k \cos(\xi_k(t)) \right] \tag{2.23}$$

$$\delta\omega(t) = \sum_{k=1}^{62} \left[C''_k \sin(\xi_k(t)) + D''_k \cos(\xi_k(t)) \right]. \tag{2.24}$$

where C_k, D_k, C'_k, D'_k, C''_k, and D''_k are model amplitudes given in Table (2.3).

3.PARAMETER ESTIMATION METHODS

3.1. Least Squares (LS) Adjustments

3.1.1. Gauss-Markov Model

Least squares method is a tool for adjustments of indirect observations when there are more observations than unknowns. In order to characterize the behavior of any natural event, mathematical model $\psi(x)$ and model parameters x should be designated. A model can be constructed in quite a few ways, due to the fact that the purpose of a certain model may vary according to point of view. Then, the composed model substitutes the physical phenomena as an approximation of it (Hirvonen, 1971). The functional model and the stochastic model are two components of the mathematical model. While the deterministic (non-random) properties of physical events are represented with the functional model, probabilistic (random) properties of it are expressed by the stochastic model. The functional model involves unknown parameters x, observations L_i and the post-fit residuals of the observations v_i as follows.

$$\psi_i(x) = L_i + v_i \tag{3.1}$$

Observation errors may be assumed to overlay on Normal distribution curve with zero mean and constant variance if functional model describes the physical events acting on observation sufficiently. The stochastic part of the mathematical model is exhibited with a variance-covariance matrix of the observations K_{ll} which is formed with the standard errors of observations m_i and the correlation coefficient between observations r_{ij}. The stochastic model i.e. the variance-covariance matrix of observations can be formed as follows:

$$K_{ll} = \begin{bmatrix} m_1^2 & r_{12}m_1m_2 & r_{13}m_1m_3 & \cdots & r_{1n}m_1m_n \\ r_{21}m_1m_2 & m_2^2 & r_{23}m_2m_3 & \cdots & r_{2n}m_2m_n \\ \vdots & \vdots & \vdots & & \vdots \\ r_{n1}m_1m_n & r_{n2}m_2m_n & r_{n3}m_3m_n & \cdots & m_n^2 \end{bmatrix}. \tag{3.2}$$

Using variance-covariance matrix, cofactor matrix Q_{ll} can be formed as stated below.

$$Q_{ll} = \frac{K_{ll}}{s_0^2} \tag{3.3}$$

The apriori variance factor s_0 is a measure of statistically distribution of observations around its expected value. For solving under-determined systems with least squares, the exact solution may not exists or there is infinitely many solutions exists that minimum norm solution may find one of them. Least squares may find a unique set of model parameters for over-determined systems which have the number of observations greater than the number of unknowns. Every portion of the data set will most probably indicate different models one to another owing to the errors which act on observations variously. Thus, there is no solution that will fit whole observations simultaneously. Least squares method finds the best fitting mathematical model parameters to observations by minimizing the sum of the residuals' squares that are the differences between calculated observations from mathematical model and real observations.

$$min\left[\sum_{i=1}^{n} v_i^2\, p_i\right] = min[v_1^2\, p_1 + v_2^2\, p_2 + \cdots + v_n^2\, p_n] \tag{3.4}$$

Gauss-Markov model is valid for the linear mathematical functions. For the non-linear function $\psi(x)$, Taylor series expansion should be applied for linearizing function around a priori values of unknown parameters x_0 with zero and first-order terms

$$v_i = \sum_j \frac{\partial \psi_i}{\partial x_j}(x_j - x_{0j}) - (L_i - \psi_i(x_0)) \tag{3.5}$$

where j^{th} reduced unknown parameter δx_j is difference between the estimated value of jth unknown parameter x_j and a priori value of it x_{0j}. Higher order term is neglected due to linearity rule of Gauss-Markov theorem. The functional model with u unknown parameters and n observations is as follows

$$\begin{bmatrix} v_1 \\ v_2 \\ \vdots \\ v_n \end{bmatrix} = \begin{bmatrix} (\frac{\partial \psi_1}{\partial x_1}) & (\frac{\partial \psi_1}{\partial x_2}) & \cdots & (\frac{\partial \psi_1}{\partial x_u}) \\ (\frac{\partial \psi_2}{\partial x_1}) & (\frac{\partial \psi_2}{\partial x_2}) & \cdots & (\frac{\partial \psi_2}{\partial x_u}) \\ \vdots & \vdots & \vdots & \vdots \\ (\frac{\partial \psi_n}{\partial x_1}) & (\frac{\partial \psi_n}{\partial x_2}) & \cdots & (\frac{\partial \psi_n}{\partial x_u}) \end{bmatrix} \begin{bmatrix} \delta x_1 \\ \delta x_2 \\ \vdots \\ \delta x_u \end{bmatrix} - \begin{bmatrix} l_1 \\ l_2 \\ \vdots \\ l_n \end{bmatrix} \tag{3.6}$$

where l_i is called as reduced observation

$$l_i = L_i - \psi_i(x_0). \tag{3.7}$$

The functional model in matrix form can be expressed with the residuals vector of observations v, the Jacobian (design) matrix A, the reduced unknown parameter vector δx and the

reduced observation vector l as follows

$$v = A\delta x - l. \tag{3.8}$$

To solve linearized equation system given in Equation (3.8), criterion for weighted and correlated observations in Equation (3.9) should satisfy (Koch, 1988; Öztürk and Serbetçi, 1989, 1992; Brockmann, 1997; Wolf and Ghilani, 1997; Niemeier, 2002; Teke, 2011).

$$v^T Q_{ll}^- v = v^T P v = minimum \tag{3.9}$$

$$v^T P v = (A\delta x - l)^T P(A\delta x - l) = (\delta x^T A^T - l^T)P(A\delta x - l)$$
$$= \delta x^T A^T P A \delta x - \delta x^T A^T P l - l^T P A \delta x + l^T P l \tag{3.10}$$

$$v^T P v = \delta x^T A^T P A \delta x - 2l^T P A \delta x + l^T P l \tag{3.11}$$

To find the variables that make Equation (3.11) minimum, partial derivatives w.r.t. to the vector δx should be applied to both side of Equation (3.11) and then set to zero.

$$\partial(v^T P v) = \delta x^T A^T P A \partial x + \partial x^T A^T P A \delta x - 2l^T P A \partial x = 0^T \partial x \tag{3.12}$$

Owing to the fact that $\partial dx^T A^T P A \delta x$ and $\delta x^T A^T P A \partial x$ are scalar values and $\partial x^T A^T P A \delta x = \delta x^T A^T P A \partial x$, Equation (3.13) is obtained as

$$\partial(v^T P v) = 2\delta x^T A^T P A \partial x - 2l^T P A \partial x = 0^T \partial x$$
$$\partial(v^T P v) = 2(\delta x^T A^T P A - l^T P A)\partial x = 0^T \partial x \tag{3.13}$$

Then Equation (3.14) called as normal equations system that satisfies the LS condition stated in Equation (3.9) is acquired by transposing the each side of the Equation (3.13).

$$A^T P A \delta x - A^T P A l = 0. \tag{3.14}$$

Adding the correction of unknown parameters vector δx, to the a priori values unknown parameters vector x_0 provides the total estimated value of unknown parameters vector x as shown in Equation (3.15)

$$x = x_0 + \delta x$$
$$x = x_0 + (A^T P A)^- A^T P l \tag{3.15}$$

The right hand side vector of the normal equation system b, and the normal equation matrix N can be demonstrated with the Equations (3.16) and (3.17)

$$N = A^T P A \qquad (3.16)$$

$$b = A^T P l \qquad (3.17)$$

Then, correction vector of unknown parameters can be inferred from equation below.

$$\delta x = N^- b \qquad (3.18)$$

For weighted observations , the a posteriori standard deviation of unit weight is derived as

$$m_0 = \sqrt{\frac{\sum p v^2}{r}} = \sqrt{\frac{v^T P v}{n - u}} \qquad (3.19)$$

where $\sum p v^2$ is the sum of squares of weighted observation residuals and its matrix form $v^T P v$ and r denotes degrees of freedom in other words redundant measurements of the adjustment.

3.1.2. Constraining Parameters

Constraining parameters is used in least squares adjustment for more than one reasons. If observations (measurements) is paused for certain period of time, estimated parameters at these epochs would be incorrect values. This data gaps are common in sessions of the space geodetic techniques e.g. hardware failures. The use of relative constraints limits the oscillation of the estimated value from the actual value even if there is no observation in estimation epoch. Even for systems with huge number of observations than unknowns, linearly dependent set of equations may lead to singularity. Some geodetic networks are not sensitive to certain earth related parameters that construct linearly dependent equations. On the other hands, for under-determined systems, there is more unknown parameters than observations. Thus, least squares adjustments will not find a solution without constraining parameters. If there is a prior knowledge about system parameter that will not indicate meaningful change during observation period, this parameter should be constrained to its a priori value to overcome propagating other parameters error into this parameter. In least squares adjustment method, constraint equations can be formed as follows

$$v_c = H \delta x - h \qquad (3.20)$$

where H is design matrix of pseudo-observations (constraint equations), h is reduced observation vector of the constraints, v_c is the residuals vector. Normal equation for the pseudo-observations is derived from least squares adjustment method as follows under the condition of minimization of the squares of weighted pseudo-observational residuals ($min[\sum v_c^2\, p_c]$)

$$H^T P_c H \delta x = H^T P_c h \tag{3.21}$$

where P_c indicates pseudo-observation's weight matrix. Imposing the constraints at normal equation level can be represented as

$$(A^T P A + H^T P_c H)\delta x = A^T P l + H^T P_c h. \tag{3.22}$$

Sum of coefficient matrix of normal equations for observations (N) with those of the pseudo-observations (N_c) constrained normal equation matrix (N_t) is setup as

$$N_t = A^T P A + H^T P_c H = N + N_c \tag{3.23}$$

Right hand side vector of the constrained normal equation system is formed as follows

$$b_t = A^T P l + H^T P_c h = b + b_c. \tag{3.24}$$

The residuals of the constrained unknown parameter vector can be written as

$$\delta x = N_t^- b_t. \tag{3.25}$$

Then, the total constrained unknown parameter vector is formed as

$$x_c = x_0 + \delta x = x_0 + N_t^- b_t. \tag{3.26}$$

A posteriori standard deviation of the constrained adjustment can be derived as follows

$$m_{0c} = \sqrt{\frac{v^T P v + v_c^T P_c v_c}{n + n_c - u}} \tag{3.27}$$

where n_c denotes the number of constraint equations (pseudo-observations). There are two types of constrains that are mostly applied to the geodetic parameters, absolute and relative. For *absolute constraint*, parameter may be constrained to a desired value. Then, design matrix of pseudo-observations that contains relations between parameters will not be formed. Afterwards, the functional model in matrix form will be

$$v_c = \delta x - h. \tag{3.28}$$

If the desired values are constrained as a priori values of the parameters, all the elements of the reduced observation vector for constraints, h will be zero. The other constraint type is *relative constraints* that arranges relationship between the estimates of two adjacent parameters.

3.1.3. Free Network Solution

Datum is the reference used for defining any coordinate system. In other words, for three dimensional cartesian coordinate systems, datum specifies the orientation and the origin of coordinate system. In a geodetic networks containing several observing stations, independent of geodetic technique, measurements do not contain information about full set of datum parameters. For unique definition of station coordinates, in a three dimensional networks, at least 7 datum parameters should be a priori defined. This datum definition may be based on some station coordinates by assuming their a priori coordinates x_0, y_0, z_0 as stationary and held as fixed in adjustments. This method utilizes absolute constrains on station coordinates by fixing them to their a priori values. This method causes large errors on several station coordinates of which locations are far from the fixed ones. Another way of datum definition is constraining a priori coordinates of some stations with no-net-translation (NNT), no-net-scale (NNS), and no-net-rotation (NNR) condition equations. NNT condition is limiting the change of origins between a priori and estimated coordinate systems. Variations of direction of axes and scale factor between the coordinate systems can be determined by NNR and NNS conditions, respectively. Applying these three condition equations i.e., NNT, NNR, and NNS will set free the a priori coordinates of stations to move but instead minimize the sum of the squares of estimated station coordinate corrections of whole network. This condition equations can be provided by 7 parameters Helmert transformation (Helmert, 1872; Rao and Mitra, 1971; Prongle and Rayner, 1971; Pelzer, 1974). Helmert transformation involves translation vector $[T_x \ T_y \ T_z]^T$ stating the variations of the origin in x, y, z directions respectively, rotation matrix R and scale factor μ as

$$\begin{bmatrix} X \\ Y \\ Z \end{bmatrix} = (1 + \mu)R \begin{bmatrix} X_0 \\ Y_0 \\ Z_0 \end{bmatrix} + \begin{bmatrix} T_x \\ T_y \\ T_z \end{bmatrix}.$$

(3.29)

Rotation matrix comprises the orientations around the 3st, 2st, and 1st axes of which positive rotation angles in counter-clockwise directions. In fact, rotation angles between estimated and a priori coordinate systems are very small in geodetic applications. Then, using Taylor

series expansion about the zero the rotation matrix can be rearranged as follows

$$R = \begin{bmatrix} 1 & \gamma & -\beta \\ -\gamma & 1 & \alpha \\ \beta & -\alpha & 1 \end{bmatrix}. \tag{3.30}$$

After substituting the rotation matrix R given in Equation (3.30) into the Equation (3.29) and rearranging equations, following equation

$$\begin{bmatrix} X_1 \\ Y_1 \\ Z_1 \\ X_2 \\ Y_2 \\ Z_2 \\ \vdots \end{bmatrix} = \begin{bmatrix} X_{01} \\ Y_{01} \\ Z_{01} \\ X_{02} \\ Y_{02} \\ Z_{02} \\ \vdots \end{bmatrix} + \begin{bmatrix} 1 & 0 & 0 & X_{01} & 0 & -Z_{01} & Y_{01} \\ 0 & 1 & 0 & Y_{01} & Z_{01} & 0 & -X_{01} \\ 0 & 0 & 1 & Z_{01} & -Y_{01} & X_{01} & 0 \\ 1 & 0 & 0 & X_{02} & 0 & -Z_{02} & Y_{02} \\ 0 & 1 & 0 & Y_{02} & Z_{02} & 0 & -X_{02} \\ 0 & 0 & 1 & Z_{02} & -Y_{02} & X_{02} & 0 \\ & & & \cdots & & & \end{bmatrix} \begin{bmatrix} T_X \\ T_Y \\ T_Z \\ \mu \\ \alpha \\ \beta \\ \gamma \end{bmatrix} \tag{3.31}$$

can be derived and its matrix representation is as follows

$$X = X_0 + B\zeta. \tag{3.32}$$

The unknown transformation parameters ζ can be derived as

$$\zeta = B^-(X - X_0) \tag{3.33}$$

Helmert transformation parameters in ζ vector needed to be zero to fulfill the NNT, NNR, and NNS conditions of the free network solution,

$$\zeta = B^-(X - X_0) = 0. \tag{3.34}$$

The acquired design matrix B can be assumed to be the Jacobian matrix of the constrain equations as follows

$$H = B^+ = (B^T B)^- B^T, \tag{3.35}$$

and the reduced observation vector for the constraints will be a zero vector ($h = 0$). The free network solution where the constraints are imposed in normal equation level is as follows

$$(A^T P A + H^T P_c H)\delta x = A^T P l, \tag{3.36}$$

where P_c denotes the weight matrix of the constraint equations.

There is one more way of performing the free network solution as applied on coordinate estimates via imposing condition equations to the normal equation system. In this way, normal equation matrix includes the condition equations B, the unknown parameters of the condition equations δx_c, the constants vector of the condition equations b_c (zero vector) and $A^T P A$ involving the relative and absolute constraint as follows

$$\begin{bmatrix} A^T P A & B \\ B^T & 0 \end{bmatrix} \begin{bmatrix} \delta x \\ \delta x_c \end{bmatrix} = \begin{bmatrix} A^T P l \\ b_c \end{bmatrix} \tag{3.37}$$

and its another representation is

$$N_t \, \delta_{xt} = b_t \tag{3.38}$$

where N_t and b_t are the datum conditions imposed coefficients matrix and constants vector of normal equations, respectively (Wolf and Ghilani, 1997; Öztürk and Serbetçi, 1992; Thaller, 2008; Teke, 2011).

3.1.4. Combination (Global Solution) of Several Parameters at Normal Equation Level

LS estimation creates a normal equation system matrix for every observing sessions which are performed within predefined time intervals. In order to estimate specific parameters from the observations of more than one session by stacking the normal equation system matrices, pre-elimination of certain parameters will overcome hardware related processing issues caused by handling huge matrix operations. It is a basic procedure so as to reduce the dimensions of the normal equation system while keeping influences of the reduced parameters on entire estimation. That means, the reduced parameters implicitly remain in the normal equation system. Pre-reduction procedure is not analogues to fixing parameters to their a priori values by removing belonging lines from the normal equation system. In other words, estimation of this parameters from the normal equation system will not be possible after elimination but their effects on the other (remaining) parameters will not be changed. If the reduced parameters are assumed as being in δx_1. These reduced parameters somehow should be re-ordered at the top of unknown parameters vector. Thus, desired parameters to be estimated will be located at the bottom of the unknown parameters vector and called as

δx_2. The normal equation system with the corresponding sub-matrices will be as follows,

$$
\begin{bmatrix} N_{11} & N_{12} \\ N_{21} & N_{22} \end{bmatrix} \begin{bmatrix} \delta x_1 \\ \delta x_2 \end{bmatrix} = \begin{bmatrix} b_1 \\ b_2 \end{bmatrix}.
\tag{3.39}
$$

After matrix multiplication,

$$
N_{11}\,\delta x_1 + N_{12}\,\delta x_2 = b_1
$$
$$
N_{21}\,\delta x_1 + N_{22}\,\delta x_2 = b_2
\tag{3.40}
$$

are found. Solving the first of Equation (3.40) for δx_1,

$$
\delta x_1 = N_{11}^-\,(b_1 - N_{12}\,\delta x_2)
\tag{3.41}
$$

and using of δx_1 in the second of Equation (3.40) forms

$$
N_{21}\,(N_{11}^-(b_1 - N_{12}\,\delta x_2)) + N_{22}\,\delta x_2 = b_2.
\tag{3.42}
$$

Solving Equation (3.42) for δx_2 yields

$$
(N_{22} - N_{21}N_{11}^-N_{12})\delta x_2 = b_2 - N_{21}N_{11}^-b_1
$$
$$
N_r\,\delta x_2 = b_r
\tag{3.43}
$$

where N_r is the coefficients matrix and b_r the constants vector of normal equations after parameter reduction applied,

$$
N_r = N_{22} - N_{21}N_{11}^-N_{12}
$$
$$
b_r = b_2 - N_{21}N_{11}^-b_1
\tag{3.44}
$$
$$
v^T P v = l^T P l - \delta x^T b_r = \cdots = l^T P l - b_1^T N_{11}^- b_1 - \delta x_2^T b_r.
$$

Combination of several normal equation systems is possible for both batch and sequential methods. In both method, estimated parameters would be under the influence of combined normal equation system (Helmert, 1872). Batch method utilizes observing series for defined period altogether. Sequential method updates its estimate by processing every new observation. The sequential method converges the estimates of the batch processing (Brockmann, 1997). Parameter pre-reduction procedure helps for stacking of observing sessions together by reducing the dimensions of the normal equation systems. Stacking with batch method involves Jacobian matrices A and weight matrices of independent sessions (zero off-diagonal

elements) P as

$$A = \begin{bmatrix} A_1 \\ A_2 \\ \vdots \\ A_k \end{bmatrix}, P = \begin{bmatrix} P_1 & 0 & \cdots & 0 \\ 0 & P_2 & \cdots & 0 \\ \vdots & \vdots & \ddots & \vdots \\ 0 & 0 & \cdots & P_k \end{bmatrix} \quad (3.45)$$

and estimation equation

$$A^T P A \delta x_2 = A^T P l. \quad (3.46)$$

Then, unknown combined parameters δx_2 may be found as

$$(A_1^T P_1 A_1 + A_2^T P_2 A_2 + \cdots + A_k^T P_k A_k)\delta x_2 = A_1^T P_1 l_1 + A_2^T P_2 l_2 + \cdots + A_k^T P_k l_k$$

$$(N_{r1} + N_{r2} + \cdots + N_{rk})\delta x_2 = b_{r1} + b_{r2} + \cdots + b_{rk}.$$
$$(3.47)$$

3.2. Singular Value Decomposition

Singular value decomposition (SVD) is another method for solving Equation (3.48). The design matrix A is not square matrix for space geodetic techniques. For this reason, solving this equation is not possible with simple inversion. Instead, pseudo-inverse of design matrix, A^+, should be found in order to acquire corrections of parameters, δx, from reduced observations vector, l. The SVD is very handy tool when the design matrix is rank-deficient. The decomposition procedure so-called factorization is applied in the inverse solution method, SVD to the functional model given below

$$A\delta x = l. \quad (3.48)$$

The SVD preserves information of the original matrix after decomposition. Following equations will be convenient for over-determined systems, as well as, they can be derived also for under-determined systems. Key advantage of SVD is that providing robust solution in order for linear least squares problems (Golub and Van Loan, 1996; Alter, Brown and Botstein, 2000; Strang, 2006; Haykin, 2014).

For design matrix $A_{[n \times u]}$ where n and u are the amount of observations (rows), and unknown

parameters (columns), respectively. Decomposition is executed as

$$A = U\Sigma V^T \tag{3.49}$$

where columns of $U_{[n\times n]}$ unitary matrix are left singular vectors of A, columns of $V_{[u\times u]}$ matrix containing orthonormal properties of A are right singular vectors of A, and elements of $\Sigma_{[n\times u]}$ diagonal matrix are called as singular values of A. So as to compute U orthogonal matrix, the eigen-vectors corresponding to largest eigen-values of AA^T that construct columns of U is found via solving following equation:

$$|AA^T - \lambda I| = 0 \tag{3.50}$$

where I is identity matrix, λ is a scalar value. Similarly, the eigen-vectors of $A^T A$ construct V orthogonal matrix. The Σ matrix containing singular values, σ_i, is as follows

$$\Sigma = \begin{bmatrix} \sigma_1 & 0 & \dots & 0 & 0 & \dots & 0 \\ 0 & \sigma_2 & \dots & 0 & 0 & \dots & 0 \\ \vdots & \vdots & \ddots & \vdots & & \vdots & \\ 0 & 0 & \dots & \sigma_r & 0 & \dots & 0 \\ 0 & 0 & \dots & 0 & 0 & \dots & 0 \\ & & \vdots & & & \vdots & \ddots & \vdots \\ 0 & 0 & \dots & 0 & 0 & \dots & 0 \end{bmatrix} \tag{3.51}$$

where r is rank of A matrix, σ_i values are sorted as $\sigma_1 \geq \sigma_2 \geq \cdots \geq \sigma_u$, and values of σ_i for $i > r$ are zero ($\sigma_{r+1} = \sigma_{r+2} = \cdots = \sigma_u = 0$). Under the condition of $minimize \, ||A\delta x - l||$, the pseudo-inverse of design matrix A is specified as

$$A^+ = (A^T A)^- A^T. \tag{3.52}$$

If Equation (3.49) is substituted with A, pseudo-inverse is obtained as follows

$$\begin{aligned} A^+ &= [(U\Sigma V^T)^T \, (U\Sigma V^T)]^- \, (U\Sigma V^T)^T \\ &= [(V\Sigma^T U^T) \, (U\Sigma V^T)]^- \, (V\Sigma^T U^T). \end{aligned} \tag{3.53}$$

It is known that for orthogonal matrix $U^T U = I_{n \times n}$, therefore equation becomes as follows

$$
\begin{aligned}
A^+ &= [V\Sigma^T\Sigma V^T)]^-(V\Sigma^T U^T) \\
&= [(V^T)^- (\Sigma^T\Sigma)^- V^-](V\Sigma^T U^T).
\end{aligned}
\tag{3.54}
$$

Similarly, $V^T V = I_{n \times n}$ and $V^- = V^T$ are also hold for orthogonal matrix V, consequently, A^+ to be simplified as below

$$
A^+ = V(\Sigma^T\Sigma)^-\Sigma^T U^T
\tag{3.55}
$$

where $\Sigma^+ = (\Sigma^T\Sigma)^-\Sigma^T$ is pseudo-inverse of Σ

$$
A^+ = V\Sigma^+ U^T.
\tag{3.56}
$$

Then, estimated parameter vector δx is assigned as

$$
\delta x = V\Sigma^+ U^T l.
\tag{3.57}
$$

3.3. Complex Demodulation

The complex demodulation is an elementary technique for time series analysis. By means of Fourier analysis, it is proved that any time series may be expressed with sufficiently much sinusoidal functions (Oppenheim, Willsky and Nawab, 1997). In addition to this, amplitudes and phases of these sinusoidal functions can be found with complex demodulation if prior knowledge of the frequency of these functions is held. Although, the concept of modulation/demodulation is in the scope of communication systems, time series analysis studies take advantage of such a tool. Complex demodulation is known as the equivalent of heterodyne detectors (Choi et al., 1986; Gasquet and Wootton, 1997). For the purpose of extracting amplitudes of sinusoidal waves from time series, the least squares and singular value decomposition techniques are often used. But, these tools apportion residuals (e.g. noises or meaningful geodynamic signals) among all estimated parameters. Another difference of complex demodulation from linear equation system solutions is that every sinusoidal amplitude are estimated individually in contrast to simultaneous estimation in LS and SVD. As a result, complex demodulation is more robust when frequencies of harmonics are so close to each other and noise is high. But, least squares and singular value decomposition can fit any kind of equation to time series. The comprehensive foundation in the theory of complex demodulation may be found in Hasan (1983); Bloomfield (2000).

Consider a time series of $x(t)$,

$$x(t) = A_{dc} + A_c \, cos(2\pi f_c t) \qquad (3.58)$$

where A_{dc} represents offset component of signal, A_c is the amplitude of sinusoidal function which have frequency f_c. The complex demodulation is performed via multiplying the time series $x(t)$ with the complex exponential at frequency f as given below:

$$
\begin{aligned}
y(t) = x(t)e^{i2\pi ft} \quad &= A_{dc} \, e^{i2\pi ft} + \frac{A_c}{2} \left[e^{i2\pi f_c t} + e^{-i2\pi f_c t} \right] e^{i2\pi ft} \\
&= A_{dc} \, e^{i2\pi ft} + \frac{A_c}{2} \left[e^{i2\pi(f+f_c)t} + e^{i2\pi(f-f_c)t} \right].
\end{aligned} \qquad (3.59)
$$

Choosing $f \simeq f_c$ is the crucial factor for acquiring amplitudes properly. Then, low-pass-filter (LPF) is applied to the $y(t)$ as given,

$$LPF[y(t)] = \frac{A_c}{2} \, e^{i2\pi(f-f_c)t} \qquad (3.60)$$

where cut-off frequency and frequency response of LPF should be chosen so as to pass only desired signal without distorting its amplitude. Consequently, high frequency components of demodulated signal are removed. Thereafter, magnitude of filtered signal will be equal to half of amplitude as stated below

$$|LPF[y(t)]| = \frac{A_c}{2}. \qquad (3.61)$$

If the sufficiently narrow-band low-pass filter is applied, complex demodulation captures amplitude of sinusoidal signal only for the desired frequency. It is similar to Fourier transform, nevertheless, it does not take the Fourier transform place, due to the fact that bandwidth of the oscillation should be known prior to estimation.

4. TROPOSPHERE DELAYS

4.1. Radio-wave Propagation in Neutral Atmosphere

The Earth is surrounded by the gaseous envelope named as the Earth's atmosphere which stays close to the Earth owing to the gravity. %99 of the mass of the atmosphere concentrate up to ∼10-km height from sea level. The atmosphere consists of different constituents, that may be investigated under three fundamental parts: water substance, dry air, and aerosols (Iribarne and Godson, 1973). While an electromagnetic wave emitted from source such as artificial satellite or galaxy in space to the Earth, after entering Earth's atmosphere, firstly it is effected by free electrons exist in the ionosphere, then electrically neutral part of atmosphere called as troposphere. For analysis of observations of space/satellite based geodetic techniques i.e. VLBI, GNSS, DORIS, modeling of electromagnetic radio-wave propagation is important. The effects of the charged particles in ionosphere on radio-wave may be removed pretty well via utilizing dual-frequency radio-wave length observations because ionosphere is a dispersive medium where the propagation velocity of a radio-wave changes by its frequency. However, impacts of non-dispersive (frequency-independent) part of the atmosphere could not be removed from dual-frequency observations. Moreover, spatio-temporal variation of the troposphere water vapor content, cause radio-wave signals to delay ranging from 5 to 35 cm in zenith direction, is very high. Thus, modeling the propagation of electromagnetic radio-waves through troposphere is necessary to quantify the delay of the signal along he path of the observations. For a neutral (source free) and non-conducting medium, Maxwell's equations describing propagation of electromagnetic waves are (Cheng, 1989; Jackson, 1999)

$$\nabla \cdot (\varepsilon \vec{E}) = 0, \tag{4.1}$$

$$\nabla \cdot \vec{B} = 0, \tag{4.2}$$

$$\nabla \times \vec{E} = -\frac{\partial \vec{B}}{\partial t}, \tag{4.3}$$

$$\nabla \times \vec{B} = \mu \varepsilon \frac{\partial \vec{E}}{\partial t}, \tag{4.4}$$

where ε denotes medium's electric permittivity, and μ indicates medium's magnetic permeability medium, $\vec{E}$ is the electric field, and $\vec{B}$ is the magnetic field. For small spatio-temporal variations in ε and μ, the vector Laplacian of the electric field may be assumed as follows (Böhm and Schuh, 2013)

$$\nabla^2 \vec{E} = \mu \varepsilon \frac{\partial^2 \vec{E}}{\partial t^2}. \tag{4.5}$$

The phase velocity of the electromagnetic wave in medium with properties of propagation medium ε and μ is

$$v_p = \frac{1}{\sqrt{\mu\varepsilon}}, \tag{4.6}$$

and free space velocity of electromagnetic wave is

$$c = \frac{1}{\sqrt{\mu_0\varepsilon_0}} \tag{4.7}$$

where ε_0 denotes free-space electric permittivityand μ_0 are the electric permittivity, and magnetic permeability in free space, respectively. Then, n called as the refractive index is defined as (Bleaney and Bleaney, 1978)

$$n = \frac{c}{v_p} = \frac{\sqrt{\mu\varepsilon}}{\sqrt{\mu_0\varepsilon_0}} = \sqrt{\mu_r\varepsilon_r} \tag{4.8}$$

where ε_r and μ_r are relative permittivity and relative permeability of medium relative to the vacuum respectively. In fact, for absorptive materials, refractive index, $\tilde{n}$, is a complex number. Imaginary part of $\tilde{n}$ corresponds to the coefficient of absorption (Mendes, 1999). With exception of water vapor line (22.235 GHz) and oxygen line (60 GHz), on the radio-wave frequency spectrum, the refraction effects are dependent on the real part of refractive index only. So refractivity is not frequency dependent for operating frequencies of space geodetic techniques. Refractive index n in the Earth's neutral atmosphere is approximately one, then using refractivity N instead of recractive index is more convenient (Böhm and Schuh, 2013). Refractivity may be derived from refractive index as

$$N = (n - 1) \cdot 10^6. \tag{4.9}$$

Radio wave propagation speed (phase speed) slows down with the increasing of refractive index. The water vapor (wet constituents) and dry air quantities are changing in both space and time, then refractive index varies in every portion of medium wave traveling in it. This causes a deviation of wave's propagation path from a straight line as a consequence of least time principle of Fermat (Born and Wolf, 1975). Arrival time of a radio signal may be delayed compared to propagation in vacuum environment by retardation and bending effects caused by troposphere ingredients. Figure 4.1 shows the shortest paths in terms of time (S) and in terms of length (G) (Böhm and Schuh, 2013). While, the wave in vacuum would propagate through straight line, G, in neutral atmosphere, the wave propagates through the curve, S. The electromagnetic path length which is longer than G (geometric length) may be found as

$$L = \int_S n(s)ds. \tag{4.10}$$
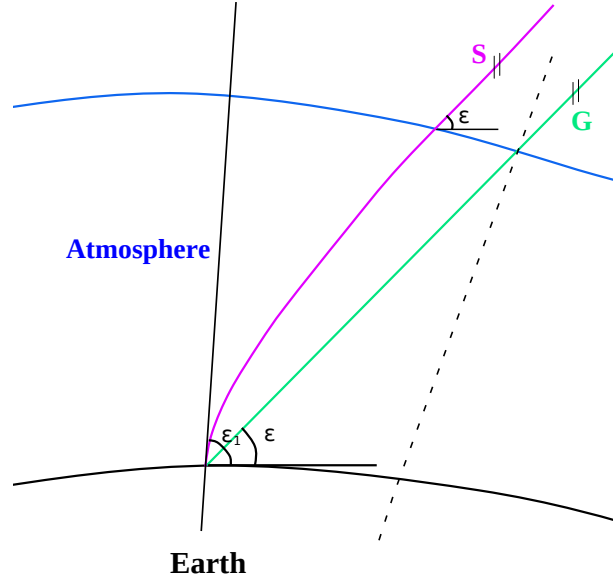
Figure 4.1: Ray bending in the neutral part of the atmosphere.

The geometric length, G, defined for vacuum environment may be stated as

$$G = \int_{vac} ds. \tag{4.11}$$

The geometric length of actual wave propagation path in neutral atmosphere, S, is defined as

$$S = \int_S ds. \tag{4.12}$$

The propagation delay owing to the neutral atmosphere, ΔL, which is difference of geometric path length from electromagnetic path length:

$$\Delta L = L - G. \tag{4.13}$$

Slant path delay may be handled for analysis of geodetic observations in two ways. Firstly, slant total delay derived from observations of other techniques may be reduced from observations. The other way is estimation of delay caused by troposphere. In order to estimate any variable properly from linearized least square estimation (see Chapter 3 for more details), a priori value of this variable should be close to its actual value. Therefore, modeling the troposphere is necessary for estimation of slant total delay. Using Equations (4.10) and (4.11) in Equation (4.13), by adding and subtracting Equation (4.12),

$$\Delta L = \int_S n(s)ds - \int_S ds + \int_S ds - G, \tag{4.14}$$

$$\Delta L = \int_S [n(s) - 1]ds + \int_S ds - \int_{vac} ds = 10^{-6} \int_S N(s)ds + S - G. \tag{4.15}$$

If the refractivity $N(s)$ is separated into two parts: hydrostatic refractivity, $N_h(s)$ and wet refractivity, $N_w(s)$, then slant path delay

$$\Delta L = 10^{-6} \int_S N_h(s)ds + 10^{-6} \int_S N_w(s)ds + S - G. \tag{4.16}$$

In general, excess path delay caused by bending effect, $S - G$, is included to hydrostatic delay via hydrostatic mapping function (see Subsection 4.2) (Böhm and Schuh, 2013) Under the assumptions of refractivity is not frequency dependent, and there is no water constituents in liquid phase, refractivity N is as follows

$$N = k_1 \frac{p_d}{T} Z_d^{-1} + k_2 \frac{p_w}{T} Z_w^{-1} + k_3 \frac{p_w}{T^2} Z_w^{-1}. \tag{4.17}$$

where dry air pressure, p_d, water vapor pressure, p_w, temperature, T, dry air compressiblity factor Z_d, and water vapor compressiblity factor Z_w (Böhm and Schuh, 2013). The constants k_1, k_2 and k_3 are emprically determined from several laboratory experiments. These constants are varying with atmospheric substance concentrations. Details of determination of the constants may be found in Rüeger (2002a,b). $k_1 \approx 77.6 \frac{K}{hPa}$, $k_2 \approx 70.4 \frac{K}{hPa}$, and $k_3 \approx 375000 \frac{K^2}{hPa}$. Another representation of Equation (4.17) is

$$N = k_1 \frac{R}{M_d} \rho + k_2' \frac{p_w}{T} Z_w^{-1} + k_3 \frac{p_w}{T^2} Z_w^{-1}. \tag{4.18}$$

where R is the universal gas constant, M_w is the molar mass of water vapor, M_d is the molar mass of dry air, $k_2' = k_2 - k_1 \frac{M_w}{M_d}$, and $\rho = \rho_d + \rho_w$ is sum of dry air density ρ_d and water vapor density ρ_w. Then, the hydrosatatic refractivity N_h and wet refractivity N_w may be seperated from total refractivity N as

$$N_h = k_1 \frac{R}{M_d} \rho, \tag{4.19}$$

$$N_w = k_2' \frac{p_w}{T} Z_w^{-1} + k_3 \frac{p_w}{T^2} Z_w^{-1}. \tag{4.20}$$

For expressing delays in zenith direction instead of direction of observation, the zenith hydrostatic delay, ΔL_h^z, and the zenith wet delay, ΔL_w^z, may be found as

$$\Delta L_h^z = 10^{-6} \int_{h_0}^{\infty} N_h(z)dz, \tag{4.21}$$

$$\Delta L_w^z = 10^{-6} \int_{h_0}^{\infty} N_w(z)dz \tag{4.22}$$

where h_0 is the site altitude. ΔL_h^z is derived by Saastamoinen (1972, 1973), and refined by Davis et al. (1985) as

$$\Delta L_h^z = \frac{0.0022768 \cdot p_0}{1 - 0.00266 \cdot cos(2\varphi_0) - 0.28 \cdot 10^{-6} h_0} \tag{4.23}$$

where p_0 is total pressure in hPa at receiving station which has orthometric height, h_0, and latitude, φ_0. Because of the high spatio-temporal variation of water vapor, modeling the wet part of the zenith delay is more challenging than the hydrostatic delay. The water vapor quantity and Earth's surface temperature may not be representative for higher altitudes.

4.2. Troposphere Mapping Functions

Azimuthal symmetry assumption refers that delays are only depends on elevation angle. That means, there is no azimuthal variation in terms of zenith delay. This approach is described as (Davis et al., 1985)

$$\Delta L(\varepsilon) = \Delta L_h^z \cdot m_h(\varepsilon) + \Delta L_w^z \cdot m_w(\varepsilon) \tag{4.24}$$

where ε is elevation angle defined in vacuum, $m_h(\varepsilon)$ and $m_w(\varepsilon)$ are hydrostatic and wet mapping functions respectively. In fact, mapping functions are providing a ratio of the delays in the observation direction to the delays in the direction of zenith. Proposed azimuthal symmetric model only consider wet and dry delays in the direction of observations to find slant total delays. Troposphere mapping functions are not only used for relating slant and zenith delays but also their partial derivatives are involved in least square estimation as design matrices (Böhm and Schuh, 2013). A simple model for mapping function is $m(\varepsilon) = 1/\sin(\varepsilon)$ for planar troposphere assumption. For elevation angle higher than 20°, this mapping function is sufficiently accurate. But at lower elevation angles, bending is extremely problematic, then more accurate mapping functions are needed. So as to increase precision of mapping function, continuous fractional terms are added to simple model as follows,

$$m(\varepsilon) = \cfrac{1}{\sin(\varepsilon) + \cfrac{a}{\sin(\varepsilon) + \cfrac{b}{\sin(\varepsilon) + \cfrac{c}{\sin(\varepsilon) + \cdots}}}} \tag{4.25}$$

where $a, b, c, \cdots$ coefficients were determined with standard atmosphere data by Marini (1972). But real weather conditions were not considered. Chao (1974) used $\tan(\varepsilon)$ instead of second $\sin(\varepsilon)$ term in order to provide $m(\varepsilon) = 1$ in zenith direction, and obtained a and b coefficients from standard atmosphere. Additional constant, c, was used, and all

the coefficients were specified as a function of ray traced temperature, water vapor and total peressures by Davis et al. (1985) in addition to perspective of Chao (1974). Herring (1992a) improved continued fraction form for both hydrostatic and wet mapping functions as

$$m(\varepsilon) = \frac{1 + \dfrac{a}{1 + \dfrac{b}{1 + c}}}{\sin(\varepsilon) + \dfrac{a}{\sin(\varepsilon) + \dfrac{b}{\sin(\varepsilon) + c}}} \qquad (4.26)$$

where a, b, and c coefficients were obtained from radiosonde data as functions of height, latitude, and the temperature at receiving site. The Niell Mapping Functions (NMF) (Niell, 1996) and the Isobaric Mapping Functions (IMF) (Niell, 2000) also used this form.

For determination of NMF continued fraction form coefficients (a, b, and c) for both hydrostatic and wet mapping functions, standard atmosphere models were used. The coefficients are functions of height, latitude, and day-of-year. Validation of the NMF coefficients were done with radiosonde data during 1992. The NMF does not require meteorological parameters at receiving station. Thus, the NMF is easy to use for analysis of observations done by GNSS sites without meteorological sensor (Böhm and Schuh, 2013).

Numerical weather models were firstly used by Niell (2000) for determination of the IMF. While, b and c coefficients of Equation (4.26) were specified with using empirical functions, data provided by Schubert, Rood and Pfaendtner (1993) were used to find out a coefficients. The IMF hydrostatic (IMFh) coefficients were determined as the functions at 200hPa pressure level. For the IMF wet (IMFw), relative humidity, temperature, and pressure are needed. Some conceptual and practical restrictions for IMFw computation led Böhm and Schuh (2004) to generate the Vienna Mapping Functions (VMF).

Vienna Mapping Functions (VMF)

The VMF was developed in order to eliminate shortcomings of the IMF wet by Böhm and Schuh (2004) considering bending effect and applying vertical interpolation to weather model, e.g. European Centre for Medium-Range Weather Forecasts (ECMWF) ERA-Interim (Böhm and Schuh, 2013). It is based on directly ray tracing through numerical weather models (NMW) in the place of taking intermediate steps. For the VMF wet (VMFw) b and c coefficients were obtained from the IMFw. Besides, the VMF hydrostatic b and c coefficients were acquired from the NMFh. The VMF is named as the "fast" approach due to the fact that a coefficients of Equation (4.26) is designated with simple inversion of the fraction form with best available coefficients b and c, and mapping function value ($m(\varepsilon) = (Slant\,Total\,Delay)/(Zenith\,Total\,Delay)$) from only one ray tracing at $\varepsilon = 3.3^o$ initial

angle of elevation as

$$a = -\frac{m(\varepsilon) \cdot \sin(\varepsilon) - 1}{\dfrac{m(\varepsilon)}{sin(\varepsilon) + \dfrac{b}{sin(\varepsilon) + c}} - \dfrac{1}{1 + \dfrac{b}{1 + c}}}.$$ (4.27)

The Vienna Mapping Functions 1 (VMF1) (Böhm, Werl and Schuh, 2006) is called as successor of the VMF (Böhm and Schuh, 2004). The VMF1 b and c coefficients were updated every 6 hours from the 40-years re-analysis data (ERA-40, Uppala et al. 2005) of ECMWF containing temperature, water vapor pressure, and total pressure at profiles of 23 pressurelevels between 1000hPa to 1hPa. The c_h can be calculated using Table (4.1) as

$$c_h = c_0 + \left(\left(\cos\left(\frac{doy - 28}{365.25} \cdot 2\pi + \psi \right) + 1 \right) \cdot \frac{c_{11}}{2} + c_{10} \right) \cdot (1 - \cos(\theta)).$$ (4.28)

Table 4.1: Parameteres for computation of the c coefficient of the VMF1 hydrostatic.

Hemisphere	c_0	c_{10}	c_{11}	ψ
Northern	0.062	0.001	0.005	0
Southern	0.062	0.002	0.007	π

Determination of the a coefficients is the same as VMF "fast" approach via simple inversion given in Equation (4.27) (Böhm, Werl and Schuh, 2006; Böhm and Schuh, 2013). Validation of the VMF1 was done with "rigorous" approach which involves all the coefficients of VMF1 estimated in a least squares adjustment method with ray tracing using ten different initial angles of elevation at GPS and VLBI stations starting from station height. The latest version of the Vienna mapping functions is the VMF3 developed by Landskron and Böhm (2018) using ray-tracer delays called as RADIATE (Hofmeister and Böhm, 2017), that is based on ray-tracing method (Hobiger et al., 2008), for calculations of Equation (4.26) coefficients. The VMF3 is significantly improved version of its predecessor, the VMF1. In development of the VMF3, empiric natures of previous VMFs were conserved for assigning of b and c coefficients. As a numerical weather model ECMWF ERA-Interim (Dee et al., 2011) that succeeds the ERA-40 used in VMF1, which is ten years monthly means from 2001 to 2010, and available as 1° x 1° horizontal resolution, were used. The ERA-Interim has 37 pressure levels, and 25 of its were used for VMF3. The b and c coefficients were deduced from seasonal fit formula using mean value (A_0), amplitudes for annual variations (A_1, B_1), and semi-annual variations (A_2, B_2) of the coefficient to be calculated (b_w, b_h, c_w, and c_h) as

(Lagler et al., 2013; Böhm et al., 2015)

$$r(t) = A_0 + A_1 \cos\left(\frac{doy}{365.25}2\pi\right) + B_1 \sin\left(\frac{doy}{365.25}2\pi\right) +$$
$$A_2 \cos\left(\frac{doy}{365.25}4\pi\right) + B_2 \sin\left(\frac{doy}{365.25}4\pi\right) \tag{4.29}$$

where doy denotes day-of-year. Then, a_w and a_h coefficients were estimated using least squares adjustment using ray-traced delays over seven (outgoing) angles of elevation starting from 3°.

Global Mapping Functions (GMF)

The GMF proposed by Böhm et al. (2006) is easy to use and global version of the discrete mapping functions (IMF, Niell (2000), VMF "fast", Böhm and Schuh (2004), VMF1, Böhm, Werl and Schuh (2006), VMF3, Landskron and Böhm (2018). The GMF has the coefficients that were acquired from spherical harmonics expansion of the VMF1 (Böhm, Werl and Schuh, 2006) on a global grid. The GMF is replacement for the analysis of observations done by station where the discrete mapping functions are not available. The GMF takes longitude dependence into account with refined continued fraction form according to the NMF (Niell, 1996). To determine wet and hydrostatic a coefficients, ECMWF ERA-40 (Uppala et al., 2005) global grids for the time interval between September 1999 and August 2002 containing montly mean profiles for temperature, pressure, and humidity were applied to the same procedures as the VMF1 determination with the same b and c coefficients of the VMF1. Then, the wet and hydrostatic a coefficients for 36 months were obtained at the 312 grid points. Height corrections mentioned by Niell (1996) were applied to reduce the hydrostatic coefficients to mean sea level. The a coefficients time series for hydrostatic and wet mapping functions for each of grid points were assigned as

$$a = a_0 + A \cdot \cos\left(\frac{doy - 28}{365.25} \cdot 2\pi\right) \tag{4.30}$$

where A is the annual amplitudes, a_0 is the mean values. The phase reference of this equation is 28th day of the year for consistency with the NMF (Niell, 1996). Then, in least squares adjustments, spherical harmonic coefficients expansions were done up to order and degree 9 for both the hydrostatic and wet amplitudes A and the mean values a_0 as seen in Equation (4.31) for only a_0.

$$a_0 = \sum_{n=0}^{9} \sum_{m=0}^{n} P_{nm}(sin\theta)(A_{nm}\cos(m\lambda) + (B_{nm}\sin(m\lambda)). \tag{4.31}$$

37

where P_{nm} are the Associate Legendre Functions of the deree n and order m, θ denotes the geocentric co-latitude, and λ is the longitude. The GMF may be computed with height, longitude, latitude, and day-of-year similar to the NMF.

4.3. Troposphere Gradients

The previously mentioned azimuthal symmetry perspective basically suggested by Marini (1972); Chao (1974) is based on the assumption, that neutral atmosphere involves spherical shell slices with uniform refractive index. Height of the troposphere varies from the poles to the equator that changes the troposphere path length according to angle of azimuth (MacMillan and Ma, 1997). Troposhere gradients modeling is required for each of space-based geodetic techniques. For GNSS observations, Bar-Sever, Kroger and Borjesson (1998) shows that gradient modeling improves the estimation accuracy and precision. Troposphere zenith delays and station heights are highly correlated (Rothacher, 2002). As a consequence, any deficiency in troposphere modeling would propagate to height component as well as to all of the components of the station coordinates. The slant total delay was expressed as a sum of hydrostatic delay, wet delay, and gradient delays by MacMillan (1995) which follows previous model put forward by Davis et al. (1985, 1993) as

$$\Delta L(\alpha, \varepsilon) = \Delta L_h^z \cdot m_h(\varepsilon) + \Delta L_w^z \cdot m_w(\varepsilon) + m_g(\varepsilon)[G_n cos(\alpha) + G_e sin(\alpha)], \qquad (4.32)$$

$$m_g(\varepsilon) = m_{h,w}(\varepsilon) cot(\varepsilon) \qquad (4.33)$$

where α and ε are the angles of the azimuth (horizontal angle from geodetic North to observation direction) and the elevation, respectively. $m_h(\varepsilon)$ and $m_w(\varepsilon)$ are hydrostatic and wet mapping functions, G_n and G_e are north and east troposphere gradients. Chen and Herring (1997) proposed another gradient model as

$$m_g(\varepsilon) = \frac{1}{\sin(\varepsilon) \tan(\varepsilon) + C} \qquad (4.34)$$

where, C is assigned as 0.0031 for hydrostatic part (H=6.5km), 0.0007 for wet part (H=1.5km) from $C = 3H/R_e$ formula derived with integration where R_e is radius of the Earth. Herring (1992a) suggests to use $C = 0.0032$ for total gradient estimation. Niell (2001) obtain hydrostatic gradients from 200hPa pressure level tilting. Interpreting the gradients as illustrated in Figure (4.2) by tilting the mapping function can be done under the assumptions of flat atmosphere ($m(\varepsilon) = 1/\sin(\varepsilon)$), and tilting angle β is infinitesimal thus path delay through

zenith direction remains the same (Rothacher et al., 1998). The tilting angle β causes deflection of the path delay through zenith direction which is then called as gradient G. Resulting gradient model is the same as the model by MacMillan (1995). Estimation of the gradi-
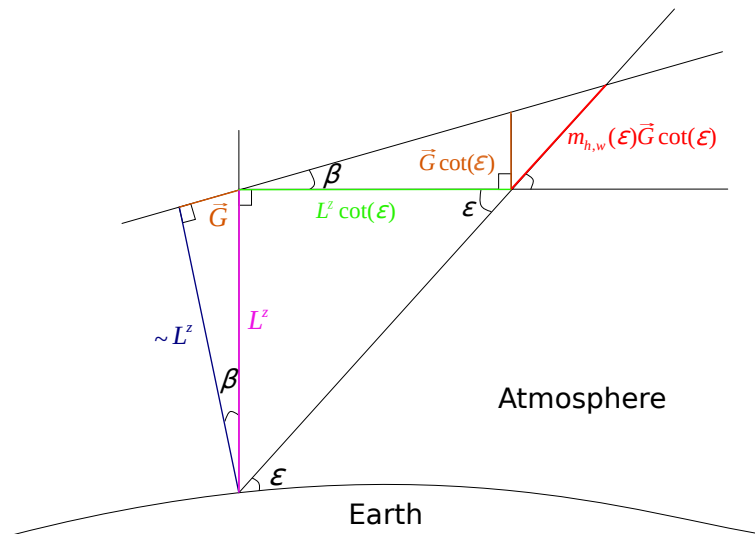
Figure 4.2: Tilted mapping function under the assumption of horizontally stratified atmosphere (Böhm and Schuh, 2013).

ents during the analysis of space geodetic techniques is important. For estimation without constraints, a priori gradient usage is not required in the analysis of sessions with enough observations to estimate all parameters simultaneously (e.g. over-determined system, see Chapter 3). Although there are many important studies related to the troposphere, because of the rapid spatio-temporal variations of especially wet contents, the troposphere is still the largest source of error in the observations of space/satellite based geodetic techniques.

5. GLOBAL NAVIGATION SATELLITE SYSTEMS (GNSS)

5.1. GNSS Fundamentals

The GNSS are one-way (space-to-earth) passive ranging systems (Hofmann-Wellenhof, Lichtenegger and Wasle, 2008). The GNSS are widely used for navigation, time transfer, and positioning purposes. There are several satellite-based navigation systems (see Table 5.1) available having either global or regional coverage with quite a lot of satellites orbiting the Earth (United Nations, 2010). Each satellite transmits signals towards the Earth continuously containing information for computation of receivers position. There are also few more regional satellite-based navigation systems such as founded by Japan and India alongside Galileo and BeiDou, which are currently regional but will be global by the year 2020. In the scope of this thesis, only the Global Positioning System (GPS) and the Global Navigation Satellite System (GLONASS) are considered because of their global coverage.

Table 5.1: Coverage of major GNSS.

System	Owner - Operator	Coverage
GPS	United States - Department of Defense (DOD)	Global
GLONASS	Russian Federation - Federal Space Agency (ROSCOSMOS)	Global
Galileo	European Union - European GNSS Agency (GSA)	Regional
BeiDou	China - National Space Administration (CNSA)	Regional

GPS

The GPS is the first fully operational space-borne global radio-positioning system (Sanz Subirana, Juan Zornoza and Hernández-Pajares, 2013). The key idea behind the development of the GPS was military force enhancement, however, they have been opened for public use with some restrictions after a while. During the last 20 years, scientific and commercial usage of the GPS has grown up. The GPS satellites are placed into 6 different orbital planes, each plane nominally consisting of 4 unequally spaced satellites (Hofmann-Wellenhof, Lichtenegger and Wasle, 2008; Dach et al., 2015). The number of the operational satellite is currently 32 (U.S. Naval Observatory, 2019) and changing due to the existence of few backup satellites but always more than 24 to guarantee at least 4 satellites needed for positioning are

available for any point on the Earth. Orbits of the GPS have inclination 55° according to the equator, and altitude above the Earth surface about 20 200 kilometers. Therefore, orbital periods of the satellites are approximately half a sidereal day ($\approx 11^h 58^m$), that means almost the same satellite constellations are repeated twice a day. The transmitters of the GPS space segment devices send navigation messages from right-hand circular polarized antennas with three different carrier signals derived from reference crystal oscillator operating at $f_0 = 10.23\ MHz$. These carriers are L_1, L_2, and L_5 with wavelengths $\lambda_1 \approx 19.0\ cm$, $\lambda_2 \approx 24.4\ cm$, and $\lambda_5 \approx 25.5\ cm$ respectively, and each owns allocated bandwidth of 24 MHz (see Table (5.2)). The coarse/acquisition (C/A) code, $C(t)$, the precision code (P), $P(t)$, and navigation message, $D(t)$ are modulated with Binary Phase Shift Keying (BPSK) onto carriers as (Baueršíma, 1982; Ávila Rodríguez, 2008)

$$L_1 = a_c\ C(t)\ D(t)\ \sin(2\pi f_1 t) + a_p\ P(t)\ D(t)\ \cos(2\pi f_1 t), \qquad (5.1)$$

$$L_2 = b_p\ P(t)\ \cos(2\pi f_2 t) \qquad (5.2)$$

where a_p, a_c, and b_p are the signal amplitudes relevant to signal power. The precision, C/A, and navigation message codes are carried to user with L_1 signal which is received by most of commercial devices (e.g. mobile phones). However, L_2 signal consists of only precise code. Devices receiving both L_1 and L_2 signals are mostly sophisticated equipment enabling ionosphere effect elimination. The GPS satellites operate with the Code Division Multiple Access (CDMA) method using orthogonal codes in order to prevent interference between different satellite signals transmitted with the same carrier frequency. Modernization of the GPS have been started with placing Block IIR-M satellites into orbit. New generation satellites are enabled to transmit new carrier frequency called as L_5, improved L_2 containing C/A code and navigation message, and few more codes (e.g. M: Military, L2C: Civilian).

Table 5.2: The GPS satellite signal constituents.

Signal	Frequency (MHz)
Base frequency	$f_0 = 10.230$
Carrier L1	$f_1 = 1\,575.420\ (154 \times f_0)$
Carrier L2	$f_2 = 1\,227.600\ (120 \times f_0)$
Carrier L5	$f_5 = 1\,176.450\ (115 \times f_0)$
P Code	$10.230\ (f_0)$
C/A Code	$1.023\ (f_0/10)$
L2C Code	$0.5115\ (f_0/20)$
Navigation Message	$50 \cdot 10^{-6}\ (f_0/204600)$

GLONASS

The GLONASS is another space-borne radio-navigation system operated and maintained by the Russian Federation space agency. There are 24 satellites orbiting the Earth on 3 orbits having an inclination of 64.8^o according to the equator and separated by 120° in the plane of the equator. Each of the orbits contains the same number of satellites spaced equally at an orbital height of 19 130 kilometers. Thus, orbital period is approximately $\approx 11^h 15^m 44^s$. Consequently, in contrast to the GPS ground track repeating once a sidereal day, a GLONASS satellite pass through the same path every eight sidereal days. In order to use a wave propagation medium called as communication channel by different satellites simultaneously, Frequency Division Multiple Access (FDMA) method is utilized in the GLONASS satellites. In contrast to CDMA used in the GPS which averting interference with orthogonal codes, the different carrier frequency is allocated for every satellite in FDMA. The frequency bands for L1 and L2 signals are f_1 and f_2 respectively, and may be found as

$$f_1(l) = 1602 + l \times 9/16 = (2848 + l) \times 9/16 \,\text{MHz} \tag{5.3}$$

$$f_2(l) = 1246 + l \times 7/16 = (2848 + l) \times 7/16 \,\text{MHz} \tag{5.4}$$

where $l = -7, ..., 6$. The antipodal satellites in the same orbit are transmitting on the same frequency (e.g. same k). Similar to the GPS, navigation message, C/A code and the precision code (P) are modulated using the BPSK modulation technique onto carrier frequencies and transmitted from right-hand circular polarized antennas. For free of charge usage, L1 and L2 bands are providing standard accuracy signals. The high-accurate service is also sent via the same frequency bands consisting of precise signals for only authorized or military users without encryption. During the upgrade of the GLONASS with K1 generation, new frequency called as L3 operating with CDMA took its place in orbit (Urlichich et al., 2011; Povalyaev, 2013). It is planned to transmit also L1 and L2 bands with both FDMA and CDMA techniques in the near future.

Table 5.3: The GLONASS satellite signal constituents.

Signal	Frequency (MHz)
Carrier L1	$1598.0625 - 1605.3750$
Carrier L2	$1242.9375 - 1248.6250$
Carrier L3	1202.025
P Code	0.511
C/A Code	5.110

5.2. GNSS Observations

Propagation duration between emission instant of signal from phase center of satellite antenna and reception instant at phase center of receiver antenna is called as travel time ΔT, and it is the basic observable of the GNSS technique (Sanz Subirana, Juan Zornoza and Hernández-Pajares, 2013). For methodology of extraction of both code pseudo-range and carrier phase observations from received signal, Tsui (2000) and Borre et al. (2007) present detailed foundations.

Code Pseudo-range

Travel time ΔT can be extracted via processing ranging codes in the GNSS signals. This process is correlation between received code and codes generated by receiver, which are exact replica of satellites' codes, in order to find maximum correlation. The observed travel time ΔT is then multiplied with speed of the light c so as to find apparent range (pseudo-range). The geometric-range or true-range differs from pseudo-range due to the error sources (e.g. asynchronous clocks, atmospheric effects, instrumental errors, etc.). Clock readings of the satellite (t^{sat}) and the receiver (t_{rcv}) are in two different time scales. Thus, pseudo-range for the P code at the carrier frequency f may be attained as

$$P_f = c[t_{rcv}(T_2) - t^{sat}(T_1)] \tag{5.5}$$

where $t_{rcv}(T_2)$ is the reception time measured with receiver clock, $t^{sat}(T_1)$ is the emission time measured with satellite clock, c is the light speed in vacuum. Pseudo-range for s^{th} satellite and frequency f may be expanded as

$$P_f^s = \rho^s + c(dt_{rcv} - dt^{sat}) + T_r^s + \alpha_f STEC + K_{f,rcv} - K_f^{sat} + \varepsilon_f \tag{5.6}$$

where

- ρ^s is distance from s^{th} satellite to receiver,

- dt_{rcv}, receiver clock error,

- dt^{sat}, satellite clock error,

- T_r^s is the non-dispersive troposphere delay through the wave path from s^{th} satellite to receiver (see Chapter 4),

- $\alpha_f STEC$ is the ionospheric delay, α_f is frequency-dependent delay per unit electron density. STEC is total electron content in the direction of observation.,

- $K_{f,rcv}$ and K_f^{sat} are frequency-dependent instrumental delays caused by hardware electronics of receiver and satellite respectively,

- ε_f is the noise term containing un-modeled parts of the observed signal.

Carrier Phase

Another ranging method used in GNSS is carrier phase measurement achieved from phase difference of received signal carrier with its replica generated by receiver. Carrier phase measurement has more accuracy compared to those of code measurement. Carrier phase measurement consists of fractional part of the carrier phase. However, unknown number of full cycle carrier wave is ambiguity term. Then, the model of the carrier phase measurement is stated as

$$\phi_f^s = \rho^s + c(dt_{rcv} - dt^{sat}) + T_r^s - \alpha_f STEC + k_{f,rcv} - k_f^{sat} + \lambda_f^s N_f^s + \epsilon_f \qquad (5.7)$$

where N_f^s is the ambiguity, λ_f^s the wavelength, $k_{f,rcv}$ and k_f^{sat} instrumental delays belong to receiver and satellite respectively, and ϵ_f the noise. The other terms are similar to those in the code pseudo-range measurements. It should be noticed that ionospheric delay term has opposite sign compared to code pseudo-range measurement due to fact that ionosphere causes group delay and phase advance (Misra and Enge, 2011).

5.3. Precise Point Positioning (PPP) Technique

Determination of receiver position can be realized with several different techniques such as those with single receiver and more than one receivers (relative positioning). Precise point positioning is a single receiver technique suggested by Zumberge et al. (1997) in order to decrease computational burden of processing observations of hundreds of receivers with utilizing precise clock and orbit as a priori information. Enhancement of PPP was proposed by Kouba and Héroux (2001) with taking into consideration minor effects in addition to those with significant impacts. These minor effects were stated in three part as the altitude of satellite, displacement of site, and consistency of used data and conventions. PPP approach aims minimizing positioning error via processing ionosphere-free linear combinations of the observations of two different frequencies introducing high accurate prior values of error sources. Ionosphere-free combination eliminates the first-order ionosphere delay ($\approx \%99.9$)

derived for code and phase observations as (Sanz Subirana, Juan Zornoza and Hernández-Pajares, 2013)

$$P_c^s = \frac{f_1^2 P_1^s - f_2^2 P_2^s}{f_1^2 - f_2^2}, \tag{5.8}$$

$$\phi_c^s = \frac{f_1^2 \phi_1^s - f_2^2 \phi_2^s}{f_1^2 - f_2^2}. \tag{5.9}$$

where, P_1^s, P_2^s and ϕ_1^s, ϕ_2^s are code and phase observations from s^{th} satellite in the f_1 and f_2 frequencies respectively. On account of CDMA method so as to distinguish different satellite signals used in the GPS, carrier frequencies f_1 and f_2 are the same for all satellites. Consequently, ionosphere-free equations are belong to the GPS L1 and L2 observations for the sake of simplicity and following derivations are based on the GPS observations only. However, same strategy may be applied for those of the GLONASS satellites by taking FDMA signal structure with various frequencies into account. After placing Equations (5.6) and (5.7) into Equations (5.8) and (5.9) respectively for $f = 1, 2$, ionosphere-free combinations are found as

$$P_c^s = \rho^s + c(dt_{rcv} - dt^{sat}) + T_r^s + K_{c,rcv} - K_c^{sat} + \varepsilon_c, \tag{5.10}$$

$$\phi_c^s = \rho^s + c(dt_{rcv} - dt^{sat}) + T_r^s + k_{c,rcv} - k_c^{sat} + \lambda_c^s N_c^s + \epsilon_c \tag{5.11}$$

where $K_{c,rcv}$, K_c^{sat}, $k_{c,rcv}$ and k_c^{sat} are receiver and satellite hardware biases of ionosphere-free combined code and phase equations, and $\lambda_c^s N_c^s$ is the ambiguity term of combined phase observation. For simplicity, hardware biases may be included by satellite and receiver clock error, and integer ambiguity term are became floating ambiguity term via involving hardware biases as (Shi and Gao, 2014)

$$c\,\tilde{dt}_{rcv} = c\,dt_{rcv} + K_{c,rcv}, \qquad c\,\tilde{dt}^{sat} = c\,dt^{sat} + K_c^{sat},$$
$$c\,\hat{dt}_{rcv} = c\,dt_{rcv} + k_{c,rcv}, \qquad c\,\hat{dt}^{sat} = c\,dt^{sat} + k_c^{sat}, \tag{5.12}$$

$$\lambda_c^s F^s = \lambda_c^s N_c^s + K_c^{sat} - K_{c,rcv} + k_{c,rcv} - k_c^{sat}. \tag{5.13}$$

Then, simplified forms of Equations (5.10) and (5.11) on account of Equations (5.12) and (5.13), and taking $T_r^s = M \cdot ZTD$ may be derived as

$$f_P = \rho^s + c(\tilde{dt}_{rcv} - \tilde{dt}^{sat}) + M \cdot ZTD + \varepsilon_c - P_c^s, \tag{5.14}$$

$$f_\phi = \rho^s + c(\tilde{dt}_{rcv} - \tilde{dt}^{sat}) + M \cdot ZTD + \lambda_c^s F^s + \epsilon_c - \phi_c^s \tag{5.15}$$

where M is the troposphere mapping function basically, and ZTD is the total delay in the zenith direction resulting from neutral atmosphere (see Chapter 4). The geometric distance between reference points (phase centers of antennas) of satellite $(X^{sat}, Y^{sat}, Z^{sat})$ and re-

ceiver $(X_{rcv}, Y_{rcv}, Z_{rcv})$ may be calculated as

$$\rho^s = \sqrt{(X^{sat} - X_{rcv})^2 + (Y^{sat} - Y_{rcv})^2 + (Z^{sat} - Z_{rcv})^2}. \qquad (5.16)$$

As seen in Equation (5.16), geometric distance is not linear. However, for least squares estimation (see Chapter 3), equations should be linearized to introduce $\sum pv^2 = min$ i.e. the condition of providing the weighted sum of squared-residuals of observations to be minimum. Then, Taylor series expansion up to first-order term should be applied around a priori values of the unknown parameters so as to approximate the non-linear equations in linear form. The functional model in matrix notation is stated as

$$v = A\delta x - l \qquad (5.17)$$

where v is the residual vector of observations, A is design matrix containing linearized equations of observations, δx is the reduced unknown parameter vector, and l is the reduced observation (observed minus computed) vector. The reduced observations vector may be formed with a priori values of satellite clock off-set dt^{sat}, troposphere delay term $T_r^s(0)$ as

$$l = \begin{bmatrix} P_c^s - \rho^s(0) + c\, dt^{sat} - T_r^s(0) \\[2mm] \phi_c^s - \rho^s(0) + c\, dt^{sat} - T_r^s(0) \end{bmatrix}. \qquad (5.18)$$

The unknown parameters are $x = \delta x + x_0$ sum of a priori parameters vector x_0 and corrections of a priori parameters vector, and these parameters are given as

$$x = [X_{rcv},\ Y_{rcv},\ Z_{rcv},\ c\tilde{d}t_{rcv},\ ZTD,\ \lambda_c^s F^s]^T. \qquad (5.19)$$

The design matrix or Jakobian matrix of the observations containing partial derivatives of code and phase observations w.r.t. estimated parameters may be derived as

$$A = \begin{bmatrix} \dfrac{\partial(f_P)}{\partial X_{rcv}} & \dfrac{\partial(f_P)}{\partial Y_{rcv}} & \dfrac{\partial(f_P)}{\partial Z_{rcv}} & \dfrac{\partial(f_P)}{\partial c\tilde{d}t_{rcv}} & \dfrac{\partial(f_P)}{\partial ZTD} & \dfrac{\partial(f_P)}{\partial \lambda_c^s F^s} \\[4mm] \dfrac{\partial(f_\phi)}{\partial X_{rcv}} & \dfrac{\partial(f_\phi)}{\partial Y_{rcv}} & \dfrac{\partial(f_\phi)}{\partial Z_{rcv}} & \dfrac{\partial(f_\phi)}{\partial c\tilde{d}t_{rcv}} & \dfrac{\partial(f_\phi)}{\partial ZTD} & \dfrac{\partial(f_\phi)}{\partial \lambda_c^s F^s} \end{bmatrix}. \qquad (5.20)$$

After partial derivatives, design matrix is found as

$$A = \begin{bmatrix} \dfrac{X_{rcv}(0) - X^{sat}}{\rho^s(0)} & \dfrac{Y_{rcv}(0) - Y^{sat}}{\rho^s(0)} & \dfrac{Z_{rcv}(0) - Z^{sat}}{\rho^s(0)} & 1 & M & 0 \\[4mm] \dfrac{X_{rcv}(0) - X^{sat}}{\rho^s(0)} & \dfrac{Y_{rcv}(0) - Y^{sat}}{\rho^s(0)} & \dfrac{Z_{rcv}(0) - Z^{sat}}{\rho^s(0)} & 1 & M & 1 \end{bmatrix}. \qquad (5.21)$$

Then, estimation of corrections of unknown parameters may be performed with weighted least squares adjustment with W weighting of observations as follows

$$\delta x = (A^T W A)^{-1} A^T W \, l. \tag{5.22}$$

5.4. Error Corrections for PPP

Ranging errors of GNSS observations arise from satellite, receiver or propagation medium. All these error sources must be modeled, reduced or estimated for accurate positioning in the way that Zumberge et al. (1997) put forward and afterward detailed by Kouba and Héroux (2001). Based on ionosphere-free combined dual frequency code and phase observations, the ionospheric delay is admitted as removed. Moreover, troposphere modeling including troposphere mapping functions and gradients was reviewed in detail at Chapter (4). The most common approach is reducing a priori hydrostatic delay from observations and estimating wet part. The rest of the error sources will be examined in upcoming passages.

5.4.1. Satellite Orbit and Clocks

Instantaneous positions of GNSS satellites are dispatched via broadcast ephemeris messages for the purpose of estimating unknown receiver position from known satellite positions. However, the accuracy of orbit assessed from the broadcast message does not satisfy the necessity of precise positioning on account of one of the major error sources is satellite orbit. Alongside orbital corrections, satellite clock is another significant error source even if clock correction polynomial constants (offset a_0, drift a_1, drift rate a_2) offered in broadcast ephemeris are used as given in Equation (5.23). As a result, the strength of the PPP approach comes from primary employment of satellite orbit and clock precise products acquired from the global network instead of the broadcast message during the estimation as recommended by Kouba and Héroux (2001).

$$\tilde{\delta t}^{sat} = a_0 + a_1(t - t_0) + a_2(t - t_0)^2. \tag{5.23}$$

IGS (Dow, Neilan and Rizos, 2009) is civilian organization established for producing GNSS derived products (e.g. satellite orbit, clock, atmosphere delays) from analyzing observations of more than 500 participating GNSS stations around the world (see current IGS network: IGS 2019a). IGS serves orbit and clock products for free of charge with various accuracy and latency criterions as seen in Table (5.4) (IGS, 2019b).

Table 5.4: The IGS orbit and clock products.

System	Type		Accuracy (RMS)	Latency	Sample Interval
GPS	Broadcast	Orbit	100 cm	Real time	Daily
		Clock	5 ns		
	Ultra-Rapid (predicted half)	Orbit	5 cm	Real time	15 min
		Clock	3 ns		
	Ultra-Rapid (observed half)	Orbit	3 cm	3-9 hours	15 min
		Clock	150 ps		
	Rapid	Orbit	2.5 cm	17-41 hours	15 min
		Clock	75 ps		5 min
	Final	Orbit	2.5 cm	12-18 days	15 min
		Clock	75 ps		30 sec
GLONASS	Final	Orbit	3 cm	12-18 days	15 min

5.4.2. Receiver Clocks

On board satellite circuits built up with precious atomic clocks put forward very precise time reference. But unfortunately, budget constraints for ground receivers induce to integrate cheaper oscillator circuits into receiving structures for timing generation. Receiver clock correction is mostly estimated along with other parameters (e.g. station coordinates, troposphere delay, etc) as given in Equation (5.19).

5.4.3. Relativistic Effects

GNSS observations suffer from relativistic effects in two ways basically: clock error and signal path error. Propagation time of emitted radio wave from the GNSS satellite is measured as a difference of clocks on satellite and ground receiver. Keeping satellite and receiver clocks synchronize is vital for precise distance measurement. Although state of the art GNSS satellites are built up with highly accurate and stable clocks, relativistic clock corrections must be applied in addition to clock corrections done with the coefficients in either broadcast message or clock solution files served by the IGS (Kouba, 2004). The relativistic clock correction may be investigated as a sum of constant correction Δt_{con} and periodic correction Δt_{per} as follows

$$\Delta t_{rel} = \Delta t_{con} + \Delta t_{per}. \tag{5.24}$$

The constant relativistic effects have an impact on nominal frequency because of both orbital speed of satellite (special relativity) and gravitational attractions on satellite (general relativity) as,

$$\frac{\Delta f}{f_0} = \frac{f - f_0}{f_0} = \frac{v^2}{2c^2} + \frac{\Delta U}{c^2}. \tag{5.25}$$

where v is the relative velocity of satellite clock according to receiver clock, c is vacuum speed of the light, and ΔU is the gravitational potential difference between orbit of satellite and the geoid. For satellites of GPS, $\Delta f/f_0 = 446.47 \cdot 10^{-12}$.

Strictly speaking, effect of General Relativity is leading faster elapse of satellite clocks in proportional to altitude. Nevertheless, due to Special relativity, as orbital velocity of satellite increases, on board clock slows down. The periodic part in Equation (5.24) is arising from the orbital eccentricity of the satellite. This effect also contains orbital perturbations. Position vector $\vec{r}$ and velocity vector $\vec{v}$ of the satellite at transmission instant determines clock correction due to eccentricity as defined in following equation (Ashby, 2003)

$$\Delta t_{ecc} = 2\frac{\vec{r} \cdot \vec{v}}{c^2}. \tag{5.26}$$

Path range error due to relativity so-called Shapiro time delay should be considered for precise positioning purposes so as to improve accuracy for a few centimeters. This effect directly delays GNSS radio wave by space-time dilation. Path error may be derived as

$$\Delta \rho_{rel} = 2\frac{\mu}{c^2}ln\frac{r^{sat} + r_{rcv} + r_{rcv}^{sat}}{r^{sat} + r_{rcv} - r_{rcv}^{sat}}. \tag{5.27}$$

Here, μ indicated gravitational constant of the Earth, r_{rcv} and r^{sat} denote geometric distances of the receiver and satellite respectively, and r_{rcv}^{sat} is the distance between receiver and satellite.

5.4.4. Antenna Phase Center

The instantaneous phase center of an antenna changes with frequency and direction of transmission/reception. In order to define coordinates of satellite and receiver, reference points are defined on the device. The fixed point for the satellite is its center of mass; nonetheless, the antenna reference point of the receiver (ARP) is defined and marked by the manufacturer. Variations between actual phase centers and reference points should be taken into consideration for precise positioning (Kouba and Héroux, 2001). The instantaneous satellite antenna

phase center $\vec{X}_{APC}$ is found as

$$\vec{X}_{APC} = \vec{X}_M - \overrightarrow{PCO} - \overrightarrow{PCV} \tag{5.28}$$

where $\vec{X}_M$ is the center of mass of the satellite, which is referred as satellite coordinate in precise orbit. $\overrightarrow{PCO}$ is mean phase center called as phase center offset, and $\overrightarrow{PCV}$ defines variations of real phase center for particular frequency and signal direction from $\overrightarrow{PCO}$. Publicly available values of PCO and PCV for satellites may be downloaded in ANTEX format from IGS (Schmid et al., 2016).

Similarly, true phase center for receiver suffer from antenna phase pattern and phyiscal protector so-called radome on antenna. Calibration for various antenna and radome pairs are carried out with anechoic chamber or robot (Dach et al., 2015).

5.4.5. Phase Wind-up

In order for high precision positioning, the wind-up effect at carrier phase observation, which is due to circular polarized radio wave, should be considered. During the orbital motion of GNSS satellites, they keep rotate for gaining maximum energy from the sun. This motion leads phase variation thereby mistake for range measurement. The phase wind-up correction for crossed dipole antenna may be calculated as (Wu et al., 1993)

$$\Delta\phi = \delta\phi + 2N\pi \tag{5.29}$$

where fractional piece of a period $\delta\phi$ is found using unit vector from satellite to receiver, $\hat{\boldsymbol{\rho}}$ and effective dipoles for satellite and receiver labeled as $\boldsymbol{d'}$ and $\boldsymbol{d}$ as given in following equation

$$\delta\phi = sign(\hat{\boldsymbol{\rho}}\,(\boldsymbol{d'} \times \boldsymbol{d}))\arccos\left(\frac{\boldsymbol{d'} \cdot \boldsymbol{d}}{|\boldsymbol{d'}|\,|\boldsymbol{d}|}\right) \tag{5.30}$$

and integer N, which is initially treated as zero, may be calculated via rounding to the nearest integer as

$$N = \left\lfloor \frac{\Delta\phi_{prev} - \delta\phi}{2\pi} \right\rceil \tag{5.31}$$

where $\Delta\phi_{prev}$ is previous phase correction value. The effective dipoles are obtained as

$$\boldsymbol{d'} = \hat{\boldsymbol{x}}' - \hat{\boldsymbol{\rho}}\,(\hat{\boldsymbol{\rho}} \cdot \hat{\boldsymbol{x}}') + \hat{\boldsymbol{\rho}} \times \hat{\boldsymbol{y}}'$$
$$\boldsymbol{d} = \hat{\boldsymbol{x}} - \hat{\boldsymbol{\rho}}\,(\hat{\boldsymbol{\rho}} \cdot \hat{\boldsymbol{x}}) + \hat{\boldsymbol{\rho}} \times \hat{\boldsymbol{y}} \tag{5.32}$$

where unit vectors of local receiver $(\hat{\boldsymbol{x}}, \hat{\boldsymbol{y}}, \hat{\boldsymbol{z}})$, and unit vectors of satellite body $(\hat{\boldsymbol{x}}', \hat{\boldsymbol{y}}', \hat{\boldsymbol{z}}')$

5.4.6. Differential Code Biases

Hardware related delays for satellite and receiver are called as differential code biases (DCB) so that every type of transmitter/receiver circuits have its own DCB. While, biases cause group delays for code observations, their effects on phase observations are perceived as gathered into ambiguity parameter. These biases must be regarded for single frequency receivers as well as dual frequency observations' linear combination (ionosphere-free). (Leandro, Langley and Santos, 2007; Montenbruck and Hauschild, 2013). Despite satellite circuit based delays are needed to be corrected with proper DCB values, delays due to receiver circuits are handled while receiver clock are being estimated because of DCB error propagation into clock parameters. For this purpose, some GNSS agencies are producing DCB corrections for monthly periods (Schaer, 2012).

5.4.7. Displacements of Crust-fixed Reference Points

Solid Earth Tides

Gravitational forces due to the Moon and the Sun are driving the solid Earth to move in tidal periods as well as permanently. Tidal frequency and geographic location specific Love and Shida numbers scale a spherical harmonic expansion to represent site displacement (Wahr, 1981a). In IERS 2010 conventions (Petit and Luzum, 2010), crust-fixed point displacement is calculated with firstly degree: 2 and degree: 3 tides followed by Love and Shida numbers frequency dependence. Tides with degree: 2 causes displacement as given below:

$$\Delta \overrightarrow{r} = \sum_{j=2}^{3} \frac{GM_j R_e^4}{GM_\oplus R_j^3} \left\{ h_2 \hat{\mathbf{r}} \left(\frac{3(\hat{\mathbf{R}}_j \cdot \hat{\mathbf{r}})^2 - 1}{2} \right) + 3\, l_2 \, (\hat{\mathbf{R}}_j \cdot \hat{\mathbf{r}}) \left[\hat{\mathbf{R}}_j - (\hat{\mathbf{R}}_j \cdot \hat{\mathbf{r}}) \, \hat{\mathbf{r}} \right] \right\} \quad (5.33)$$

where $GM_\oplus$, GM_2 and GM_3 are the gravitational parameters belong to the Earth, the Moon and the Sun respectively. $\hat{\mathbf{R}}_2$ and R_2 are unit vector and its magnitude, which are defined from the geocenter and to the Moon; besides $\hat{\mathbf{R}}_3$ and R_3 are defined between the geocenter and the Sun. R_e is equatorial radius of the Earth. Between geocenter and station, unit vector $\hat{\mathbf{r}}$ and its magnitude r are established. Degree:2 Love and Shida numbers are h_2 and l_2 respectively. Nominal values of these numbers are corrected using station latitude as follows:

$$h_2 = 0.6078 - 0.0006 \left[(3 \sin^2 (\varphi) - 1)/2 \right] \quad (5.34)$$

and

$$l_2 = 0.0847 + 0.0002 \left[(3 \sin^2 (\varphi) - 1)/2 \right]. \quad (5.35)$$

where φ is station geocentric latitude. Degree:3 caused displacement is given as

$$\Delta \vec{r} = \sum_{j=2}^{3} \frac{GM_j R_e^5}{GM_\oplus R_j^4} \left\{ h_3 \, \hat{\mathbf{r}} \left(\frac{5(\hat{\mathbf{R}}_j \cdot \hat{\mathbf{r}})^3 - 3(\hat{\mathbf{R}}_j \cdot \hat{\mathbf{r}})}{2} \right) + l_3 \left(\frac{15(\hat{\mathbf{R}}_j \cdot \hat{\mathbf{r}})^2 - 3}{2} \right) \left[\hat{\mathbf{R}}_j - (\hat{\mathbf{R}}_j \cdot \hat{\mathbf{r}}) \, \hat{\mathbf{r}} \right] \right\}. \tag{5.36}$$

Here, contribution of the Sun is insignificant (Petit and Luzum, 2010). The time invariant part of the tidal displacement so-called permanent deformation in radial and transverse components, r and t, respectively may be calculated as

$$r = [-0.1206 + 0.0001 \, P_2(\sin \varphi)] \, P_2(\sin \varphi), \tag{5.37}$$

$$t = [-0.0252 - 0.0001 \, P_2(\sin \varphi)] \, (\sin \varphi). \tag{5.38}$$

Ocean and Hydrology Loading

The displacement at the station caused by loading effects of the ocean tides is another significant crust movement mostly occurs in coastal zones. In order for inland areas as well, ocean tidal loading (OTL) effects should be considered. The mass redistribution at the ocean induced by the celestial bodies gravitational attractions cause loading effects at sub-daily, daily, fortnightly, monthly, semi-annual periods. So as to compute ocean tidal loading induced site displacements, following equation is provided as (Scherneck, 1999; Petit and Luzum, 2010)

$$\Delta c = \sum_{j=1}^{11} f_j A_{cj} \cos(\omega_j t + \lambda_j + u_j - \Phi_{cj}) \tag{5.39}$$

where corresponding 11 tides are M_2, S_2, K_2 and N_2 in semi-diurnal periods, O_1, K_1, P_1 and Q_1 in diurnal periods, and M_{mf}, M_m and M_{sa} in periods from 2 weeks to 6 months. f_j and u_j are the modulation effect of the longitude of lunar node. λ_j represents the astronomical argument for t=0 h, and ω_j is the angular velocity. The station specific A_{cj} and Φ_{cj} components are site specific amplitude and phase as w.r.t. Greenwich, respectively, and they are derived from ocean tide model (e.g. FES2004, see Lyard et al. 2006). Besides tidal variations, non-tidal ocean loading arising from sea surface height and water column density changes is another important reason for site displacement, which causes errors at clock corrections and zenith wet delay estimation by error propagation (Vey et al., 2002). Unlike tidal variations, non-tidal part is still un-modeled.

Another site displacement due to annual variations of surface water storage (e.g. snow, ice, soil moisture, ground water, etc.) is not negligible and reaches up to 30 mm in vertical component (Schuh et al., 2003).

Tidal and Non-tidal Atmosphere Loading

Variations at atmosphere heat induce oscillations of surface pressure. Response of the Earth for pressure change from reference values is site displacement (vanDam, Blewitt and Heflin, 1994; Petrov and Boy, 2004; Petit and Luzum, 2010). The tidal and non-tidal movements caused by atmosphere loading do exist. In contrast to ocean loading, non-tidal part of atmosphere loading has much more influence compared to tidal part. The tidal part consists of diurnal tide called as S_1 and semi-diurnal S_2 tide. The tidal vertical displacement model established by Ray and Ponte (2003). Sub-daily model (tidal) is derived to calculate displacements caused by S_1 and S_2 from global surface pressures of the ECMWF. These displacements in up, east and north directions (n, e, u) are found as

$$\Delta(u, e, n)_{S_1} = A_{d1}(u, e, n) \cos(\omega_1 T) + B_{d1}(u, e, n) \sin(\omega_1 T), \qquad (5.40)$$

$$\Delta(u, e, n)_{S_2} = A_{d2}(u, e, n) \cos(\omega_2 T) + B_{d2}(u, e, n) \sin(\omega_2 T) \qquad (5.41)$$

where A_{d1}, A_{d2}, B_{d1} and B_{d2} are amplitudes of model, T is Universal Time (UT1) in days, and ω_1, ω_2 are frequencies of the model. Site specific amplitudes (A_{d1}, A_{d2}, B_{d1}, B_{d2}) are determined with Green's function global convolution sum with pressure mass coefficients.

Pole Tides

Instantaneous Earth rotation axis w.r.t. the crust is varying with time, that is leading deformations up to several cm (Petit and Luzum, 2010). The pole tide correction is needed for high precision positioning as well. The latitude correction $\Delta\varphi$, the longitude correction $\Delta\lambda$ and the height corrections Δr are expressed as

$$\begin{aligned}
\Delta\varphi &= -9 \cos(2\varphi) \left[(X_p - \overline{X}_p) \cos\lambda - (Y_p - \overline{Y}_p) \sin\lambda \right], \\
\Delta\lambda &= 9 \cos\varphi \left[(X_p - \overline{X}_p) \sin\lambda + (Y_p - \overline{Y}_p) \cos\lambda \right], \qquad (5.42) \\
\Delta r &= -33 \sin 2\varphi \left[(X_p - \overline{X}_p) \cos\lambda - (Y_p - \overline{Y}_p) \sin\lambda \right]
\end{aligned}$$

where φ is latitude, and λ indicates longitude of station, $(X_p - \overline{X}_p)$ and $(Y_p - \overline{Y}_p)$ denote the pole coordinate variation from the mean pole $(\overline{X}_p, \overline{Y}_p)$

Tectonic Plate Motion

Tectonic plates are continuously moving, that changes the crust-fixed station coordinates (Dach et al., 2015). This effect is considered by shifting station coordinates from reference

epoch, which is the time reference (estimation epoch) of the initial coordinates of geodetic control stations, to the epoch of observation by using corresponding station's linear velocities. Mentioned site specific velocities are available for IGS stations, and may be computed for stations without velocity information with model provided by DeMets et al. (1994)

6. VERY LONG BASELINE INTERFEROMETRY (VLBI)

6.1. VLBI Delay Model

VLBI is a space-based geodetic technique that receives radio-waves emitted from bright and distant galaxies called as quasar (quasi-stellar radio source) by multiple radio telescopes. VLBI utilizes huge parabolic reflector antennas located around the Earth continents to collect radio signals reaching on it. The measurement principle of VLBI is based on arrival time differences of signals received by two or more antennas (Figure 6.1).
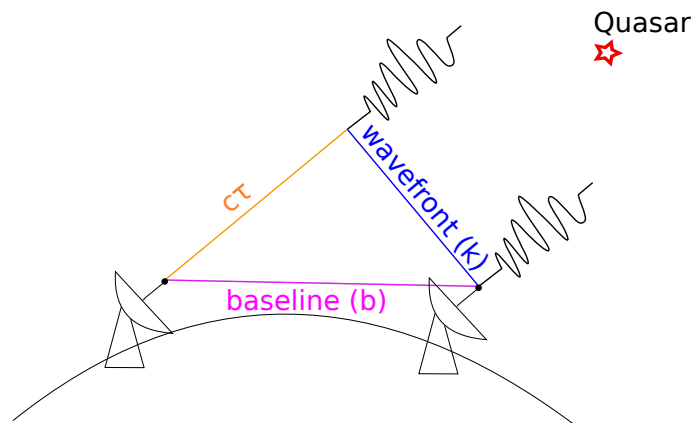
Figure 6.1: VLBI observation principle.

This technique made many important contribution to global geodesy, geophysics, astrometry and astrophysics (Sovers, Fanselow and Jacobs, 1998; Campbell, 2000; Kellermann and Moran, 2001; Schlüter and Behrend, 2007; Teke, 2011; Teke et al., 2012; Schuh and Behrend, 2012; Schuh and Böhm, 2013). VLBI is the unique technique for determination of the space-fixed reference frame (i.e. ICRF2, Fey, Gordon and Jacobs 2009) that contains quasar's angular positions. Besides, Global VLBI network has a significant role on precise determination of the crust-fixed reference stations position named as terrestrial reference frame (i.e. ITRF14, Altamimi et al. 2016) by monitoring variations of Earth orientation. State-of-the-art VLBI equipment has sub-centimeter accuracy for determination of intercontinental baselines (Schlüter and Behrend, 2007). VLBI is the fundamental and unique technique for estimation of the full set of Earth orientation parameters. Accurate determination of celestial and terrestrial reference frames have an essential role in space missions, atmospheric studies, oceanic level monitoring and improvements of other geodetic techniques such as GNSS, DORIS, SLR/LLR. Besides scientific contributions as well as, technological and technical progress of VLBI are contributing to navigation and positioning in space and on Earth.

IVS is responsible for arranging VLBI observing sessions by the participation of stations around the Earth. During the VLBI session with multiple antennas, different subsets of antennas may observe various sources. The VLBI antennas are able to slew ranging from a few seconds to a few minutes for observing different sources (Sovers, Fanselow and Jacobs, 1998). If at least two VLBI antennas are steered to the direction of a quasar and captured the signal, it is called as a scan. The scan contains valuable information about Earth orientation, the position of quasars and the position of receiving antennas. The principle of VLBI is straightforward. Extra-galactic radio sources (quasars) distributed on the sky are emitting signals in radio-wave frequency bands. Current VLBI receivers are sensitive to electromagnetic radio waves at 2.2-2.4 GHz (S-band) and 8.2-8.95 GHz (X-band). According to VLBI2010 prospective, this limited bandwidth should be expanded to four-band receivers operating up to 14 GHz (Petrachenko et al., 2009). This radiation arrives on Earth as a planar wave. VLBI antenna receives and records the signal, then marks the signal with time-tag using very precise and stable hydrogen maser clock. Soon after, these data are sent to the correlators located in the USA, in Germany, and in Japan for a cross-correlation process.

Extraction of τ from recorded signals by VLBI antennas involve correlation procedure. For two antenna voltages represented as $V_1(t)$ and $V_2(t)$ varying with time t, then cross-correlation function

$$R(\tau) = \frac{1}{T} \int_0^T V_1(t) \cdot V_2^*(t - \tau) \cdot dt \qquad (6.1)$$

should be maximized in order to find out the group delay τ over time interval T. Note that asterisk denotes the complex conjugate. Due to rotation of the Earth, VLBI observation around X band (8.4 GHz) is effected by Doppler shifts. This leads to oscillation at these frequencies up to several kilohertz if it is not 'counter-rotated' (Sovers, Fanselow and Jacobs, 1998). Phases and amplitudes are determined in parallel for every 1-2 s ω_i while correlator computer is processing for 14 frequency channels. During the post-correlation stage, correction for the phase calibration and fitting the group delay τ_{gd}, the phase ϕ_0 and the phase rate τ'_{pd} to the phase samples $\phi(\omega_i, t_j)$ from the different frequency channels ω_i and times t_j are applied. The phase-derived observables are specified (for circular frequency ω and phase ϕ) from a bi-linear Least-squares fit to the measured phases $\phi(\omega, t)$ from (Sovers, Fanselow and Jacobs, 1998)

$$\phi(\omega, t) = \phi_0(\omega_0, t_0) + \frac{d\phi}{d\omega}(\omega - \omega_0) + \frac{d\phi}{dt}(t - t_0) \qquad (6.2)$$

where the group delay τ_{gd}, the phase delay τ_{pd} and phase delay rate τ'_{pd} are extracted as follows

$$\tau_{gd} = \frac{d\phi}{d\omega}, \tau_{pd} = \frac{\phi_0}{\omega_0}, \tau'_{pd} = \frac{1}{\omega_0}\frac{\phi}{dt}. \qquad (6.3)$$

To emphasize: phase delay, phase delay rate, group delay and amplitude are the products of the interferometer. For geodetic purposes, the group delay rate τ'_{gd} should not be used

due to its low accuracy. Instead, group delay ambiguity resolution needs the group delay rate in a first solution step (Schuh and Böhm, 2013). Amplitudes are not commonly used for geodetic and astrometric purposes of VLBI data analysis (Sovers, Fanselow and Jacobs, 1998). The phase delay is providing high accuracy on very short baselines (Herring, 1992b; Petrov, 1999). The phase ambiguities are not solved for long baselines yet. The group delay is now fundamental observable of geodetic VLBI. The group delay resolution

$$\sigma_\tau = \frac{1}{2\pi} \cdot \frac{1}{SNR \cdot B_{eff}} \tag{6.4}$$

where SNR is the signal-to-noise-ratio, and B_{eff} is the root-mean-square (RMS) spanned bandwith (Rogers, 1970). Besides, SNR changes according to the digital loss factor η, the correlation amplitude ρ_0, the recorded bandwidth B and the coherent integration time T (Takahashi et al., 2000) as

$$SNR = \eta \cdot \rho_0 \cdot \sqrt{2 \cdot B \cdot T}. \tag{6.5}$$

The VLBI delay model for geodetic parameter estimation can be simply stated as,

$$-c \cdot \tau = \vec{b} \cdot \vec{k} + \Delta\tau_{retarded\,baseline} + \Delta\tau_{clock} + \Delta\tau_{trop} + \Delta\tau_{iono} + \cdots \tag{6.6}$$

where

- c is the velocity of light in vacuum environment,

- $\vec{k}$ is the unit source vector that is the wavefront propagation direction in BCRS,

- $\vec{b}$ is the baseline vector defined TRS,

- $\Delta\tau_{retarded\,baseline}$ is the delay correction owing to the fact that the radio-wave reaches to the first antenna before the second one. The instantaneous position of the second VLBI antenna is changed by Earth rotation in GCRS during the wave is traveling (Cohen and Shaffer, 1971),

- $\Delta\tau_{clock}$ is the delay correction caused by asynchronous atomic clocks of stations ($\tau_{clk1} - \tau_{clk2}$),

- $\Delta\tau_{trop}$ is the delay correction due to troposphere ($\tau_{trop1} - \tau_{trop2}$),

- $\Delta\tau_{iono}$ is the delay correction due to ionosphere ($\tau_{iono1} - \tau_{iono2}$).

The present-day VLBI delay model is exhibited by IERS Conventions named as "consensus model" developed from five different relativistic delay models combination (Petit and Luzum, 2010). Positions of VLBI antennas are defined in the ITRS which is Earth-fixed and

Earth-centered Cartesian coordinate system. However, quasar positions given in the ICRF catalogue are defined in a space-fixed coordinate system called as BCRS. The origin of the BCRS is the centre of the mass of the Solar system. Another celestial coordinate system is the GCRS which has its origin at the centre of the mass of the Earth. The calculated delay is the arrival time difference of receiving antenna 2, t_2, and receiving antenna 1, t_1 in GCRS. VLBI atomic clocks synchronized to UTC. For the calculation of the tidal effects (e.g. solid Earth tide, ocean tidal loading, pole tide, non-tidal and tidal atmosphere loading) so as to correct the a priori ITRS catalogue coordinates of VLBI antennas, UTC time scale should be converted to the terrestrial time (TT) scale. Most of the geodynamical models require terrestrial time TT for calculation. From definition: $TT - TAI = 32.184 \; seconds$ and $TAI - UTC = leap \; seconds$ (Petit and Luzum, 2010). For the observation epoch, t_1 that is defined in terrestrial time scale and units of MJD may be written as

$$TT = t_1 + (32.184 + leap \; seconds)/86400. \qquad (6.7)$$

Then, Julian centuries since standard epoch (J2000, 01.01.2000, 12 UT) in TT time frame for t_1 is found

$$t = (TT - 51544.5)/36525. \qquad (6.8)$$

ITRS coordinates of the antenna at that scan epoch are (X_{ITRS}). Then, it can be transformed to GCRS at observation epoch with the transformation matrices $Q(t)$, $R(t)$ and $W(t)$ as

$$X_{GCRS} = Q(t) \cdot R(t) \cdot W(t) \cdot X_{ITRS}. \qquad (6.9)$$

- The Wobble matrix, $W(t)$ is based on the motion of CIP position in TRS (polar motion),

- The rotation matrix, $R(t)$ is based Earth rotation around the pole,

- The Nutation/precession matrix, $Q(t)$ is based on the motion of the CIP position in the GCRS.

The Wobble matrix, $W(t)$ may be expressed as

$$W(t) = R_3(s') \cdot R_2(x_p) \cdot R_1(y_p), \qquad (6.10)$$

where x_p and y_p are ITRS coordinates of CIP. The rotation matrices R_1, R_2 and R_3 describes rotation around 1st, 2nd and 3rd axes, respectively in positive angle. s' is the position of TIO on the instantaneous CIP equator which corresponds to the definition of the non-rotating origin (NRO) in the ITRS at epoch t. TIO locater, s' is not effected by the variations of

polar motion with small amplitudes (i.e. sub-daily variations). Then, it can be calculated with mean amplitudes of the annual and Chandler ($\sim$433 days period) wobbles as follows (Capitaine, Guinot and Souchay, 1986; Lambert and Bizouard, 2002)

$$s' = -47 \cdot 10^{-6} \cdot t. \tag{6.11}$$

Rotation matrix involves rotation of Earth around the axis of CIP given as

$$R(t) = R_3(-\theta(t_u)) \tag{6.12}$$

where θ denotes the Earth Rotation Angle (ERA) also called as stellar angle which is the angle observed from CIO to TIO on the CIP equator. Then, the θ can be calculated from

$$\theta(t_u) = 2\pi \left(0.7790572732640 + 1.00273781191135448 \cdot (t_{UT1} - 54544.5)\right) \tag{6.13}$$

where constants are arising from Capitaine, Guinot and McCarthy (2000). t_{UT1} is Universal Time at the epoch of observation defined in MJD time frame may be found as

$$t_{UT1} = t_1 + \Delta UT1/86400. \tag{6.14}$$

The nutation/precession matrix involving the motion of the CIP in the GCRS may be revealed as
$$Q(t) = R_3(-E) \cdot R_2(-d) \cdot R_3(E) \cdot R_3(s) \tag{6.15}$$

where E and d values are found using the CIP coordinates in GCRS as follows:

$$E = \arctan \frac{Y}{X}, \tag{6.16}$$

$$d = \arccos\left(\sqrt{1 - X^2 + Y^2}\right), \tag{6.17}$$

and the s called as CIO locator is denoting the position of the CIO on the CIP equator which corresponds to definition of the non-rotating origin (NRO) in the GCRS when the CIP is moving according to the GCRS under the effects of nutation and precession, from the standard epoch to the epoch of interest t_1 as (Capitaine, Guinot and McCarthy, 2000; Petit and Luzum, 2010)

$$s = s_0 - \frac{XY}{2}. \tag{6.18}$$

6.1.1. Gravitational Delay

As stated in General Relativity Theory (GRT), an electromagnetic wave propagating through a gravitational potential is retarded according to its travel time through field-free space (Einstein, 1916). Not only time delay but also diverging from straight-line path occurs by gravitational attraction (Shapiro, 1964, 1967). Electromagnetic wave emitted from quasar is under the effect of gravity before received. Thus, gravitational delay corrections must be applied to observations of VLBI a priori to the parameter estimation (Sovers, Fanselow and Jacobs, 1998). Following derivations are based on Sovers, Fanselow and Jacobs (1998); Kopeikin and Schafer (1999); Petit and Luzum (2010). Assuming arrival time for station 1, t_1 is the time reference for the observation, and it is converted to appropriate time system for using in geometric model calculations. Then, the barycentric coordinates (station vectors) $\vec{X}_i(t_1)$ for the receiving antenna

$$\vec{X}_i(t_1) = \vec{X}_\oplus(t_1) + \vec{x}_i(t_1), \tag{6.19}$$

where t_1 is the arrival time of the radio signal for the first receiver, $\vec{X}_\oplus(t_1)$ is the barycentric coordinates (radius vector) of the geocenter, and $\vec{x}_i(t_1)$ is the GCRS coordinates (radius vector) of the ith receiver. Then, in order to compute $\vec{R}_{iJ}$ which is the vector from the Moon, the Sun and each of other planets apart from Earth to receivers 1 and 2, the time t_{1J} when the wave is propagating near to the Jth gravitating body can be calculated with

$$t_{1J} = t_1 - \frac{\vec{K}(\vec{X}_J(t_1) - \vec{X}_1(t_1))}{c}, \tag{6.20}$$

where $\vec{X}_J$ defining the barycentric coordinate of the Jth gravitating body can be calculated using the barycentric velocity of the Jth gravitating body $\vec{V}_J$ as

$$\vec{X}_J(t_{1J}) = \vec{X}_J(t_1) + \vec{V}_J(t_{1J} - t_1) \tag{6.21}$$

and $\vec{K}$ is the barycentric unit source vector

$$\vec{K} = \begin{bmatrix} \cos\delta\cos\alpha & \cos\delta\sin\alpha & \sin\delta \end{bmatrix}, \tag{6.22}$$

where α is right ascension and δ is declination of source defined in the BCRS without gravitational and aberrational bending. Then, the vector from the Jth gravitating body to the antenna 1 and 2 respectively as

$$\vec{R}_{1J}(t_1) = \vec{X}_1(t_1) - \vec{X}_J(t_{1J})$$

$$\vec{R}_{2J} = \vec{X}_2(t_1) - \frac{\vec{v}_\oplus}{c}(\vec{K} \cdot \vec{b}) - \vec{X}_J(t_{1J}) \tag{6.23}$$

where $\vec{V}_{\oplus}$ is the velocity of the geocenter according to barycenter, c is velocity of light in vacuum, and $\vec{b}$ is the baseline vector when the signal is received by the first antenna. The differential Barycentric Coordinate Time (TCB) gravitational delay for J^{th} gravitating body may be stated as

$$\Delta T_{gravJ} = (1 + \gamma) \frac{\mu_J}{c^3} \ln \frac{|\vec{R}_{1J}| + \vec{K} \cdot \vec{R}_{1J}}{|\vec{R}_{2J}| + \vec{K} \cdot \vec{R}_{2J}}, \tag{6.24}$$

where γ light deflection parameter may be assumed as unity in GRT (Sovers, Fanselow and Jacobs, 1998; Schuh and Böhm, 2013), and μ_J is the standard gravitational parameter which can be determined via space geodetic missions with higher precision than determination of gravitational constant G and the rest or invariant mass of the Jth gravitating body M_J. Relation between these parameters may be stated as

$$\mu_J = GM_J. \tag{6.25}$$

In similar manner, gravitational delay owing to the Earth

$$\Delta T_{grav\oplus} = (1 + \gamma) \frac{GM_{\oplus}}{c^3} \ln \frac{|\vec{x}_1| + \vec{K} \cdot \vec{x}_1}{|\vec{x}_2| + \vec{K} \cdot \vec{x}_2}, \tag{6.26}$$

where $\vec{x}_i$ is coordinates of the ith receiver at epoch t_1 in the GCRS, and $M_{\oplus}$ is the invariant mass of the Earth (Kopeikin and Schafer, 1999; Petit and Luzum, 2010). Consequently, sum of all gravitational delays caused by the Earth and other gravitating bodies

$$\Delta T_{grav} = \sum_j \Delta T_{gravJ}. \tag{6.27}$$

Higher order terms of relativistic time delay should be taken into account for the rays that are passing close to massive bodies especially the Sun and Jupiter. As described by Richter and Matzner (1983) and Hellings (1986), the ray path bending by the gravitating body J is the largest correction that can be found as

$$\delta T_{grav,J} = \frac{4G^2 M_J^2}{c^5} \frac{\vec{b} \cdot (\vec{N_{1J}} + \vec{K})}{(|\vec{R}_{1J}| + \vec{R_{1J}} \cdot \vec{K})^2}, \tag{6.28}$$

and it should be added to the sum in Equation (6.27). $\vec{N_{1J}}$ is the unit vector between the Jth gravitating body and the first antenna.

6.1.2. Geometric and Vacuum Delays

The vacuum delay in the barycentric frame may be found with approximation up to sufficient level as (Petit and Luzum, 2010)

$$T_2 - T_1 = -\frac{1}{c}\vec{K} \cdot (\vec{X}_2(T_2) - \vec{X}_1(T_1)) + \Delta T_{grav}. \tag{6.29}$$

Then, transformation from T_2-T_1 to t_2-t_1 which is actually transformation from barycentric to geocentric time may be performed by applying the relativistic transformations. Considering gravitational delay but ignoring the atmospheric bending and the atmospheric delay, the total vacuum delay in geocentric coordinate time (TCG) between arrival times of the second receiver t_{v2} and the first receiver t_{v1} (Kopeikin, 1990; Eubanks, 1991; Shahid-Saless, Hellings and Ashby, 1991; Soffel et al., 1991; Treuhaft and Thomas, 1991; Sovers and Jacobs, 1994).

$$t_{v2} - t_{v1} = \frac{\Delta T_{grav} - \frac{\vec{K}\cdot\vec{b}}{c}[1 - \frac{(1+\gamma)\cdot U}{c^2} - \frac{|\vec{V}_\oplus|^2}{2c^2} - \frac{\vec{V}_\oplus\cdot\vec{\omega}_2}{c^2}] - \frac{\vec{V}_\oplus\cdot\vec{b}}{c^2}(1 + \vec{K}\cdot\vec{V}_\oplus/2c)}{1 + \frac{\vec{K}\cdot(\vec{V}_\oplus+\vec{\omega}_2)}{c}}, \tag{6.30}$$

where ω_i is the velocity of the ith receiver according to geocenter, and the gravitational potential at the center of the Earth U may be expressed as

$$U = \frac{GM_\odot}{|\vec{R}_{\oplus\odot}|}, \tag{6.31}$$

where $M_\odot$ is the invariant mass of the Sun, and the $\vec{R}_{\oplus\odot}$ is the vector from the Sun to the geocenter. Planetary ephemerides are proving the vectors $\vec{X}_\oplus$, $\vec{V}_\oplus$, $\vec{X}_J$, $\vec{V}_J$ used for gravitational and vacuum delay calculations. Geometric and propagation delays are the parts of total delay. The geometric delay part is stated as

$$t_{g2} - t_{g1} = t_{v2} - t_{v1} + \delta t_{atm1}\frac{\vec{K}(\vec{\omega}_2 - \vec{\omega}_1)}{c}, \tag{6.32}$$

where δt_{atm1} is the hydrostatic delay at receiver 1 for the observation epoch t_1 (Teke, 2011)

$$\delta t_{atm1} = \frac{\Delta L_h^{st(1)}(t_1) \cdot m_h^{st(1)}(\varepsilon, t_1)}{c}, \tag{6.33}$$

where $\Delta L_h^{st(1)}(t_1)$ is the dry troposphere delay at the zenith direction at receiver 1 for epoch t_1, ε denotes the elevation angle, and m_h is the dry mapping function. Then, adding the propagation delay leads to total delay as

$$t_2 - t_1 = t_{v2} - t_{v1} + (\delta t_{atm1} - \delta t_{atm2}) + \delta t_{atm1}\frac{\vec{K}(\vec{\omega}_2 - \vec{\omega}_1)}{c}. \tag{6.34}$$

6.2. VLBI Data Analysis

6.2.1. Partial Differentiation of the VLBI Delay

Partial differentiation of the VLBI time delay is procedure of VLBI data analysis as explained in Böhm et al. (2012); Teke (2011); Böhm et al. (2018). In order to derive equations simpler, a basic VLBI delay model

$$\tau = \vec{K} \cdot Q \cdot R \cdot W \cdot \vec{b} \tag{6.35}$$

is used . The source vector $\vec{K}$ is defined in BCRS, and baseline vector $\vec{b}$ is defined in TRF. This model does not contain gravitational delays, Lorentz transformation between GCRS and BCRS, and retarded baseline corrections. Polar motion components x_p and y_p are defined as the coordinate of the CIP in TRF along the Greenwich meridian and 270° east longitude respectively. The partial differentiation of the basic VLBI delay model w.r.t. x_p:

$$\frac{\partial \tau}{\partial x_p} = \vec{K} \cdot Q \cdot R \cdot \frac{\partial W}{\partial x_p} \cdot \vec{b}, \tag{6.36}$$

where

$$\frac{\partial W}{\partial x_p} = R_3(s') \cdot \begin{bmatrix} -\sin x_p & 0 & -\cos x_p \\ 0 & 0 & 0 \\ \cos x_p & 0 & -\sin x_p \end{bmatrix} \cdot R_1(y_p). \tag{6.37}$$

The partial differentiation of the delay model w.r.t. y_p:

$$\frac{\partial \tau}{\partial y_p} = \vec{K} \cdot Q \cdot R \cdot \frac{\partial W}{\partial y_p} \cdot \vec{b}, \tag{6.38}$$

where

$$\frac{\partial W}{\partial y_p} = R_3(s') \cdot R_2(x_p) \cdot \begin{bmatrix} 0 & 0 & 0 \\ 0 & -\sin y_p & \cos y_p \\ 0 & -\cos y_p & -\sin y_p \end{bmatrix}. \tag{6.39}$$

The partial differentiation of the delay model w.r.t. Earth rotation phase, UT1, is:

$$\frac{\partial \tau}{\partial (UT1)} = \vec{K} \cdot Q \cdot \frac{\partial R}{\partial (-\theta)} \cdot \frac{\partial (-\theta)}{\partial (UT1)} \cdot W \cdot \vec{b}, \tag{6.40}$$

where

$$\frac{\partial R}{\partial(-\theta)} = \begin{bmatrix} -\sin(-\theta) & cos(-\theta) & 0 \\ -\cos(-\theta) & -sin(-\theta) & 0 \\ 0 & 0 & 0 \end{bmatrix}, \tag{6.41}$$

and

$$\frac{\partial(-\theta)}{\partial(UT1)} = -ak = -1.00273781191135448. \tag{6.42}$$

The partial differentiation of the delay model w.r.t. the CIP coordinate X in CRF is:

$$\frac{\partial\tau}{\partial X} = \vec{K} \cdot \frac{\partial Q}{\partial X} \cdot R \cdot W \cdot \vec{b}, \tag{6.43}$$

where the nutation/precession matrix Q involving the motion of the celestial intermediate pole in CRS contains four matrices as given in Equation (6.15). Then, its partial differentiation w.r.t. the X as

$$\begin{aligned} \frac{\partial Q}{\partial X} &= \frac{\partial R_3(-E)}{\partial(-E)} \cdot \frac{\partial(-E)}{\partial X} \cdot R_2(-d) \cdot R_3(E) \cdot R_3(s) \\ &+ R_3(-E) \cdot \frac{\partial R_2(-d)}{\partial(-d)} \cdot \frac{\partial(-d)}{\partial X} \cdot R_3(E) \cdot R_3(s) \\ &+ R_3(-E) \cdot R_2(-d) \cdot \frac{\partial R_3(E)}{\partial E} \cdot \frac{\partial E}{\partial X} \cdot R_3(s) \\ &+ R_3(-E) \cdot R_2(-d) \cdot R_3(E) \cdot \frac{\partial R_3(s)}{\partial s} \cdot \frac{\partial s}{\partial X}. \end{aligned} \tag{6.44}$$

Equations (6.16, 6.17, and 6.18) are giving the formulae of E, d, and s. Then, their partial differentiations w.r.t. X are given as

$$\frac{\partial(-E)}{\partial X} = \frac{Y}{X^2 + Y^2}, \tag{6.45}$$

$$\frac{\partial(-d)}{\partial X} = \frac{X}{\sqrt{1 - (X^2 + Y^2)}\sqrt{X^2 + Y^2}}, \tag{6.46}$$

$$\frac{\partial s}{\partial X} = \frac{-Y}{2}. \tag{6.47}$$

The partial differentiation of the delay model w.r.t. the CIP coordinate Y in CRF is:

$$\frac{\partial\tau}{\partial Y} = \vec{K} \cdot \frac{\partial Q}{\partial Y} \cdot R \cdot W \cdot \vec{b}, \tag{6.48}$$

where

$$\frac{\partial Q}{\partial Y} = \frac{\partial R_3(-E)}{\partial(-E)} \cdot \frac{\partial(-E)}{\partial Y} \cdot R_2(-d) \cdot R_3(E) \cdot R_3(s)$$

$$+R_3(-E) \cdot \frac{\partial R_2(-d)}{\partial(-d)} \cdot \frac{\partial(-d)}{\partial Y} \cdot R_3(E) \cdot R_3(s)$$

$$+R_3(-E) \cdot R_2(-d) \cdot \frac{\partial R_3(E)}{\partial E} \cdot \frac{\partial E}{\partial Y} \cdot R_3(s)$$ (6.49)

$$+R_3(-E) \cdot R_2(-d) \cdot R_3(E) \cdot \frac{\partial R_3(s)}{\partial s} \cdot \frac{\partial s}{\partial Y}.$$

In Equation (6.49),

$$\frac{\partial(-E)}{\partial Y} = \frac{-X}{X^2 + Y^2},$$ (6.50)

$$\frac{\partial(-d)}{\partial Y} = \frac{Y}{\sqrt{1 - (X^2 + Y^2)}\sqrt{X^2 + Y^2}},$$ (6.51)

$$\frac{\partial s}{\partial Y} = \frac{-X}{2}.$$ (6.52)

The partial differentiation of the delay model w.r.t. α right ascension of the source

$$\frac{\partial \tau}{\partial \alpha} = \frac{\partial \vec{K}}{\partial \alpha} \cdot Q \cdot R \cdot W \cdot \vec{b},$$ (6.53)

where

$$\frac{\partial \vec{K}}{\partial \alpha} = \begin{bmatrix} -\cos\delta\sin\alpha & \cos\delta\cos\alpha & 0 \end{bmatrix}.$$ (6.54)

The partial differentiation of the delay model w.r.t. declination of the source

$$\frac{\partial \tau}{\partial \delta} = \frac{\partial \vec{K}}{\partial \delta} \cdot Q \cdot R \cdot W \cdot \vec{b},$$ (6.55)

where

$$\frac{\partial \vec{K}}{\partial \delta} = \begin{bmatrix} -\sin\delta\cos\alpha & -\sin\delta\sin\alpha & \cos\delta \end{bmatrix}.$$ (6.56)

The partial differentiation of the delay model w.r.t. the first antenna's X coordinate in TRF:

$$\frac{\partial \tau}{\partial X_{st1}} = \vec{K} \cdot Q \cdot R \cdot W \cdot \frac{\partial \vec{b}}{\partial X_{st1}},$$ (6.57)

where

$$\frac{\partial \vec{b}}{\partial X_{st1}} = \begin{bmatrix} 1 \\ 0 \\ 0 \end{bmatrix}.$$ (6.58)

6.2.2. PWLO Functions for Parameter Estimation in Sub-daily Periods

In VLBI analysis; troposphere gradients, troposphere delays, Earth orientation parameters, station and source coordinates, clocks, and others may be estimated as piecewise linear offset functions for sub-daily estimation intervals (Teke et al., 2009; Teke, 2011). Estimating offsets for UTC integer hours may be done from the initial offset and rates as piece-wise linear offset function

$$x_i = x_1 + \frac{t - t_1}{t_2 - t_1}(x_2 - x_1) \tag{6.59}$$

where x_1 and x_2 are estimated at defined t_1 and t_2 epochs respectively, and x_i is the estimate at the observation epoch t as illustrated in Figure 6.2. The partial differentiation of the delay
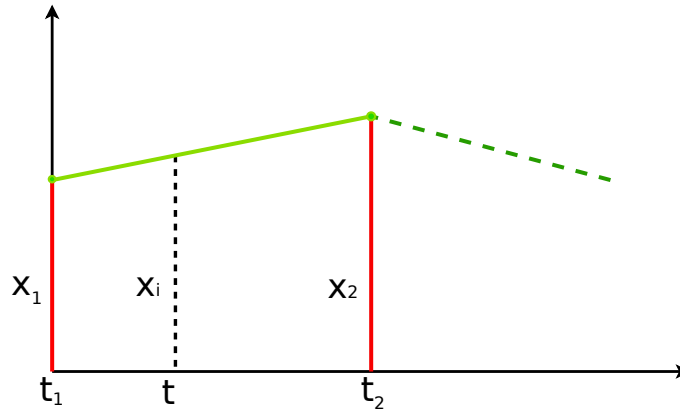
Figure 6.2: Piece-wise linear offset functions (Teke, 2011).

model with respect to an parameter to be estimated, x_i at the observation epoch t may be performed as

$$\frac{\partial \tau(t)}{\partial x_1} = \frac{\partial \tau(t)}{\partial x_i} \cdot \frac{\partial x_i}{\partial x_1}, \tag{6.60}$$

$$\frac{\partial \tau(t)}{\partial x_2} = \frac{\partial \tau(t)}{\partial x_i} \cdot \frac{\partial x_i}{\partial x_2}. \tag{6.61}$$

The partial differentiation of Equation (6.59) with respect to offsets x_1 and x_2 may be performed as

$$\frac{\partial x_i}{\partial x_1} = [1 - \frac{t - t_j}{t_{j+1} - t_j}], \tag{6.62}$$

$$\frac{\partial x_i}{\partial x_2} = [\frac{t - t_j}{t_{j+1} - t_j}]. \tag{6.63}$$

It should be noticed that the observation epoch t should be between the estimation epochs i.e. t_j and t_{j+1} for PWLO functions.

7. UT1 MONITORING WITH VLBI INTENSIVE SESSIONS

UT1 is one of the five EOP which are used for transformation between CRF and TRF (see Chapter 2). Accurate determination of the EOP is necessary for navigation purposes both in space and on the Earth. The main and only technique for UT1 determination is VLBI. The main objective of this chapter is to improve the VLBI estimation accuracy of UT1 using several approaches. For this purpose,the series of New UT1 parameter, with an improved accuracy relative to those produced by the IVS Intensive standard analysis, was estimated by means of assimilating the troposphere zenith delays, and troposphere gradients from GNSS in the analysis of Intensive sessions (Intensives).

7.1. GNSS Troposphere Delays and Gradients

The IGS, (Dow, Neilan and Rizos, 2009) is providing GNSS derived troposphere delays from 01.01.2008 till now with three weeks latency from IGS FTP archives (e.g. CDDIS: Greenbelt USA). In the content of this thesis, troposphere products of stations at Table (7.1) are downloaded with Linux shell scripts automatically every day. Then, these troposphere related files are converted into a suitable format that the VLBI analysis software can read. VLBI Intensives and the stations joining these sessions are given below.

- INT1 sessions: Wettzell (Germany)-Kokee Park (Hawaii Island, USA)

- INT2 sessions: Wettzell (Germany)-Tsukuba or Ishioka (Japan)

- INT3 sessions: Wettzell (Germany)-Ny Alesund (Norway)-Tsukuba or Ishioka (Japan)

IGS troposphere zenith signal delays and gradients have been determined as 5-min intervals from the analysis of the observations of more than 350 GNSS stations around the world with PPP technique (Zumberge et al., 1997) using Bernese software (Dach et al., 2015) by the GNSS analysis centre, United States Naval Observatory (USNO) every day from July of 2011. In this analysis, Earth orientation parameters, satellite orbits, clock corrections of satellite and receiver are fixed to IGS final combined values (IGS, 2019b). ZHD are calculated with hydrostatic NMF (Niell, 1996), and reduced from the observations. ZWD are estimated using the GMF (Böhm et al., 2006). The observations are restricted to those observed with an elevation angle greater than $7°$ (Byram, Hackman and Tracey, 2011). Between January of 2008 and July of 2011, these troposphere products were produced using Gipsy-

Table 7.1: Geodetic co-located sites of VLBI and GNSS stations, and their ITRF2008 ellipsoidal heights, horizontal distances and height differences.

Co-located site	Latitude (°)	Country	VLBI antenna height (m)	GNSS station name	VLBI-GNSS horizontal dist. (m)	GNSS antenna height (m)	VLBI-GNSS height diff. (m)
Ny-Alesund	78.9	Norway	87.3	nya1	106	84.2	3.1
				nyal	112	83.7	3.6
Wettzell	49.1	Germany	669.1	wtzr	139	666.1	3.0
				wtza	137	666.0	3.1
Tsukuba	36.1	Japan	84.7	tskb	302	67.3	17.4
Kokee	22.1	USA	1176.6	kokb	45	1167.4	9.2

Oasis GNSS Software (Webb and Zumberge, 1995) with a similar analysis parameterization and strategy by NASA Jet Propulsion Laboratory (JPL) (Byun and Bar-Sever, 2009).

The same troposphere signal delays as produced by USNO were generated from the GNSS PPP observation model using Bernese GNSS Software (Dach et al., 2015) for only GNSS sites co-located with VLBI stations, in the scope of this thesis independent to IGS. The GNSS observations were re-weighted according to elevation angle towards satellites for troposphere estimation using PPP method. Station coordinates were acquired from ITRF2014 coordinates and ITRF2014 velocity corrections for observation epochs. Clock corrections for satellites and receivers were reduced from observations using final solutions of CODE analysis center. Satellite coordinates were fixed to the interpolated values to each observation epoch of precise ephemeris coordinates of CODE analysis center. EOP were fixed to final products of CODE in accordance with IAU2000/2006 precession-nutation model. Displacements of stations coordinates due to ocean tidal loading were corrected using the FES2004 model (Lyard et al., 2006). Besides, displacements owing to atmosphere tidal loading effect were calculated using Ray and Ponte (2003) model, and a priori reduced from station coordinates. Troposphere mapping function was VMF1 (Böhm, Werl and Schuh, 2006). In station-specific troposphere estimation parametrization, troposphere delays were estimated using VMF1 for 15 minutes intervals with 10 centimeter after 15 minutes, using relative loose constraints. In addition to this, the estimation of troposphere gradients was carried out using Chen and Herring (1997) gradient model for 30 minutes intervals with 1 centimeter after 30 minutes, with loose relative constraints. Consequently, troposphere signal delays were obtained as SINEX files.

Figure 7.1: VLBI stations participating in IVS-R1 and -R4 sessions (black squares) as well as Intensives (red dots). INT1, INT2, and INT3 baseline vectors are given with purple, blue (dashed) and red lines, respectively.

7.2. IVS Intensive and Standard Sessions

IVS is responsible for organizing the VLBI observations. Intensives (INT1, INT2, and INT3) are carried out for 1-2 hours in order for UT1 determination on a daily basis owing to regularly UT1 determination for each day. UT1 obtained by IVS analysis centers from the analysis of the Intensives is the necessary parameter used for space-based navigation and orbit determination studies, and continuously presented to the Earth and space science users by the IERS for free of charge. In contrast to "Standard sessions" performed for 24-hours with in general more than six VLBI antennas, "Intensives" are executed using 2-3 stations for 1-2 hours duration due to financial and operational difficulties. INT1 sessions are realized for weekdays between 18:30-19:30 UT with radio telescopes at Wettzell (Germany) and Kokee Park (Hawaii islands, USA) since 1984. In addition to this, INT2 sessions take up 1-2 hours long measurement at 7:30 UT on Saturdays and Sundays with Tsukuba or Ishioka (Japan) and Wettzell (Germany) baseline since 2002. Besides, on Mondays, INT3 sessions are held with the participation of Tsukuba or Ishioka (Japan), Wettzell (Germany) and Ny-Alesund (Norway) radio telescopes. On the other hand, 24-hours long Standard sessions so-called "Rapid turnaround" are operated for Mondays (R1) and Thursdays (R4) for Earth orienta-

69

tion parameters (EOP) monitoring. Figure (7.1) shows that the VLBI stations observing for "Intensive" and "Standard sessions".

So as to enhance the precision of the VLBI measurements of Intensives to the UT1 parameter, the long baseline vectors connecting the radio telescopes are selected close to the equatorial plane and east-west extension (Nothnagel and Schnell, 2008; Nilsson, Böhm and Schuh, 2011). The baseline lengths of Intensives satisfying the UT1 determination requirements are 8445 km and 10357 km for Wettzell-Tsukuba and Wettzell-Kokee baselines, respectively. After the correlation of observations, Intensives are published in 1 week at the latest via FTP servers of IVS analysis centers (Schuh and Behrend, 2012).

7.3. Analysis of the VLBI Intensive Sessions

Both the Intensive and Standard sessions were analyzed with VieVS VLBI and satellite software (Böhm et al., 2018) developed by the Vienna Institute of Technology. Analysis of the VLBI observations with several analysis strategies was carried out between 2008 and 2018. Firstly, IVS standard analysis of the Intensives (Analysis-1) were performed. In the context of the Analysis-1, for 1-hour VLBI session with two radio telescope, a troposphere signal delay per station (two parameters), clock synchronization corrections between atomic clocks of VLBI stations as one offset and one linear trend (two parameters), and UT1 offset (one parameter) are estimated. Apart from these parameters, coordinates of radio telescopes in TRF needed for analysis of observations, CRF coordinates of Quasars, polar motion coordinates and nutation offsets are fixed to their a priori values. The errors between the exact and a priori values of these parameters are propagated into UT1 parameters according to their correlations with UT1. The received signal in S (2.15-2.35 GHz) and X (8.0-8.8 GHz) bands by VLBI antennas are delayed by the ionosphere. VLBI correlators establish the ionosphere delay as a linear combination of VLBI signal delays in S and X bands. The observation files contain ionosphere delays through the signal paths for every observation. As a result of this, ionosphere signal delays were not modeled in the analysis, instead, they were reduced from observations before the parameter estimation. Analysis-1 has the same analysis strategy and parameterization as the standard analysis of IVS. UT1 values obtained from Analysis-1 is so-called "StandardUT1(A1)". In the context of this thesis, two new analysis method: "Analysis-2" and "Analysis-3" are performed and suggested to use in addition to the Analysis-1.

Analysis-2 was carried out via reducing the external GNSS troposphere gradients from VLBI observations a priori to the estimation. Troposphere ZWD estimation was also included in Analysis-2 as one ZWD per VLBI antenna. Troposphere ZHD were calculated from Equa-

tion (4.23) (Saastamoinen, 1972) using in-situ total pressures and ellipsoidal latitudes of stations, then reduced from observations before parameter estimation. In order to subtract troposphere north and east gradients from VLBI measurements, gradients acquired from GNSS observations were interpolated (linearly) to the VLBI observations epochs, and azimuthal asymmetric troposphere delays were calculated using Davis et al. (1985, 1993) azimuthal asymmetric troposphere delay model and Chen and Herring (1997) troposphere gradient mapping function as given in Equations (4.32), (4.34). Here, we used IGS (IGS, 2019b) 5-min interval troposphere north and east gradients. To summarize, in Analysis-2: In addition to Analysis-1 which estimates a troposphere zenith wet delay per VLBI antenna, north and east troposphere gradients derived from GNSS were pre-reduced from VLBI observations. The estimated UT1 with Analysis-2 is called as NewUT1(A2).

Analysis-3 is another approach as an alternative to Analysis-1 and Analysis-2. In this perspective, after the GNSS troposphere gradients are reduced from the VLBI observations, corrections to a priori gradients are estimated in the analysis of the Intensives. In other words, we estimated troposphere east-west, G_e, and north-south, G_n gradients as corrections to those a priori gradients for each station of the Intensives. It is anticipated that azimuthal asymmetric troposphere delays are reduced from the observations pretty well with Analysis-3. NewUT1(A3) is obtained with Analysis-3. In the Analysis-2 and Analysis-3, the troposphere gradients estimated from observations of International GNSS Service (IGS, Dow, Neilan and Rizos 2009) stations which are given in Table (7.1) co-located with VLBI stations were used.

StandardUT1(A1), NewUT1(A2), and NewUT1(A3) achieved from the analysis of the Intensives with Analysis-1, Analysis-2, and Analysis-3, respectively should be compared to reference UT1 values so as to find out the accuracy of analysis methods. UT1 reference series should be more accurate than those obtained from Intensives. UT1 determination from 24-hours R1 and R4 sessions is much more accurate than Intensives derived from IVS standard analysis. While the accuracy of UT1 estimation from R1 and R4 sessions are $\sim 1-2\mu s$, it becomes $\sim 15 - 20\mu s$ for Intensives (Schuh and Behrend, 2012). Hence, UT1 reference values were obtained from R1 and R4 observations for investigation of the accuracy of UT1 determination from Intensives with Analysis-1, Analysis-2, and Analysis-3.

The reference UT1 series is estimated using piecewise linear offset functions (Teke et al., 2009) without any absolute or relative constraint. Nutation offsets are fixed to IAU2006 precession-nutation model (Petit and Luzum, 2010) plus IERS 14 C04 Earth orientation parameters (EOP) series (Bizouard et al., 2018) corrections. Polar motion coordinates (x_p, y_p) were estimated as one offset per session while their a priori values are IERS 14 C04 series plus high-frequency (diurnal and semi-diurnal) polar motion variations (Petit and Luzum,

2010). Hourly estimates of UT1 were performed using piecewise linear offsets with a priori values: IERS 14 C04 series plus high-frequency UT1 variations (Petit and Luzum, 2010). Daily corrections to the ITRF2014 (Altamimi et al., 2016) coordinates of Earth-fixed stations, and ICRF2 (Fey, Gordon and Jacobs, 2009) coordinates of space-fixed quasars were estimated through imposing datum conditions: NNT/NNR for TRF and NNR for CRF. Displacements of crust-fixed stations were calculated with models: Solid Earth tides (Petit and Luzum, 2010), ocean tidal loading (Lyard et al., 2006), pole tides (Petit and Luzum, 2010), atmosphere loading (Petrov and Boy, 2004) besides TRF coordinate linear velocity corrections due to plate tectonics per observation epoch. Troposphere ZWD were estimated hourly. Troposphere gradients were estimated as 6-hourly piecewise linear offsets using Davis et al. (1985, 1993) troposphere model. In the troposphere model, VMF1 (Vienna Mapping Function, Böhm, Werl and Schuh 2006) was used for azimuthal symmetric delays, and Chen and Herring (1997) gradient mapping function was used for azimuthal asymmetric delays. Ionosphere delays determined during correlation of VLBI observations were reduced from signal delays of each observation before parameter estimation. Clock errors at VLBI telescopes were estimated as coefficients of quadratic polynomials, and reduced from observations before the adjustment.

7.4. Comparisons of Universal Time Estimates from Intensive Sessions

UT1 estimates from Intensives (INT1, INT2, and INT3) were compared to those obtained from the analysis of R1 and R4 (reference UT1 series) from the beginning of 2008 till July of 2018. We eliminated estimates of StandardUT1(A1) series with formal uncertainties greater than $50\ \mu s$. Estimations corresponding to the estimation epoch that we eliminated for StandardUT1(A1) were also removed from the NewUT1(A2), and NewUT1(A3) series. Thus, StandardUT1(A1), NewUT1(A2), and NewUT1(A3) series were obtained in 3030 epochs as plotted in Figure (7.2).
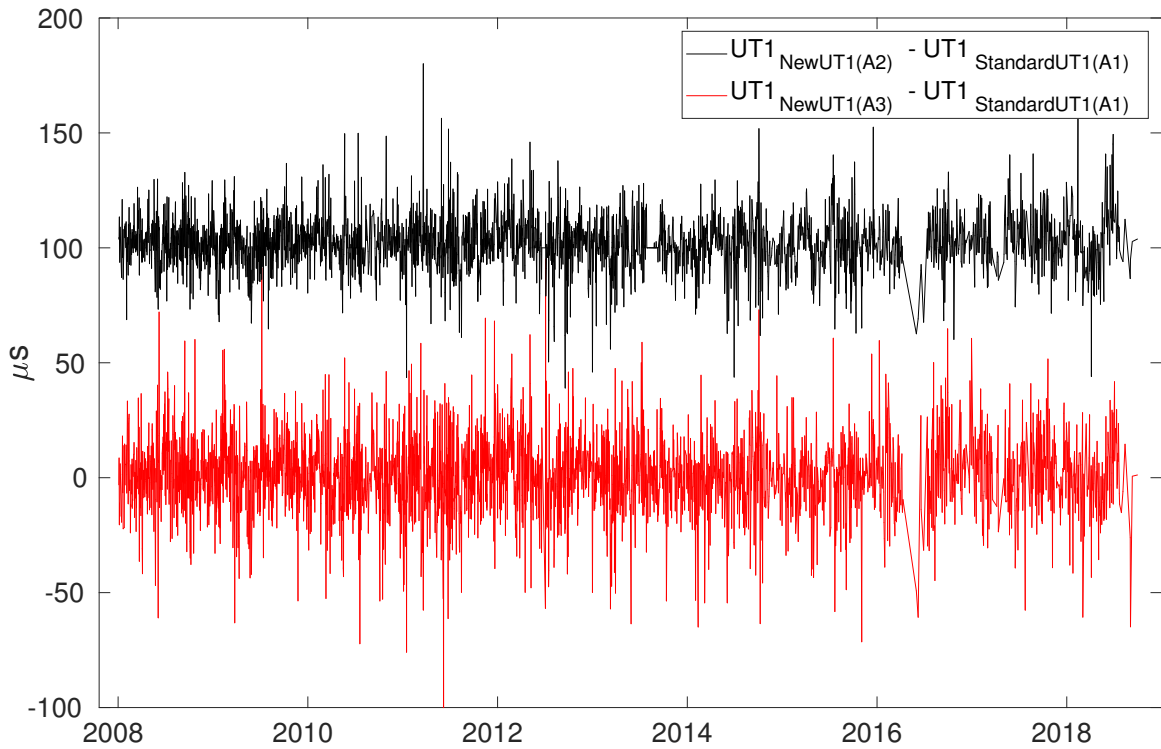
Figure 7.2: Time series of NewUT1(A2) and NewUT1(A3) estimated from in order of Analysis-2 and Analysis-3 with respect to IVS standard analysis: StandardUT1(A1). The analyzed sessions are INT1, INT2, and INT3.

To investigate the impact on the UT1 estimation accuracy of the new analysis strategies proposed in this thesis (Analysis-2 and Analysis-3) compared to the IVS standard analysis (Analysis-1), differences of NewUT1(A2) and NewUT1(A3) obtained from the analysis of INT1 session carried out on weekdays from the StandardUT1(A1) were acquired.

Weighted mean (WM_j^k) as well as weighted root-mean-square error ($WRMS_j^k$) of difference vector between $k^t h$ and $j^t h$ series were calculated from Equations (7.1), (7.2) given below,

$$WM_j^k = \frac{\sum_{i=1}^n \dfrac{UT1_{Analysis-j,i} - UT1_{Analysis-k,i}}{\sigma^2_{UT1_{Analysis-j,i}} + \sigma^2_{UT1_{Analysis-k,i}}}}{\sum_{i=1}^n \dfrac{1}{\sigma^2_{UT1_{Analysis-j,i}} + \sigma^2_{UT1_{Analysis-k,i}}}} \tag{7.1}$$

and

$$WRMS_j^k = \sqrt{\frac{\sum_{i=1}^n \dfrac{(UT1_{Analysis-j,i} - UT1_{Analysis-k,i} - WM_j^k)^2}{\sigma^2_{UT1_{Analysis-j,i}} + \sigma^2_{UT1_{Analysis-k,i}}}}{\sum_{i=1}^n \dfrac{1}{\sigma^2_{UT1_{Analysis-j,i}} + \sigma^2_{UT1_{Analysis-k,i}}}}} \tag{7.2}$$

where n is the number of estimation in series, $UT1_{Analysis-j,i}$ is the estimated UT1 represented with indices i. As previously stated, Analysis-1, Analysis-2, and Analysis-3 denote StandartUT1(A1), NewUT1(A2), and NewUT1(A3), respectively. $\sigma_{UT1_{Analysis-j,i}}$ is the formal uncertainties of $UT1_{Analysis-j,i}$. These WM and $WRMS$ values of difference vector between NewUT1 series and StandartUT1 are given in Table (7.2).

Table 7.2: WRMS of differences of UT1 estimates from INT1, INT2 and INT3 sessions. Median of formal uncertainties of UT1 estimates are given in square brackets (such as [NewUT1(A2) — StandardUT1(A1)]).

Analysis (3030 UT1 pairs)	WRMS of UT1 differences in μs
NewUT1(A2)-StandardUT1(A1)	$\pm$11.7 [10.6 | 10.7]
NewUT1(A3)-StandardUT1(A1)	$\pm$17.3 [16.5 | 10.7]

WRMS values given in table show that NewUT1(A2) is more close to the IVS standard solution (StandardUT1(A1)) than NewUT1(A3). Comparing the UT1 estimates of Intensives do not indicate whether the accuracy of UT1 estimates is increasing or not. However, that shows meaningful changes in UT1 estimates from Intensives via various analysis strategies. As previously mentioned in the context of this thesis, hourly UT1 piece-wise linear offsets were estimated from 24-hours long R1 and R4 sessions. Besides, one UT1 offset at the midpoint of session duration was estimated from Intensives for each of 1-hour long observations. While UT1 estimates of R1 and R4 sessions were being interpolated to UT1 estimation epochs of Intensives, UT1-TAI values were used via reducing leap seconds ($UTC - TAI = -37s$ since 01.01.2017) from UT1 estimates in order to prevent a large gap ($1s$) as shown in Figure (7.3).

In our comparisons, UT1 estimates of R1 and R4 sessions were linearly interpolated to UT1
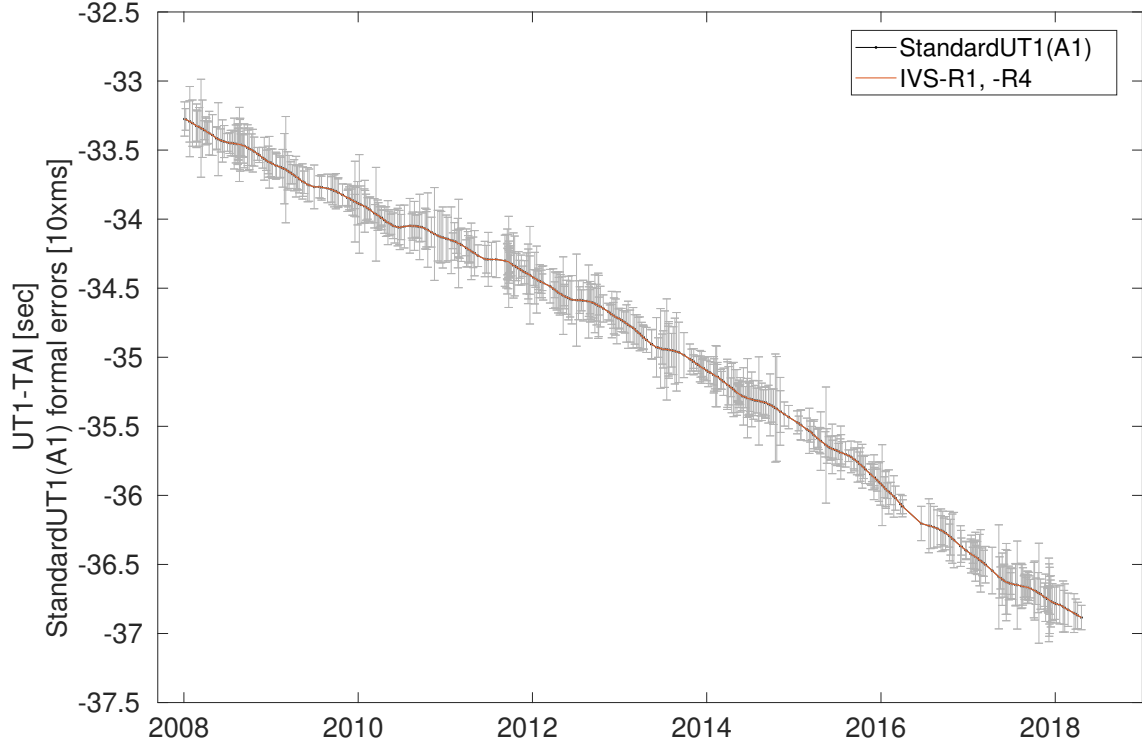
Figure 7.3: UT1 estimates of R1, R4 Standard sessions and INT1, INT2, INT3 Intensives from the beginning of 2008 till July of 2018. Formal errors of StandardUT1(A1) is in $10 \times ms$ to be seen better.

estimation epochs of Intensives, if only the time interval between epochs of UT1 estimates of Standard and Intensives is less than 1 hour. Thence, the differences between UT1 estimates of Intensive and Standard session were obtained as seen in Figure (7.4). UT1 estimates of Intensive and Standard sessions with formal uncertainties less than $50\mu s$ and $20\mu s$ respectively were considered for comparison (total 548 UT1 differences) as given in Figure (7.4) and Table (7.3).

The derivation of UT1 with respect to time so-called Length-of-Day (LOD) is more accurately determined by GNSS compared to VLBI (Rothacher et al., 1999; Steigenberger et al., 2006; Dow, Neilan and Rizos, 2009). GNSS LOD estimates at 12 UT were achieved in daily resolution between the beginning of 2008 to July of 2018 from the IGS analysis centers such as ESA/ESOC, Germany; NASA/JPL, the USA; NOAA/NGS. LOD values were calculated from UT1 estimates of all Intensives (INT1, INT2, INT3) using following formulae

$$
\begin{aligned}
LOD(t) &= \frac{UT1(t_1) - UT1(t_2)}{t_2 - t_1} \times 1 day \\
t &= \frac{t_1 + t_2}{2} \quad (t_2 - t_1 < 1.2 day)
\end{aligned}
\tag{7.3}
$$
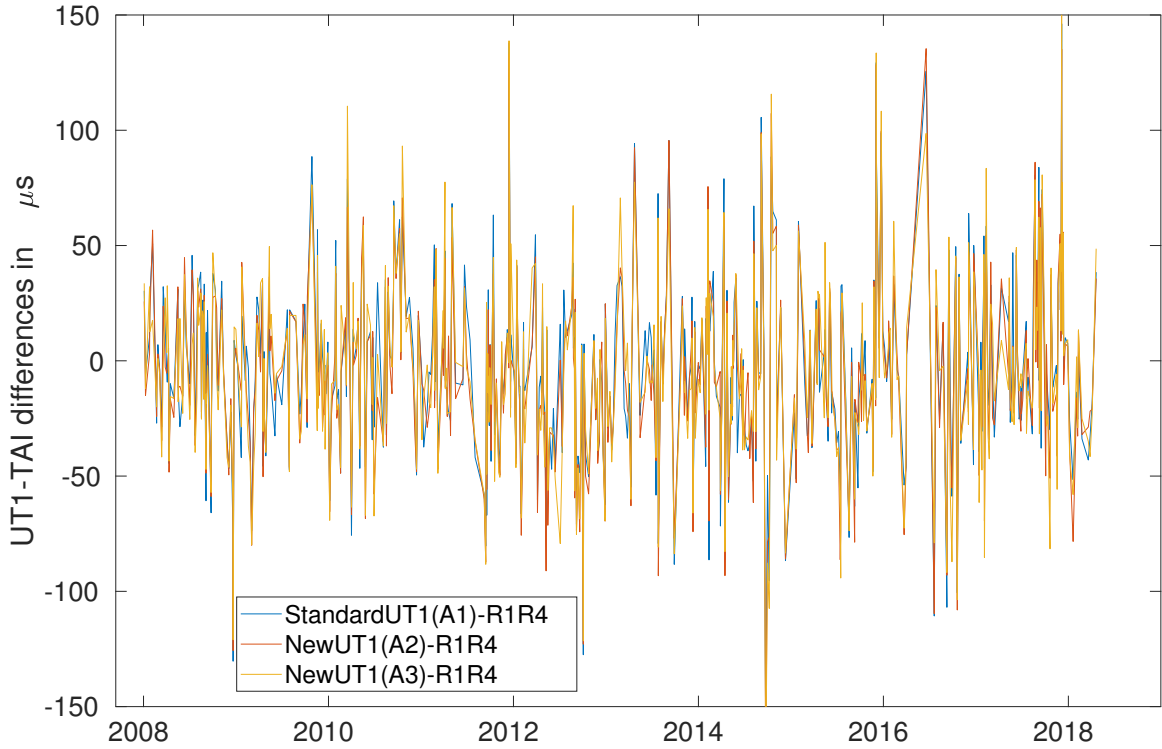
Figure 7.4: UT1 estimates from the analysis of INT1 sessions with respect to estimates of R1, R4 sessions.

where t_1 and t_2 are UT1 estimation epochs of sequenced Intensives and t denotes epoch of LOD which is the midpoint of t_1 and t_2. In order to calculate LOD, UT1 estimates were used if their formal uncertainties are less than $50 \mu s$, and the difference between adjacent epochs is less than $1.2 \ days$. Differentiation with respect to time is a linear approach. Then, if UT1 values with consecutive estimation epochs with much more than the 1-day time interval between them are used, LOD values would not straightly be determined accurately. That is the reason for the maximum allowed time interval between adjacent epochs is less than $1.2 \ days$. Daily LOD estimates of IGS analysis centers at 12 UT were linearly interpolated to the estimation epochs of LOD obtained from the analysis of Intensives, and differences of these series were achieved such as $LOD_{Standard(A1)} - LOD_{IGS(ESA)}$ or $LOD_{NewUT1(A2)} -$

Table 7.3: WRMS of differences of UT1 estimates from INT1 sessions and from R1 and R4 sessions.

Analysis	WRMS of UT1 differences in μs INT1 Sessions (548 UT1 pairs)
StandardUT1(A1)-R1R4	± 38.0
NewUT1(A2)-R1R4	± 37.7
NewUT1(A3)-R1R4	± 38.8
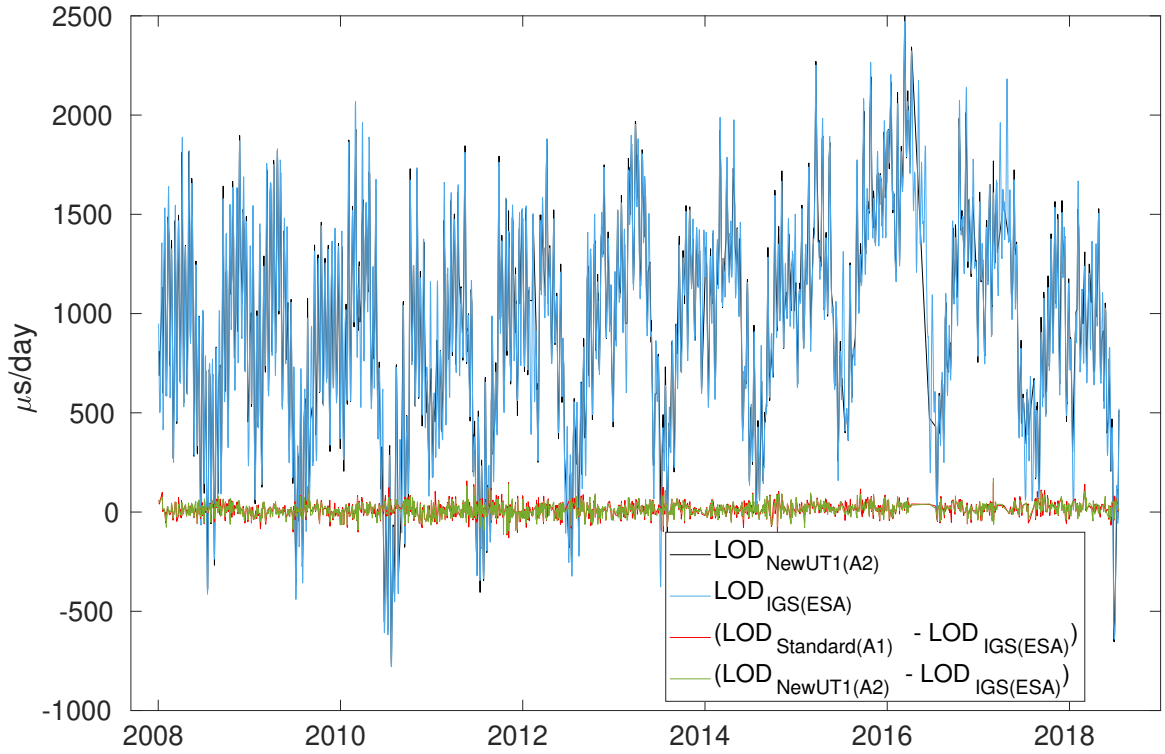
Figure 7.5: Length-of-Day (LOD) estimated from Intensives and ESA/ESOC IGS analysis center, and their differences from the beginning of 2008 till July of 2018.

$LOD_{IGS(ESA)}$. Agreement between GNSS and VLBI estimated LOD series were presented with WRMS of differences as given in Table (7.4).

Table 7.4: WRMS of differences of LOD estimates of analysis centers (ESA(ESOC), NASA(JPL) and NOAA(NGS)) and INT1 sessions in $\mu s/day$. Analysis-1, Analysis-2 and Analysis-3 series are in the same epochs (1610 values considered).

	StandardUT1(A1)	NewUT1(A2)	NewUT1(A3)
ESA/ESSOC	$\pm$ 34.2	$\pm$ 31.6	$\pm$ 33.7
NASA/JPL	$\pm$ 36.9	$\pm$ 34.1	$\pm$ 36.2
NOAA/NGS	$\pm$ 37.6	$\pm$ 35.6	$\pm$ 36.6

WRMS of differences between LOD series calculated from NewUT1(A2) estimates and LOD series of IGS analysis centers (ESA/ESOC, NASA/JPL, and NOAA/NGS) are $2 - 3\mu s/day$ less than those of StandardUT1(A1). Besides, Analysis-3 is also $1\mu s/day$ compared to the IVS standard solution (Table 7.4).

While formal uncertainties of LOD estimation of one offset from 24-hours long R1 and R4 observations are about $15\mu s/day$, IGS stations covering the world with more than 400 stations can determine LOD with formal uncertainties $10\mu s/day$ (Rothacher et al., 1999; Steigenberger et al., 2006; Nilsson, Böhm and Schuh, 2011). Considering these, LOD series from NewUT1(A2) obtained from Analysis-2 is more accurate $(2 - 3\mu s/day)$ than IVS standard analysis. In other words, introducing GNSS derived troposphere east and north gradients into the analysis of the Intensives is increasing the accuracy about $(2 - 3\mu s/day)$ over 10-years UT1 series. Analysis-3 also increases the accuracy of $(1\mu s/day)$.

The daily updated Universal Time (UT1) series have been produced automatically in the content of this thesis is available online: `http://vlbi.hacettepe.edu.tr/en/menu/tubitak_3501_115y244-20`

8. SUB-DAILY ERP ESTIMATION FROM VLBI OBSERVATIONS

The IERS2010 conventions (Petit and Luzum, 2010) suggested to use the model of high-frequency harmonic variations of Earth rotation parameters (ERP) caused by ocean tides (see Chapter 2). This model was generated by Ray et al. (1994) more than twenty-five years ago based on ocean dynamics when the observations of the space geodetic techniques were not enough to estimate such a model. International Association of Geodesy (IAG) propounded that this model should be updated with the new amplitudes. This chapter aims to estimate a better model for sub-daily ERP variations due to ocean tides as a replacement of the IERS recommended model.

8.1. Analysis Parametrization

IVS (Schlüter and Behrend, 2007; Schuh and Behrend, 2009) is responsible for scheduling and carrying out VLBI sessions. Observing program consists of so-called "master" for $24 - hours$ (standard) and $\sim 1 - hour$ (intensive) sessions. Among all sessions the *Standard* sessions are considered for this part of the thesis due to the fact that *Intensive* sessions are carried out with 2 or 3 radio telescopes that can record 15-55 epochs. Since, estimation of polar motion coordinates requires globally distributed observing network, only $24 - hours$ sessions (e.g. R1, R4, CONT; see up-to-date observing program: IVS 2019) with minimum 6 VLBI stations between 2000-2018 years were analyzed (see Table 8.1). Figure (8.1) shows the stations that participated many sessions and meet our selection criteria. CONT observations are performed per $3 - years$ intervals for $15 - days$ continuously with the contribution of $10 \sim 17$ stations in order to test the maximum capability of the modern VLBI technique. Due to operational restrictions, continuous VLBI observations are not feasible for every day and by every VLBI station in contrast to GNSS. Instead, IVS-R1 and IVS-R4 sessions so-called rapid turnaround are conducted twice per week, i.e. on Monday and Thursday, respectively (Lambert and Gontier, 2006). Some of the other sessions are either executed in regional networks or planned for testing purposes such as the deployment of new devices or techniques.

In this part of the thesis, the Earth rotation parameters x_p, y_p and $\Delta UT1$ from VLBI observations are estimated using VieVS (Böhm et al., 2018) which utilizes classical Gauss-Markov least squares method. In the first run, we found and eliminated sessions that are not suitable for ERP estimation with criterion $chi^2 > 4$ and $wrms > 2$ (weighted root-mean-square error). Moreover, we applied a "normal outlier test" with the threshold value of $3 \cdot m_0 \cdot \sqrt{Q_{vv}}$
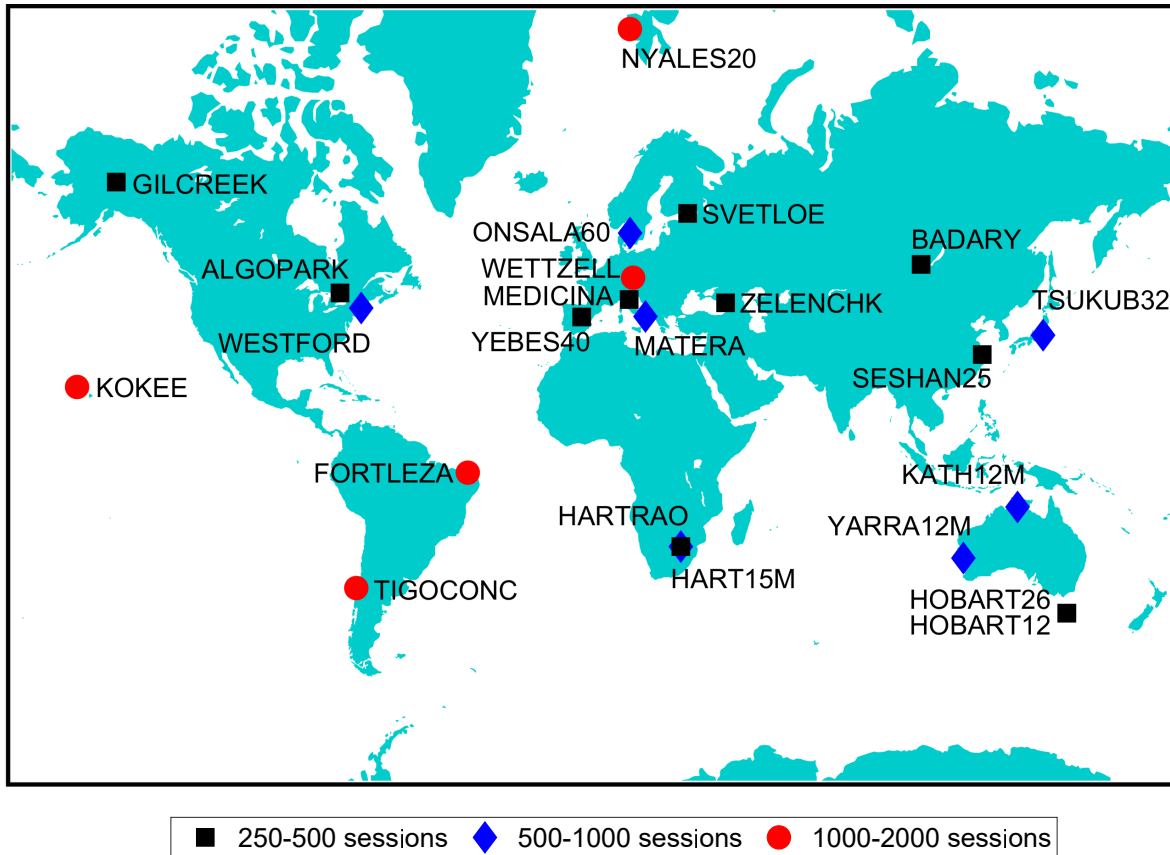
Figure 8.1: VLBI stations participating to 24-hours sessions between 2000-2018.

in VieVS for remaining 2171 sessions. Here, $\sqrt{Q_{vv}}$ denotes the co-factor matrix of post-fit observational residuals ($Q_{vv} = Q_{ll} - A\,Q_{xx}\,A^T$). The remaining observations of which post-fit corrections are smaller than three times of their standard errors ($|v| = 3m_v$).

We analyzed every session separately, then we obtained ERP estimates for 1-hour intervals as piecewise linear offsets (Teke et al., 2009). Estimation of polar motion with nutation in sub-daily periods is not possible due to their high correlations in sub-daily revolution (Thaller et al., 2007). In order to overcome this problem, Artz et al. (2010) recommended using accurately estimated nutation offsets as a priori values and fixing nutation during sub-daily polar motion estimation. For this reason, we fixed values of nutation offsets to International Astronomical Union (IAU) 2006 precession-nutation model (Petit and Luzum, 2010) plus IERS 14 C04 series (Bizouard et al., 2018) corrections.

All participating stations to the sessions have atomic clocks that are labeling time instant to the received signals. The clock of one station (reference station) is assumed to be correct in the analysis. Synchronization errors between the clock of reference station and others were estimated within pre-adjustment as coefficients of quadratic polynomials for 60-min intervals, and then reduced from observations. We used Davis et al. (1985, 1993) model, which

is widely used for all space and satellite-based geodetic techniques, for modeling the troposphere delay. Based on in-situ total surface pressure sensors and station latitude, hydrostatic delays along the zenith path were calculated (Saastamoinen, 1973) and reduced from observations after mapping with VMF3. To deal with the zenith wet delays, the design matrix formed with wet troposphere mapping functions as the partials was used for the estimation of ZWD as 60-min intervals. VMF3, Landskron and Böhm 2018 was preferred for mapping the troposphere delay in zenith to the observation direction. North and east troposphere gradients were estimated for 6-hour intervals.

A priori TRF catalog containing station coordinates and velocities was chosen as ITRF14 (Altamimi et al., 2016). We imposed NNT and NNR condition equations for the estimation of station daily coordinates so that translations and rotations between the estimated and the a priori TRF are derived as zero. The a priori quasar coordinates were fixed to ICRF2 (Fey, Gordon and Jacobs, 2009). Displacement of crust-fixed points due to geodynamical effects were reduced from antenna coordinates before adjustment according to the models counseled in the IERS2010 conventions (Petit and Luzum, 2010) (see Section 5.4.7). These displacements are caused by solid Earth tides (Petit and Luzum, 2010), ocean tidal loading (Lyard et al., 2006), atmosphere pressure loading (Petrov and Boy, 2004), and pole tides (Petit and Luzum, 2010) (see Section 5.4.7).

In this study, the IERS2010 model was not applied a priori because we want to see this effect on ERP. ERP were hourly estimated without introducing any condition or constraint equations. After we got hourly ERP offset estimates for each day separately, sessions were put together chronologically. First and last estimates of sessions have large formal errors that means they are inaccurate estimates due to lack of observation within the estimation interval. Then, we removed first and last estimates of all sessions. The last outlier removal procedure at estimated parameter level was fulfilled via removing all ERP hourly estimates having formal errors greater than three times of median of formal errors of all estimates. An overview on the ERP time series as obtained with the procedure mentioned above is summarized in Table (8.1). Then, the ERP time series decomposed into tidal constituents as proposed in the IERS2010 model via utilizing the following sinusoidal amplitude estimation methods: least squares, singular value decomposition and complex demodulation (see Chapter 3).

Table 8.1: ERP estimation overview.

Duration of session	24-hours
Time period	05.01.2000 - 04.08.2018
Minimum stations per session	6
Number of sessions	2171

Table 8.2: Observation periods of latest four IVS-CONT campaigns.

Campaign name	First observation (00:00:00 UTC)	Last observation (23:59:59 UTC)	Number of stations participated
CONT08	AUG 12, 2008	AUG 26, 2008	10
CONT11	SEP 15, 2011	SEP 29, 2011	14
CONT14	MAY 6, 2014	MAY 20, 2014	17
CONT17	NOV 28, 2017	DEC 12, 2017	14 (per legacies)

Numbers of estimation epochs	x_p : 37 697, y_p : 37 697, ΔUT1: 43 891
Medians of formal errors	x_p : 234.2 (μas), y_p : 258.8 (μas), ΔUT1: 14.3 (μs)

8.2. Results of VLBI Analysis

Analysis of VLBI observations was carried out for $24 - hour$ (Standard) sessions from the beginning of 2000 to the end of 2018. This time interval covers IVS-CONT campaigns (see Table 8.2 for most recent ones) held for $15 - days$ continuously observing with $10 \sim 17$ VLBI stations alongside IVS-R1 and -R4 sessions performed with at least 6 stations on Mondays and Thursdays. ERP estimation intervals were adjusted to $1 - hour$ due to the fact that sub-daily tidal constituent amplitude estimation requires many sub-daily estimations. But, decreasing $1 - hour$ to shorter intervals is decreasing x_p, y_p, and $\Delta UT1$ estimation accuracy since some of the VLBI stations may be out-of-service that distort network geometry for a certain period of time. Estimation accuracy of x_p and y_p increase with the expansion of the volume of global polyhedron built by VLBI stations. In addition to this, the equatorial projection of baselines is directly proportional to $\Delta UT1$ determination accuracy. Sessions analyzed satisfy these criteria mostly. Medians of formal errors for x_p, y_p and $\Delta UT1$ estimates are found as $234.2 \ \mu as$, $258.8 \ \mu as$, and $14.3 \ \mu s$, respectively. This may indicate that $\Delta UT1$ determination accuracy of the VLBI technique is more than those for x_p and y_p (e.g. $258.8 \mu as > 234.2 \mu as > 14.3 \mu s \times 15 = 214.5 \mu as$). Outlier detection and removal at the observation and at the parameter level (post-analysis) was carried out. By this approach, we basically aimed to unveil geophysical signals by means of removing unwanted noises. Thus, our ERP estimates are dedicated to be convenient to estimate the amplitudes of sub-daily ERP variations caused by the ocean tides.

A statistical comparison of the hourly ERP series between the model and VLBI observations during IVS-CONT campaigns is shown in Table (8.3). The plots of concerning time series

and Fourier transform of these series are shown in Figure (8.3) and (8.4) respectively. Even if the IERS model is not up-to-date, it demonstrates the average impact of ocean tides on ERP variations. Because, every abrupt change in ERP estimates with respect to the IERS2010 model may not be geophysically meaningful signals. We examined the Fourier transform plots that show the IERS2010 model and estimated ERP series that are mostly well-matched during CONT11. The Fourier plots are good metrics for investigation of the amplitudes of tidal constituents in frequency domain. The Fourier transform of polar motion coordinates $(x_p - iy_p)$ shows prograde and retrograde parts at positive and negative periods, respectively. Prograde parts of these plots have a good agreement with the IERS model. By contrast, estimated retrograde polar motions have deviated about $50 - 150 \ \mu as$ from the IERS2010 model for periods between -16 and $-24 - hours$. The IERS2010 conventions (Petit and Luzum, 2010) stated that motions having periods between -16 and $-48 - hours$ should be incorporated in nutation. Actually, Fourier plot of polar motion coordinates should not consist peaks at diurnal retrograde periods if the a priori nutation offsets are fixed to well-estimated values as recommended by Artz et al. (2010). Thence, we fixed the a priori nutation to IAU2006 precession-nutation model plus IERS 14 C04 series corrections in the VLBI analysis that is consistent with the IERS2010 conventions. However, it is seen at Fourier plots that nutation parameters propagated into polar motion coordinates. Another reason of the differences of estimated x_p and y_p w.r.t. the IERS2010 model would be network geometry as previously referred. In general, IVS-CONT campaigns were performed with similar VLBI stations for every realization. But in fact, IVS-CONT08, and -CONT14 campaigns do not have stations at Australia, southern side of South America, respectively. Besides, CONT17 campaigns were organized as two different legacies (networks), and legacy-1 does not cover stations at North America and the southern side of South America (TIGOCONC). These lack of stations may limit the accuracy of ERP determination. The Fourier transforms of polar motion and $\Delta UT1$ for whole duration between starting of 2000 and end of 2018 are not possible because of unevenly spaced epochs of estimates. There is no observation carried out by IVS except Mondays and Thursdays in general. Hence, we only investigated evenly spaced epochs of CONT campaigns by means of Fourier transform.

Table 8.3: Means and standard deviations of the hourly x_p, y_p and ΔUT1 series estimated from VLBI observations with respect to the IERS2010 model during the last four IVS-CONT campaigns.

Campaign	x_p in μas	y_p in μas	ΔUT1 in μs
CONT08$_{(VLBI-IERS2010)}$	-50.2 ± 349.4	-15.0 ± 347.4	-2.2 ± 14.4
CONT11$_{(VLBI-IERS2010)}$	-1.5 ± 185.1	-79.7 ± 179.5	-6.6 ± 13.1
CONT14$_{(VLBI-IERS2010)}$	66.6 ± 185.0	37.6 ± 209.8	-2.6 ± 14.8
CONT17$_{(VLBI-IERS2010)}$	246.0 ± 291.3	-137.2 ± 346.9	-24.0 ± 20.3

8.3. TIDEST - Tidal Constituent Estimation Software

TIDEST is a software built for amplitude estimation of tidal constituents from ERP series developed in the MATLAB (2018) programming language (back-end) and its extension GUIDE graphical user interface design tool (front-end) in the content of this thesis. Basically, TIDEST provides following options with a graphical user interface as shown in Figure (8.2):

- Observed ERP series
  x_p, y_p and $\Delta UT1$ time series with their formal errors in a ".mat" file should be imported via pop-up file browser menu into TIDEST for tidal amplitudes estimation. The time series may be either residuals w.r.t. an a priori series or total values.

- Daily ERP series to reduce from observations (the total values of ERP) a priori to the parameter estimation
  If imported ERP are the total values, TIDEST reduces total ERP series w.r.t. a daily a priori ERP series before the parameter estimation. The daily a priori ERP series are interpolated to the epochs of daily ERP series with either Lagrange (Abramowitz and Stegun, 2013) or linear interpolation methods. The IERS daily ERP series should be up-to-date in the subroutine of TIDEST software. The daily ERP series can be imported from e.g.
  - IERS 14 C04
  - from any series formatted as a text file including blank spaced columns.

- Handle outliers
  Handling outlier at parameter level is performed in TIDEST as well. In order for detection of outliers in x_p, y_p, and $\Delta UT1$ time series, TIDEST is looking for observations with formal errors greater than three times of the median of formal (standard) errors. Then, specified outliers are written in a text file to book keep. Elimination of outliers is executed for those in the text file in the second run. For further runs, the same outlier detection criterion is applied, after initial outliers are eliminated, then outliers can be appended to the text file again in a second run. The options of outlier handling tool are given below.
  - skip outlier handling
  - eliminate outliers
  - detect and eliminate outliers

- Apriori high-frequency ERP model
  Tides that are not estimated will be fixed to the a priori ERP model and reduced from ERP time series a priori to the amplitude estimation.

- Estimation method

  The following three estimation methods are available in TIDEST already. The details about the estimation method were given in Chapter (3)

  - least squares

  - singular value decomposition

  - complex demodulation

- Selection of the type of tides to be estimated

  The user is allowed to choose tides to be estimated simultaneously from following options.

  - all tides

  - 8 major tides

  - 41 diurnal tides

  - 30 semi-diurnal tides

  - manual tide selection

- Processing

  The "Estimate!" button is saving the selections as a ".mat" file for later use, and writing amplitudes of tidal constituents to a text file. If some of the tides are fixed to the a priori model, the amplitudes of these tides are written in a text file and taken from the model.
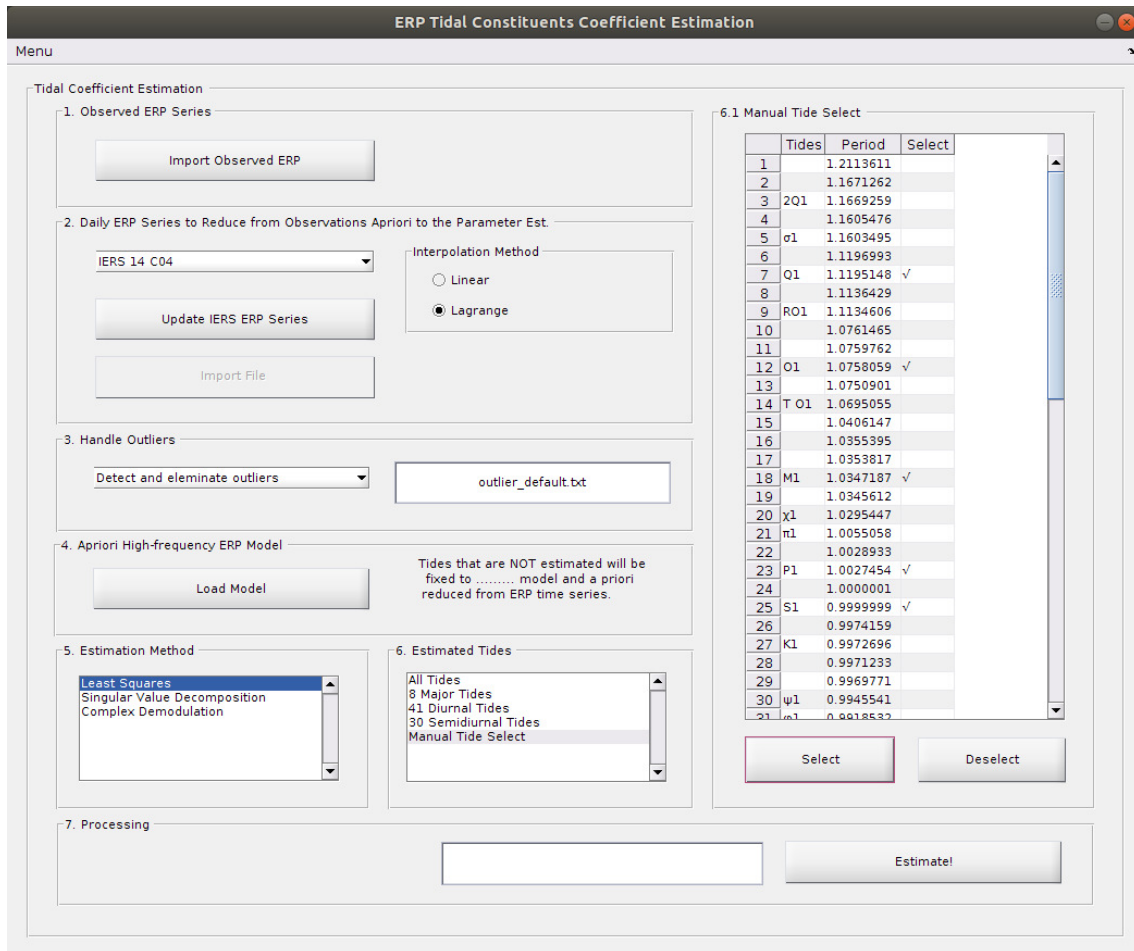
Figure 8.2: Graphical user interface of TIDEST software.
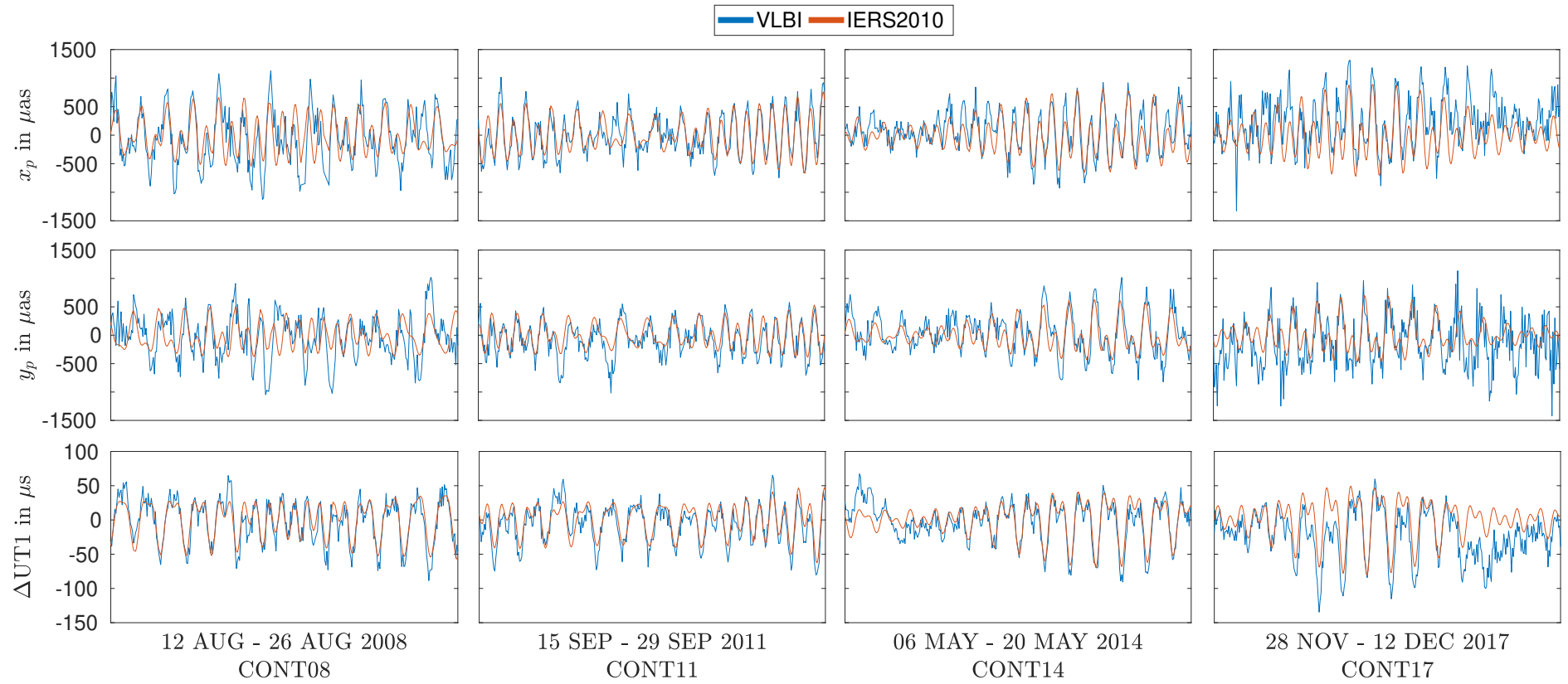
Figure 8.3: Hourly time series of x_p, y_p in μas and ΔUT1 in μs from the VLBI observations and the IERS2010 model during last four IVS-CONT campaigns.
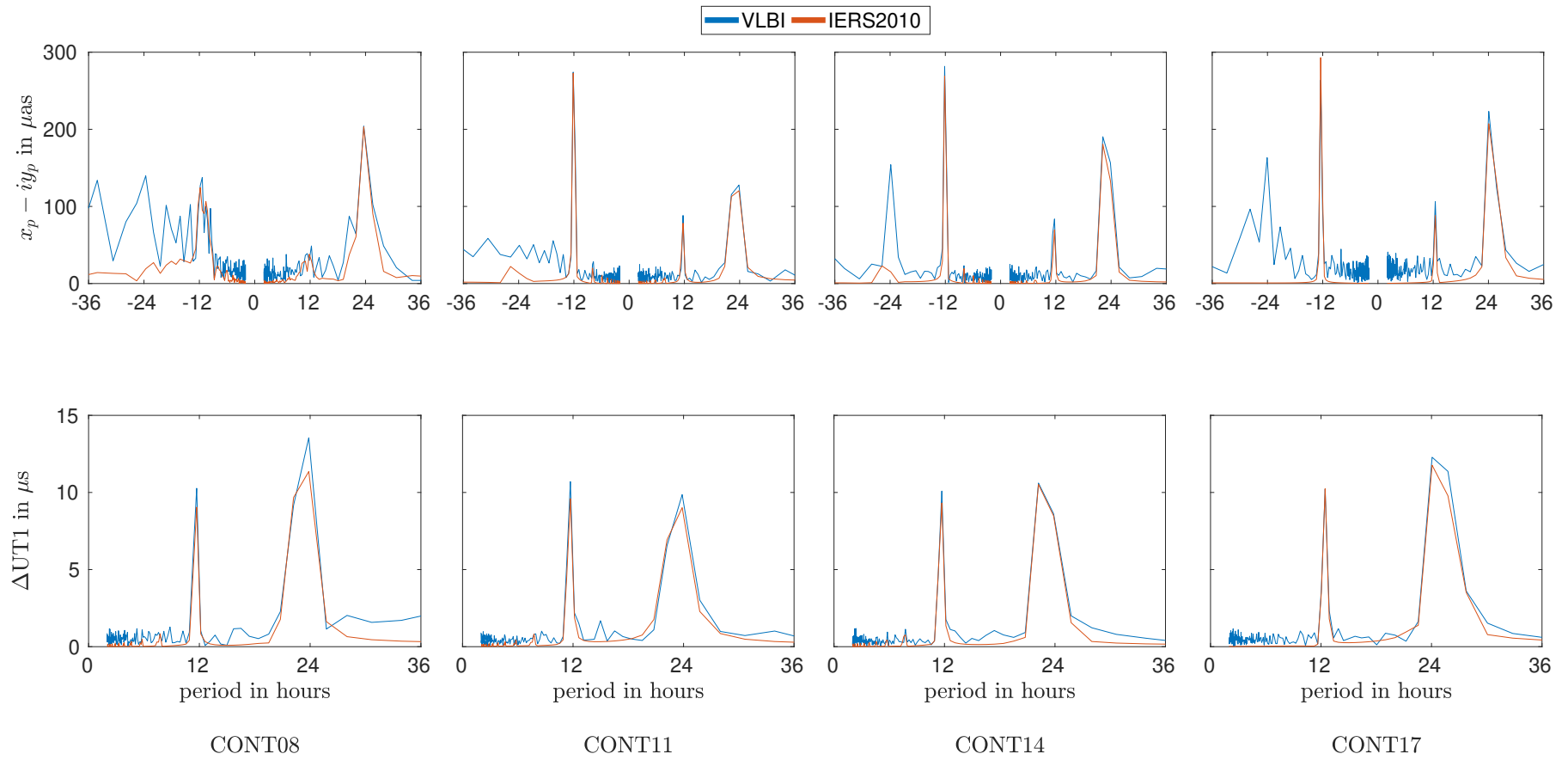
Figure 8.4: Fourier transforms of $x_p - iy_p$ in μas and ΔUT1 in μs from the VLBI observations and the IERS2010 model during last four IVS-CONT campaigns.

8.4. Tidal Amplitude Estimation

Estimation of tidal amplitudes means that in principle modeling physical impact on Earth rotation using sine and cosine components. The previous works for modeling the high-frequency ERP variations due to ocean tides may be referred to Rothacher et al. (2001); Artz, Tesmer née Böckmann and Nothnagel (2011); Böhm, Brzeziński and Schuh (2012); Desai and Sibois (2016). We used three different estimation methods for extracting the amplitude from the time series of x_p, y_p, and $\Delta UT1$: Least squares (LS), singular value decomposition (SVD) and complex demodulation (CD).

The least squares is a remarkable tool for equation fitting (estimating the parameters) by minimizing the sum of the weighted squares of post-fit observational residuals. The least squares estimation method is explicated at Chapter (3). The method may be simply applied to tidal constituents estimation from ERP time series by fitting aforesaid sub-daily ERP model in Chapter (2). Here, matrices are exemplified for x_p only, but also setup for y_p as well as $\Delta UT1$ with appropriate coefficients in the thesis work. The functional model for 71 tidal constituents and n observations each having sine and cosine amplitudes, A_k and B_k is as follows

$$
\begin{bmatrix} x_p(t_1) \\ x_p(t_2) \\ \vdots \\ x_p(t_n) \end{bmatrix} = \begin{bmatrix} sin(\xi_1(t_1)) & cos(\xi_1(t_1)) & \cdots & cos(\xi_{71}(t_1)) \\ sin(\xi_2(t_2)) & cos(\xi_1(t_2)) & \cdots & cos(\xi_{71}(t_2)) \\ \vdots & \vdots & \vdots & \vdots \\ sin(\xi_1(t_n)) & cos(\xi_1(t_n)) & \cdots & cos(\xi_{71}(t_n)) \end{bmatrix} \cdot \begin{bmatrix} A_1 \\ B_1 \\ \vdots \\ B_{71} \end{bmatrix} \tag{8.1}
$$

and its matrix notation is

$$
l = A\,x \tag{8.2}
$$

where l is a time series of ERP, A is the design matrix containing sine and cosine values, x is the coefficients matrix. Under the condition of $minimize \ ||Ax - l||^2$, estimated parameter vector x is derived as below

$$
x = (A^T A)^- A^T l, \tag{8.3}
$$

The singular value decomposition (SVD) is an alternative technique in order to find solution of Equation (8.2). Details about derivations can be found in Chapter (3). Similar to LS solution, Moore-Penrose inverse of design matrix should be acquired but in a way as shown below

$$
A^+ = V\Sigma^+ U^T. \tag{8.4}
$$

Then, the vector containing amplitudes x can be derived as given

$$x = V\Sigma^+ U^T l. \tag{8.5}$$

Estimated polar motion components (x_p, y_p) and $\Delta UT1$ are under influences of sub-daily tides as well as instrumentation and estimation noises. Each of the tidal constituent was defined with a tidal frequency and an amplitude. In order to extract amplitude of a particular tide from the time series of polar motion and $\Delta UT1$ estimates, complex demodulation was suggested by Böhm, Brzeziński and Schuh (2012); Brzeziński (2012); Brzeziński and Böhm (2012). Derivation of A_k and B_k amplitudes are shown as follows

$$A_k = \mathbb{Re}[LPF[x_p(t)e^{i\xi_k(t)}]]$$
$$B_k = \mathbb{Im}[LPF[x_p(t)e^{i\xi_k(t)}]] \tag{8.6}$$

where unit imaginary number $i = \sqrt{-1}$, $\mathbb{Re}$ denotes real, and $\mathbb{Im}$ refers imaginary part of complex number. LPF is low-pass-filter allows passing only the low frequency component of the signal.

Estimated amplitudes and estimation errors of all 71 tides of sub-daily ERP variations due to ocean tides from the least squares, singular value decomposition and complex demodulation solutions alongside those derived from the IERS2010 model are given in Tables (8.4, 8.5, 8.6, 8.7, 8.8, and 8.9) for diurnal and semi-diurnal x_p, y_p and $\Delta UT1$, respectively. However, estimation error could not be provided for complex demodulation method owing to its mathematical basis. The major tides which have the greatest impacts on total movement are thought to be properly estimated for all ERP by all three methods. In the meantime, it should be stated that S_1 tide ($period = 0.9999999$) and its nearest tide ($period = 1.0000001$) are closest tides in terms of their periods among all tidal constituents, and the estimation error is so high for these tides. This indicates that the solutions used can not de-correlate these neighboring tides from the time series due to Rayleigh criterion (Foreman, 1977). Simultaneous estimations of all tides, from the estimation methods of least squares and singular value decomposition, were failed for these closest tides as seen in Tables (8.4, 8.5, 8.6, 8.7, 8.8, and 8.9). However, complex demodulation put forward better estimation for these tides due to the disjoint estimation for each of tides. The IERS2010 model values will not remain permanent for several decades. Therefore, our amplitude estimates can be used as a replacement of the IERS sub-daily ERP model, even though they differ from the IERS2010 model for several tides. On the other hand, estimated tidal amplitudes of this thesis needed to be validated somehow. However, its decided to put the validation of the results out of the scope of this thesis. Nevertheless, the level of agreement between the IERS2010 model and our results is investigated.

Table 8.4: Estimated amplitudes for k^{th} **diurnal tide** of x_p in μas.

Tide	Period (days)	IERS2010 A_k	B_k	Least Squares A_k	B_k	Singular Value Decomposition A_k	B_k	Complex Demodulation A_k	B_k
	1.2113611	-0.05	0.94	-2.89 ± 2.25	4.67 ± 2.26	-3.71 ± 2.94	-1.25 ± 2.94	-1.35	-1.05
	1.1671262	0.06	0.64	-1.83 ± 2.29	6.94 ± 2.31	-0.60 ± 2.95	2.34 ± 2.95	-0.84	1.04
$2Q_1$	1.1669259	0.30	3.42	-6.66 ± 2.28	1.55 ± 2.31	-3.79 ± 2.94	0.41 ± 2.97	-2.24	4.39
	1.1605476	0.08	0.78	2.87 ± 2.29	4.30 ± 2.28	2.47 ± 2.95	4.96 ± 2.94	2.56	2.39
σ_1	1.1603495	0.46	4.15	3.81 ± 2.30	2.50 ± 2.29	-0.44 ± 2.95	8.23 ± 2.95	2.38	8.13
	1.1196993	1.19	4.96	-7.32 ± 2.30	15.73 ± 2.30	-0.39 ± 2.94	15.40 ± 2.95	-1.91	17.73
Q_1	1.1195148	6.24	26.31	4.10 ± 2.30	32.90 ± 2.30	6.62 ± 2.95	18.89 ± 2.94	4.92	16.06
	1.1136429	0.24	0.94	5.39 ± 2.30	-2.08 ± 2.30	3.92 ± 2.94	-2.22 ± 2.95	3.64	-0.20
RO_1	1.1134606	1.28	4.99	2.51 ± 2.30	-2.53 ± 2.30	-0.50 ± 2.94	-2.53 ± 2.95	-2.76	-3.89
	1.0761465	-0.28	-0.77	-8.35 ± 2.38	10.95 ± 2.38	-5.68 ± 2.96	16.13 ± 2.97	4.70	18.65
	1.0759762	9.22	25.06	14.78 ± 2.33	15.64 ± 2.33	9.13 ± 2.95	17.14 ± 2.95	4.30	18.95
O_1	1.0758059	48.82	132.91	68.24 ± 2.35	127.97 ± 2.35	67.08 ± 2.96	108.11 ± 2.97	60.05	105.79
	1.0750901	-0.32	-0.86	5.81 ± 2.34	10.10 ± 2.32	2.67 ± 2.95	4.71 ± 2.95	2.57	1.30
TO_1	1.0695055	-0.66	-1.72	-1.17 ± 2.28	4.60 ± 2.28	-3.74 ± 2.94	6.87 ± 2.95	-1.24	12.57
	1.0406147	-0.42	-0.92	0.79 ± 2.28	4.15 ± 2.29	2.27 ± 2.95	-1.01 ± 2.95	1.34	1.97
	1.0355395	-0.30	-0.64	5.34 ± 2.35	-5.95 ± 2.35	7.06 ± 2.95	-5.18 ± 2.95	7.98	-9.00
	1.0353817	-1.61	-3.46	-3.17 ± 2.33	-7.81 ± 2.33	-4.51 ± 2.96	0.44 ± 2.95	-5.80	-1.74
M_1	1.0347187	-4.48	-9.61	0.21 ± 2.32	-3.62 ± 2.32	-2.49 ± 2.95	-2.74 ± 2.95	-2.11	2.59
	1.0345612	-0.90	-1.93	-2.32 ± 2.35	-0.88 ± 2.35	0.60 ± 2.95	1.22 ± 2.95	4.08	2.19
χ_1	1.0295447	-0.86	-1.81	2.26 ± 2.30	9.27 ± 2.31	8.33 ± 2.95	5.95 ± 2.95	9.35	5.46

Tide	Period	IERS2010		Least Squares		Singular Value Decomposition		Complex Demodulation	
	(days)	A_k	B_k	A_k	B_k	A_k	B_k	A_k	B_k
π_1	1.0055058	1.54	3.03	11.38 ± 2.32	0.60 ± 2.32	8.11 ± 2.96	-0.70 ± 2.95	5.68	0.31
	1.0028933	-0.29	-0.58	-5.21 ± 2.32	0.73 ± 2.32	-1.03 ± 2.95	0.73 ± 2.95	-5.67	-7.17
P_1	1.0027454	26.13	51.25	19.99 ± 2.34	41.44 ± 2.34	19.97 ± 2.95	33.04 ± 2.95	17.09	25.08
	1.0000001	-0.22	-0.42	1374.84 ± 783.69	3910.88 ± 753.35	1786.24 ± 965.78	2643.07 ± 947.08	-1.77	6.17
S_1	0.9999999	-0.61	-1.20	2958.85 ± 782.73	2900.34 ± 754.35	2766.26 ± 969.28	1583.09 ± 943.51	-1.11	-6.29
	0.9974159	1.54	3.00	12.90 ± 2.39	-8.35 ± 2.37	12.46 ± 2.99	1.92 ± 2.98	14.09	-0.51
K_1	0.9972696	-77.48	-151.74	-72.72 ± 2.34	-153.14 ± 2.47	-70.85 ± 2.96	-142.85 ± 2.98	-67.59	-134.17
	0.9971233	-10.52	-20.56	-28.00 ± 2.38	-24.81 ± 2.36	-15.90 ± 2.97	-27.93 ± 2.96	-22.21	-19.67
	0.9969771	0.23	0.44	-12.95 ± 2.37	8.47 ± 2.36	-12.92 ± 2.97	10.67 ± 2.97	-11.42	-5.37
ψ_1	0.9945541	-0.61	-1.19	-13.67 ± 2.31	1.19 ± 2.33	-10.96 ± 2.95	-0.17 ± 2.95	-13.90	-0.15
ϕ_1	0.9918532	-1.09	-2.11	-1.80 ± 2.32	-15.25 ± 2.32	-5.57 ± 2.95	-11.25 ± 2.95	-10.90	-14.88
TT_1	0.9669565	-0.69	-1.43	2.47 ± 2.28	5.70 ± 2.29	-2.51 ± 2.95	2.95 ± 2.94	-1.13	4.76
J_1	0.9624365	-3.46	-7.28	-8.62 ± 2.29	4.17 ± 2.29	-6.84 ± 2.95	4.15 ± 2.94	-5.82	3.45
	0.9623003	-0.69	-1.44	3.77 ± 2.32	-9.26 ± 2.31	0.35 ± 2.95	-14.74 ± 2.95	-3.02	-11.58
So_1	0.9341741	-0.37	-1.06	-3.82 ± 2.28	-1.56 ± 2.28	0.49 ± 2.95	4.87 ± 2.95	-0.27	7.16
	0.9299547	-0.17	-0.51	-6.14 ± 2.32	-3.28 ± 2.33	-5.19 ± 2.95	-1.28 ± 2.96	-0.35	-9.16
Oo_1	0.9294198	-1.10	-3.42	-0.42 ± 2.33	-6.63 ± 2.34	-6.54 ± 2.96	-11.62 ± 2.96	-3.16	-10.24
	0.9292927	-0.70	-2.19	-7.87 ± 2.31	-7.42 ± 2.31	-1.13 ± 2.95	-8.20 ± 2.95	-3.14	-9.74
	0.9291657	-0.15	-0.46	-3.50 ± 2.36	3.27 ± 2.37	-0.41 ± 2.96	0.82 ± 2.97	1.23	-2.58
ν_1	0.8990932	-0.03	-0.59	-0.38 ± 2.29	-4.94 ± 2.29	-2.64 ± 2.95	-5.82 ± 2.96	-4.21	-4.92
	0.8989743	-0.02	-0.38	-4.02 ± 2.28	-8.83 ± 2.29	-0.50 ± 2.94	-1.45 ± 2.95	-0.24	-0.89

Table 8.5: Estimated amplitudes for k^{th} **semi-diurnal tide** of x_p in μas.

Tide	Period	IERS2010		Least Squares		Singular Value Decomposition		Complex Demodulation	
	(days)	A_k	B_k	A_k	B_k	A_k	B_k	A_k	B_k
	0.5484264	-0.49	-0.04	0.04 ± 2.25	-6.87 ± 2.25	-1.79 ± 2.94	-3.04 ± 2.94	-3.20	-0.97
	0.5469695	-1.33	-0.17	-0.89 ± 2.24	1.07 ± 2.23	-0.53 ± 2.94	1.59 ± 2.94	2.77	3.56
$2N_2$	0.5377239	-6.08	-1.61	-7.00 ± 2.28	2.76 ± 2.28	-11.90 ± 2.96	-0.49 ± 2.96	-12.42	4.51
μ_2	0.5363232	-7.59	-2.05	-9.19 ± 2.26	-5.16 ± 2.25	-10.44 ± 2.93	-5.23 ± 2.94	-10.50	-1.30
	0.5355369	-0.52	-0.14	-2.59 ± 2.25	-0.50 ± 2.26	-1.21 ± 2.94	-2.04 ± 2.94	1.33	-4.58
	0.5281939	0.47	0.11	0.03 ± 2.28	-3.15 ± 2.28	-1.34 ± 2.94	-1.92 ± 2.94	1.60	-3.13
	0.5274721	2.12	0.49	3.80 ± 2.30	0.29 ± 2.30	3.08 ± 2.94	0.29 ± 2.94	3.00	-7.67
N_2	0.5274312	-56.87	-12.93	-53.23 ± 2.28	-12.22 ± 2.29	-46.13 ± 2.94	-14.17 ± 2.94	-41.96	-11.87
	0.5266707	-0.54	-0.12	-3.37 ± 2.27	-1.78 ± 2.28	-7.27 ± 2.95	0.09 ± 2.95	-6.41	2.91
ν_2	0.5260835	-11.01	-2.40	-8.09 ± 2.29	-4.41 ± 2.28	-6.37 ± 2.94	-6.08 ± 2.94	-7.77	1.84
	0.5253269	-0.51	-0.11	-0.42 ± 2.27	-1.72 ± 2.26	4.15 ± 2.94	-3.79 ± 2.93	5.26	-5.30
	0.5188292	0.98	0.11	2.84 ± 2.28	1.18 ± 2.29	-0.36 ± 2.94	-2.57 ± 2.94	0.48	-9.35
	0.5182593	1.13	0.11	2.08 ± 2.29	2.56 ± 2.28	-1.23 ± 2.94	4.50 ± 2.95	-1.57	8.96
	0.5175645	12.32	1.00	22.88 ± 2.30	-1.97 ± 2.30	21.25 ± 2.94	-2.78 ± 2.94	21.77	-13.02
M_2	0.5175251	-330.15	-26.96	-315.25 ± 2.28	-9.20 ± 2.27	-278.64 ± 2.94	-7.67 ± 2.93	-272.28	-5.40

Tide	Period	IERS2010		Least Squares		Singular Value Decomposition		Complex Demodulation	
	(days)	A_k	B_k	A_k	B_k	A_k	B_k	A_k	B_k
	0.5167928	-1.01	-0.07	-1.08 ± 2.29	-0.38 ± 2.29	-1.74 ± 2.94	0.52 ± 2.94	0.23	0.39
λ_2	0.5092406	2.47	-0.28	2.13 ± 2.26	1.06 ± 2.27	7.55 ± 2.94	-2.81 ± 2.94	8.76	-4.95
L_2	0.5079842	9.40	-1.44	10.43 ± 2.28	-1.63 ± 2.28	12.87 ± 2.94	3.47 ± 2.94	13.00	4.14
	0.5078245	-2.35	0.37	-3.43 ± 2.30	1.30 ± 2.30	-6.84 ± 2.94	1.34 ± 2.95	-9.03	-5.11
	0.5077866	-1.04	0.17	-0.77 ± 2.31	-3.92 ± 2.32	1.09 ± 2.95	1.87 ± 2.96	-2.94	0.46
T_2	0.5006854	-8.51	3.50	-7.31 ± 2.28	5.58 ± 2.30	-5.32 ± 2.94	7.09 ± 2.95	-5.77	15.71
S_2	0.5000000	-144.13	63.56	-133.65 ± 2.22	73.63 ± 2.33	-120.45 ± 2.91	71.09 ± 2.98	-121.94	63.55
R_2	0.4993165	1.19	-0.56	3.96 ± 2.28	1.76 ± 2.28	1.96 ± 2.95	-1.54 ± 2.95	-1.33	4.49
	0.4986714	0.49	-0.25	2.16 ± 2.33	-1.46 ± 2.32	6.58 ± 2.96	0.47 ± 2.97	4.84	0.23
K_2	0.4986348	-38.48	19.14	-41.03 ± 2.37	17.33 ± 2.35	-36.98 ± 2.96	11.85 ± 2.96	-43.62	10.62
	0.4985982	-11.44	5.75	-5.14 ± 2.34	0.57 ± 2.34	-7.57 ± 2.96	-1.93 ± 2.96	-12.19	-0.74
	0.4985616	-1.24	0.63	-0.71 ± 2.32	3.62 ± 2.32	4.92 ± 2.96	2.07 ± 2.96	-0.58	-1.70
	0.4897717	-1.77	1.79	-4.36 ± 2.27	3.22 ± 2.28	-6.82 ± 2.94	3.38 ± 2.94	-8.49	2.09
	0.4897365	-0.77	0.78	3.35 ± 2.28	1.13 ± 2.27	1.00 ± 2.95	-1.83 ± 2.94	1.88	-0.82
	0.4810750	-0.33	0.62	0.97 ± 2.24	-0.47 ± 2.25	-0.25 ± 2.94	0.16 ± 2.94	-4.44	-2.15

Table 8.6: Estimated amplitudes for k^{th} **diurnal tide** of y_p in μas.

Tide	Period	IERS2010		Least Squares		Singular Value Decomposition		Complex Demodulation	
	(days)	A'_k	B'_k	A'_k	B'_k	A'_k	B'_k	A'_k	B'_k
	1.2113611	-0.94	-0.05	-2.93 ± 2.36	2.14 ± 2.36	0.93 ± 3.10	5.23 ± 3.09	2.67	7.67
	1.1671262	-0.64	0.06	-1.74 ± 2.40	-2.70 ± 2.41	-9.13 ± 3.10	-4.67 ± 3.10	-8.86	-1.25
$2Q_1$	1.1669259	-3.42	0.30	-7.71 ± 2.39	6.60 ± 2.43	-6.48 ± 3.09	7.55 ± 3.12	-4.17	5.67
	1.1605476	-0.78	0.08	-2.94 ± 2.39	-7.06 ± 2.40	0.66 ± 3.10	-12.23 ± 3.09	1.94	-12.98
σ_1	1.1603495	-4.15	0.45	-2.53 ± 2.41	-2.39 ± 2.40	0.78 ± 3.10	-0.18 ± 3.10	0.14	0.71
	1.1196993	-4.96	1.19	-3.24 ± 2.41	5.02 ± 2.42	4.50 ± 3.10	2.39 ± 3.10	3.08	-0.38
Q_1	1.1195148	-26.31	6.23	-30.00 ± 2.40	6.12 ± 2.42	-33.99 ± 3.10	2.10 ± 3.09	-32.26	-0.37
	1.1136429	-0.94	0.24	-1.30 ± 2.41	-2.18 ± 2.42	-5.56 ± 3.09	0.37 ± 3.10	-9.19	0.40
RO_1	1.1134606	-4.99	1.28	-5.08 ± 2.41	-2.76 ± 2.42	-0.70 ± 3.10	6.84 ± 3.10	-1.67	6.07
	1.0761465	0.77	-0.28	6.52 ± 2.48	5.67 ± 2.49	8.62 ± 3.12	2.20 ± 3.12	2.00	11.21
	1.0759762	-25.06	9.22	-24.99 ± 2.44	1.91 ± 2.44	-15.12 ± 3.10	1.96 ± 3.10	-16.40	-1.31
O_1	1.0758059	-132.90	48.82	-123.94 ± 2.46	53.86 ± 2.46	-104.70 ± 3.11	43.55 ± 3.12	-103.38	44.08
	1.0750901	0.86	-0.32	12.15 ± 2.44	-6.94 ± 2.45	6.91 ± 3.11	-0.47 ± 3.11	6.62	-0.22
TO_1	1.0695055	1.72	-0.66	7.96 ± 2.40	10.17 ± 2.40	6.70 ± 3.09	5.54 ± 3.10	1.83	6.97
	1.0406147	0.92	-0.42	3.83 ± 2.41	-3.21 ± 2.42	-3.35 ± 3.10	-5.00 ± 3.10	-2.86	-5.47
	1.0355395	0.64	-0.30	-0.84 ± 2.47	-0.61 ± 2.47	-4.26 ± 3.10	-8.68 ± 3.11	-0.07	-8.17
	1.0353817	3.46	-1.61	-9.08 ± 2.44	8.04 ± 2.45	0.77 ± 3.11	7.53 ± 3.10	0.68	8.56
M_1	1.0347187	9.61	-4.48	11.93 ± 2.43	0.85 ± 2.43	14.41 ± 3.10	8.58 ± 3.10	13.14	7.03
	1.0345612	1.93	-0.90	3.45 ± 2.46	0.35 ± 2.47	-1.23 ± 3.11	-0.58 ± 3.10	0.20	4.33
χ_1	1.0295447	1.81	-0.86	14.55 ± 2.43	-2.28 ± 2.42	8.79 ± 3.10	-4.58 ± 3.10	8.52	-4.61

Tide	Period (days)	IERS2010 A'_k	B'_k	Least Squares A'_k	B'_k	Singular Value Decomposition A'_k	B'_k	Complex Demodulation A'_k	B'_k
π_1	1.0055058	-3.03	1.54	-5.31 ± 2.44	-5.78 ± 2.46	-5.75 ± 3.11	-1.72 ± 3.11	-5.26	-3.22
	1.0028933	0.58	-0.29	6.15 ± 2.44	-0.44 ± 2.45	8.39 ± 3.10	-2.60 ± 3.10	10.31	-9.17
P_1	1.0027454	-51.25	26.13	-42.57 ± 2.44	32.00 ± 2.49	-37.60 ± 3.10	29.19 ± 3.11	-32.59	19.45
	1.0000001	0.42	-0.22	1245.96 ± 831.43	155.43 ± 792.76	910.26 ± 1015.45	784.91 ± 995.78	-16.46	-19.88
S_1	0.9999999	1.20	-0.61	1210.66 ± 833.63	-392.96 ± 790.42	1185.38 ± 1019.13	319.56 ± 992.03	23.56	10.57
	0.9974159	-3.00	1.54	-5.89 ± 2.48	-3.36 ± 2.50	-4.93 ± 3.14	-5.17 ± 3.14	-1.98	-0.33
K_1	0.9972696	151.74	-77.48	144.85 ± 2.58	-116.98 ± 2.48	122.94 ± 3.12	-104.46 ± 3.13	121.38	-101.29
	0.9971233	20.56	-10.52	8.42 ± 2.47	-1.53 ± 2.49	3.08 ± 3.12	-7.28 ± 3.12	-0.87	-12.39
	0.9969771	-0.44	0.23	9.31 ± 2.47	10.59 ± 2.49	9.28 ± 3.12	10.56 ± 3.12	23.00	10.57
ψ_1	0.9945541	1.19	-0.61	-2.22 ± 2.45	8.49 ± 2.44	-4.47 ± 3.11	4.69 ± 3.10	-5.93	5.96
ϕ_1	0.9918532	2.11	-1.09	-11.77 ± 2.44	2.67 ± 2.46	-5.57 ± 3.10	5.79 ± 3.10	-3.39	-1.70
TT_1	0.9669565	1.43	-0.69	4.68 ± 2.40	-5.38 ± 2.40	5.30 ± 3.10	-0.34 ± 3.10	2.08	-0.59
J_1	0.9624365	7.28	-3.46	19.06 ± 2.40	-6.37 ± 2.40	4.80 ± 3.10	-8.52 ± 3.09	1.49	-8.19
	0.9623003	1.44	-0.69	-4.77 ± 2.43	-2.39 ± 2.43	-6.37 ± 3.10	3.05 ± 3.10	-6.85	-0.82
So_1	0.9341741	1.06	-0.37	1.39 ± 2.40	4.89 ± 2.40	9.22 ± 3.10	1.55 ± 3.10	14.01	4.29
	0.9299547	0.51	-0.17	-1.57 ± 2.43	5.06 ± 2.43	-2.98 ± 3.10	8.45 ± 3.11	-3.93	6.60
Oo_1	0.9294198	3.42	-1.09	-7.44 ± 2.45	-7.14 ± 2.45	-11.76 ± 3.11	-1.04 ± 3.11	-6.90	-1.10
	0.9292927	2.19	-0.70	3.10 ± 2.43	-1.08 ± 2.43	3.92 ± 3.10	1.81 ± 3.10	4.45	3.88
	0.9291657	0.46	-0.15	10.10 ± 2.47	1.87 ± 2.47	10.83 ± 3.12	5.33 ± 3.12	8.31	3.92
ν_1	0.8990932	0.59	-0.03	-1.85 ± 2.40	-2.89 ± 2.40	-0.24 ± 3.10	-3.93 ± 3.11	1.08	-4.83
	0.8989743	0.38	-0.02	-13.96 ± 2.40	-1.66 ± 2.39	-2.58 ± 3.10	-3.24 ± 3.10	-3.74	-1.99

Table 8.7: Estimated amplitudes for k^{th} **semi-diurnal tide** of y_p in μas.

Tide	Period	IERS2010		Least Squares		Singular Value Decomposition		Complex Demodulation	
	(days)	A'_k	B'_k	A'_k	B'_k	A'_k	B'_k	A'_k	B'_k
	0.5484264	0.63	0.24	-0.87 ± 2.35	8.17 ± 2.35	3.87 ± 3.09	8.29 ± 3.09	2.53	8.59
	0.5469695	1.53	0.68	0.12 ± 2.34	4.30 ± 2.34	-5.20 ± 3.09	-1.15 ± 3.09	-4.70	-3.11
$2N_2$	0.5377239	3.13	3.35	8.44 ± 2.39	5.47 ± 2.40	5.14 ± 3.11	5.94 ± 3.11	3.51	2.45
μ_2	0.5363232	3.44	4.23	-1.43 ± 2.36	8.78 ± 2.36	-0.78 ± 3.09	6.11 ± 3.10	1.44	5.63
	0.5355369	0.22	0.29	4.98 ± 2.37	1.73 ± 2.37	2.96 ± 3.09	1.71 ± 3.09	-0.05	1.18
	0.5281939	-0.10	-0.27	-3.36 ± 2.40	4.73 ± 2.41	0.47 ± 3.09	4.07 ± 3.10	-0.66	1.63
	0.5274721	-0.41	-1.23	-0.57 ± 2.41	-3.28 ± 2.41	1.96 ± 3.09	-0.29 ± 3.10	-1.46	2.39
N_2	0.5274312	11.15	32.88	6.22 ± 2.39	30.87 ± 2.40	5.43 ± 3.09	25.52 ± 3.09	5.81	23.43
	0.5266707	0.10	0.31	0.32 ± 2.39	0.44 ± 2.40	-2.50 ± 3.10	3.74 ± 3.11	-2.57	2.63
ν_2	0.5260835	1.89	6.41	1.95 ± 2.41	2.97 ± 2.40	2.60 ± 3.10	0.03 ± 3.09	4.62	-2.17
	0.5253269	0.08	0.30	-5.54 ± 2.38	-1.76 ± 2.38	-9.17 ± 3.09	-2.67 ± 3.08	-9.80	-2.12
	0.5188292	-0.11	-0.58	0.52 ± 2.41	-2.90 ± 2.41	3.02 ± 3.09	-0.09 ± 3.10	-2.21	-0.21
	0.5182593	-0.13	-0.67	1.20 ± 2.40	1.81 ± 2.41	0.06 ± 3.10	7.69 ± 3.10	-1.65	11.32
	0.5175645	-1.41	-7.31	-10.48 ± 2.41	-14.84 ± 2.41	-7.76 ± 3.09	-17.26 ± 3.09	-12.15	-16.36
M_2	0.5175251	37.58	195.92	53.92 ± 2.38	184.10 ± 2.38	47.35 ± 3.10	159.41 ± 3.08	45.36	158.61

Tide	Period (days)	IERS2010		Least Squares		Singular Value Decomposition		Complex Demodulation	
		A'_k	B'_k	A'_k	B'_k	A'_k	B'_k	A'_k	B'_k
	0.5167928	0.11	0.60	-5.04 ± 2.42	3.93 ± 2.42	-2.74 ± 3.09	6.87 ± 3.09	-3.88	7.03
λ_2	0.5092406	-0.44	-1.48	6.26 ± 2.38	-2.77 ± 2.38	1.99 ± 3.09	0.37 ± 3.09	0.10	0.91
L_2	0.5079842	-1.88	-5.65	2.45 ± 2.38	-6.20 ± 2.38	0.86 ± 3.09	-2.72 ± 3.10	0.28	-3.61
	0.5078245	0.47	1.41	3.58 ± 2.42	-0.48 ± 2.41	3.47 ± 3.10	-0.97 ± 3.10	2.08	0.74
	0.5077866	0.21	0.62	5.86 ± 2.42	0.07 ± 2.42	5.25 ± 3.11	-0.15 ± 3.11	5.20	2.78
T_2	0.5006854	3.29	5.11	5.62 ± 2.41	3.73 ± 2.42	1.88 ± 3.09	0.57 ± 3.10	4.13	3.09
S_2	0.5000000	59.23	86.56	72.94 ± 2.34	80.78 ± 2.45	62.89 ± 3.06	66.40 ± 3.13	63.41	65.88
R_2	0.4993165	-0.52	-0.72	-3.53 ± 2.39	-3.31 ± 2.41	-4.36 ± 3.10	-7.08 ± 3.10	-9.18	-0.01
	0.4986714	-0.23	-0.29	-0.05 ± 2.44	-2.60 ± 2.43	0.93 ± 3.11	-4.05 ± 3.12	1.38	-1.45
K_2	0.4986348	17.72	23.11	15.48 ± 2.48	19.36 ± 2.47	16.00 ± 3.11	13.11 ± 3.12	19.45	17.59
	0.4985982	5.32	6.87	11.66 ± 2.45	2.52 ± 2.45	5.89 ± 3.11	4.19 ± 3.11	6.92	7.62
	0.4985616	0.58	0.75	6.31 ± 2.43	1.33 ± 2.43	3.01 ± 3.11	1.76 ± 3.11	2.31	4.85
	0.4897717	1.71	1.04	-1.98 ± 2.38	0.29 ± 2.38	-0.97 ± 3.09	0.20 ± 3.10	-0.83	1.56
	0.4897365	0.75	0.45	-3.56 ± 2.38	-0.64 ± 2.39	-5.05 ± 3.10	2.15 ± 3.09	-4.20	1.00
	0.4810750	0.65	0.19	5.58 ± 2.35	-1.15 ± 2.36	5.28 ± 3.09	0.20 ± 3.09	6.27	3.15

Table 8.8: Estimated amplitudes for k^{th} **diurnal tide** of $\Delta UT1$ in μs.

Tide	Period	IERS2010		Least Squares		Singular Value Decomposition		Complex Demodulation	
	(days)	A_k''	B_k''	A_k''	B_k''	A_k''	B_k''	A_k''	B_k''
	1.2113611	0.40	-0.08	0.22 ± 0.14	-0.37 ± 0.14	0.03 ± 0.21	0.07 ± 0.21	0.23	-0.21
	1.1671262	0.20	-0.06	0.83 ± 0.15	0.08 ± 0.15	0.54 ± 0.21	0.12 ± 0.21	0.41	0.21
$2Q_1$	1.1669259	1.03	-0.31	1.41 ± 0.15	0.57 ± 0.15	1.52 ± 0.21	0.49 ± 0.21	1.37	0.38
	1.1605476	0.22	-0.07	0.13 ± 0.15	0.04 ± 0.14	0.08 ± 0.21	0.44 ± 0.21	-0.03	0.28
σ_1	1.1603495	1.19	-0.39	0.62 ± 0.15	-0.22 ± 0.14	0.70 ± 0.21	-0.12 ± 0.21	1.01	-0.15
	1.1196993	0.97	-0.47	0.95 ± 0.15	-0.78 ± 0.15	0.69 ± 0.21	-0.79 ± 0.21	1.37	-0.64
Q_1	1.1195148	5.12	-2.50	5.56 ± 0.15	-3.17 ± 0.15	5.48 ± 0.21	-2.51 ± 0.21	5.29	-2.52
	1.1136429	0.17	-0.09	-0.12 ± 0.15	-0.38 ± 0.15	-0.13 ± 0.21	-0.05 ± 0.21	0.21	-0.04
RO_1	1.1134606	0.91	-0.47	1.01 ± 0.15	-0.33 ± 0.15	0.76 ± 0.21	-0.36 ± 0.21	0.59	-0.28
	1.0761465	-0.09	0.07	-0.29 ± 0.15	0.13 ± 0.15	-0.32 ± 0.21	-0.34 ± 0.21	0.04	-2.07
	1.0759762	3.02	-2.28	3.40 ± 0.15	-2.59 ± 0.15	3.16 ± 0.21	-2.40 ± 0.21	3.87	-1.66
O_1	1.0758059	16.02	-12.07	17.25 ± 0.15	-13.01 ± 0.15	16.73 ± 0.21	-12.46 ± 0.21	16.53	-12.21
	1.0750901	-0.10	0.08	-0.15 ± 0.15	0.05 ± 0.15	-0.37 ± 0.21	0.06 ± 0.21	-0.53	0.13
TO_1	1.0695055	-0.19	0.15	0.53 ± 0.15	0.31 ± 0.15	0.30 ± 0.21	0.56 ± 0.21	0.68	0.11
	1.0406147	-0.08	0.07	-0.22 ± 0.15	0.71 ± 0.15	0.13 ± 0.21	0.64 ± 0.21	0.16	0.85
	1.0355395	-0.06	0.05	-0.28 ± 0.15	-0.12 ± 0.15	-0.38 ± 0.21	-0.09 ± 0.21	-1.08	-0.09
	1.0353817	-0.31	0.27	-0.81 ± 0.15	0.38 ± 0.15	-0.95 ± 0.21	0.28 ± 0.21	-0.90	0.37
M_1	1.0347187	-0.86	0.75	-1.05 ± 0.15	0.38 ± 0.15	-0.90 ± 0.21	0.37 ± 0.21	-0.74	0.49
	1.0345612	-0.17	0.15	-0.60 ± 0.15	-0.10 ± 0.15	-0.56 ± 0.21	-0.10 ± 0.21	-0.36	-0.81
χ_1	1.0295447	-0.16	0.14	-0.39 ± 0.15	-0.06 ± 0.15	-0.54 ± 0.21	-0.11 ± 0.21	-0.29	-0.08

Tide	Period (days)	IERS2010 A_k''	IERS2010 B_k''	Least Squares A_k''	Least Squares B_k''	Singular Value Decomposition A_k''	Singular Value Decomposition B_k''	Complex Demodulation A_k''	Complex Demodulation B_k''
π_1	1.0055058	0.32	-0.19	0.25 ± 0.15	-0.32 ± 0.15	0.19 ± 0.21	-0.35 ± 0.21	0.27	-0.06
	1.0028933	-0.06	0.04	-0.28 ± 0.15	-0.04 ± 0.15	-0.15 ± 0.21	-0.04 ± 0.21	-0.62	0.61
P_1	1.0027454	5.51	-3.10	5.77 ± 0.15	-3.70 ± 0.15	5.59 ± 0.21	-3.39 ± 0.21	5.49	-2.89
	1.0000001	-0.05	0.03	-63.11 ± 51.26	138.21 ± 48.84	-58.66 ± 69.38	136.79 ± 68.30	0.30	0.70
S_1	0.9999999	-0.13	0.07	3.52 ± 51.13	151.13 ± 48.97	7.40 ± 69.54	147.89 ± 68.13	-0.58	-0.49
	0.9974159	0.35	-0.17	0.49 ± 0.15	-0.02 ± 0.15	0.47 ± 0.21	0.28 ± 0.21	-0.09	-0.18
K_1	0.9972696	-17.62	8.55	-17.36 ± 0.15	8.78 ± 0.15	-16.39 ± 0.21	8.87 ± 0.21	-15.98	8.60
	0.9971233	-2.39	1.16	-2.50 ± 0.15	1.20 ± 0.15	-2.32 ± 0.21	1.15 ± 0.21	-1.81	2.18
	0.9969771	0.05	-0.03	0.28 ± 0.15	-0.01 ± 0.15	-0.08 ± 0.21	-0.01 ± 0.21	-1.64	-0.41
ψ_1	0.9945541	-0.14	0.07	-0.02 ± 0.15	0.16 ± 0.15	-0.07 ± 0.21	0.21 ± 0.21	-0.18	-0.01
ϕ_1	0.9918532	-0.27	0.11	-0.45 ± 0.15	0.07 ± 0.15	-0.68 ± 0.21	0.42 ± 0.21	-1.00	0.71
TT_1	0.9669565	-0.29	0.04	-0.08 ± 0.15	0.19 ± 0.15	-0.20 ± 0.21	0.05 ± 0.21	0.17	0.17
J_1	0.9624365	-1.61	0.19	-1.19 ± 0.14	0.79 ± 0.14	-1.02 ± 0.21	0.80 ± 0.21	-0.91	0.57
	0.9623003	-0.32	0.04	-0.05 ± 0.15	0.15 ± 0.15	-0.02 ± 0.21	-0.20 ± 0.21	-0.26	0.17
So_1	0.9341741	-0.41	-0.01	-0.09 ± 0.15	0.23 ± 0.15	0.10 ± 0.21	0.19 ± 0.21	-0.47	0.21
	0.9299547	-0.21	-0.01	-0.11 ± 0.15	-0.03 ± 0.15	-0.12 ± 0.21	0.19 ± 0.21	-0.07	-0.08
Oo_1	0.9294198	-1.44	-0.04	-0.64 ± 0.15	0.82 ± 0.15	-0.62 ± 0.21	0.48 ± 0.21	-0.91	0.39
	0.9292927	-0.92	-0.02	-0.68 ± 0.15	0.33 ± 0.15	-0.71 ± 0.21	0.53 ± 0.21	-0.72	0.69
	0.9291657	-0.19	-0.01	-0.18 ± 0.15	0.43 ± 0.15	-0.31 ± 0.21	0.16 ± 0.21	-0.33	0.22
ν_1	0.8990932	-0.40	-0.02	-0.24 ± 0.14	0.53 ± 0.14	-0.37 ± 0.21	0.56 ± 0.21	-0.23	0.72
	0.8989743	-0.25	-0.01	-0.07 ± 0.14	0.27 ± 0.14	-0.12 ± 0.21	0.31 ± 0.21	0.23	0.19

Table 8.9: Estimated amplitudes for k^{th} **semi-diurnal tide** of $\Delta UT1$ in μs.

Tide	Period	IERS2010		Least Squares		Singular Value Decomposition		Complex Demodulation	
	(days)	A''_k	B''_k	A''_k	B''_k	A''_k	B''_k	A''_k	B''_k
	0.5484264	-0.09	-0.01	0.03 ± 0.14	0.17 ± 0.14	0.05 ± 0.21	0.22 ± 0.21	0.33	0.38
	0.5469695	-0.22	-0.03	-0.03 ± 0.14	-0.01 ± 0.14	-0.23 ± 0.21	-0.28 ± 0.21	-0.35	-0.24
$2N_2$	0.5377239	-0.64	-0.18	-0.94 ± 0.15	-0.52 ± 0.15	-0.81 ± 0.21	-0.74 ± 0.21	-0.54	-0.28
μ_2	0.5363232	-0.74	-0.22	-0.56 ± 0.14	-1.00 ± 0.14	-0.66 ± 0.21	-1.05 ± 0.21	-0.88	-1.17
	0.5355369	-0.05	-0.01	-0.02 ± 0.14	0.06 ± 0.14	-0.21 ± 0.21	-0.04 ± 0.21	-0.10	-0.08
	0.5281939	0.03	0.01	0.00 ± 0.15	0.19 ± 0.15	-0.12 ± 0.21	0.01 ± 0.21	0.16	-0.25
	0.5274721	0.14	0.06	0.24 ± 0.15	0.01 ± 0.15	0.16 ± 0.21	0.26 ± 0.21	0.28	-0.25
N_2	0.5274312	-3.79	-1.56	-4.08 ± 0.14	-1.45 ± 0.14	-3.97 ± 0.21	-1.36 ± 0.21	-3.97	-1.19
	0.5266707	-0.04	-0.01	-0.18 ± 0.14	-0.10 ± 0.14	-0.43 ± 0.21	-0.35 ± 0.21	-0.56	-0.15
ν_2	0.5260835	-0.70	-0.30	-0.46 ± 0.15	-0.29 ± 0.15	-0.50 ± 0.21	-0.23 ± 0.21	-0.57	0.17
	0.5253269	-0.03	-0.01	-0.08 ± 0.15	-0.07 ± 0.14	-0.20 ± 0.21	-0.16 ± 0.21	-0.29	-0.25
	0.5188292	0.05	0.02	0.03 ± 0.15	-0.11 ± 0.15	-0.14 ± 0.21	0.05 ± 0.21	0.30	-0.42
	0.5182593	0.06	0.03	-0.26 ± 0.15	-0.29 ± 0.15	-0.27 ± 0.21	-0.42 ± 0.21	0.01	-1.08
	0.5175645	0.60	0.27	0.78 ± 0.15	0.16 ± 0.15	0.67 ± 0.21	0.35 ± 0.21	0.77	-0.42
M_2	0.5175251	-16.20	-7.14	-17.30 ± 0.14	-7.91 ± 0.14	-16.51 ± 0.21	-7.80 ± 0.21	-16.36	-7.83

Tide	Period (days)	IERS2010 A_k''	B_k''	Least Squares A_k''	B_k''	Singular Value Decomposition A_k''	B_k''	Complex Demodulation A_k''	B_k''
	0.5167928	-0.05	-0.02	0.42 ± 0.15	-0.05 ± 0.15	0.34 ± 0.21	0.22 ± 0.21	0.44	0.30
λ_2	0.5092406	0.11	0.03	0.17 ± 0.14	0.12 ± 0.15	0.19 ± 0.21	0.06 ± 0.21	0.25	0.03
L_2	0.5079842	0.42	0.12	0.35 ± 0.14	0.41 ± 0.14	0.41 ± 0.21	0.34 ± 0.21	0.54	0.14
	0.5078245	-0.11	-0.03	-0.15 ± 0.15	-0.02 ± 0.15	0.03 ± 0.21	-0.12 ± 0.21	0.06	-0.15
	0.5077866	-0.05	-0.01	0.02 ± 0.15	-0.07 ± 0.15	-0.10 ± 0.21	0.01 ± 0.21	-0.38	-0.14
T_2	0.5006854	-0.44	-0.02	-0.41 ± 0.15	0.03 ± 0.15	-0.49 ± 0.21	0.02 ± 0.21	-0.57	-0.25
S_2	0.5000000	-7.55	-0.16	-8.06 ± 0.14	-0.65 ± 0.15	-7.44 ± 0.21	-0.93 ± 0.21	-7.87	-0.99
R_2	0.4993165	0.06	0.00	-0.08 ± 0.15	-0.10 ± 0.15	-0.12 ± 0.21	0.33 ± 0.21	0.12	0.01
	0.4986714	0.03	-0.00	0.18 ± 0.15	0.11 ± 0.15	0.07 ± 0.21	0.13 ± 0.21	-0.20	-0.18
K_2	0.4986348	-2.10	0.04	-2.76 ± 0.15	-0.07 ± 0.15	-2.88 ± 0.21	-0.04 ± 0.21	-3.29	-0.38
	0.4985982	-0.63	0.01	-0.86 ± 0.15	0.14 ± 0.15	-1.03 ± 0.21	0.04 ± 0.21	-1.38	-0.14
	0.4985616	-0.07	0.00	0.12 ± 0.15	0.25 ± 0.15	-0.09 ± 0.21	0.32 ± 0.21	-0.33	-0.02
	0.4897717	-0.15	0.04	-0.14 ± 0.14	-0.16 ± 0.14	-0.11 ± 0.21	-0.12 ± 0.21	-0.30	-0.19
	0.4897365	-0.06	0.02	-0.08 ± 0.14	0.14 ± 0.14	0.10 ± 0.21	0.13 ± 0.21	0.19	0.37
	0.4810750	-0.05	0.02	0.16 ± 0.14	-0.04 ± 0.14	0.20 ± 0.21	-0.02 ± 0.21	-0.01	-0.17

8.5. Comparisons of Tidal Amplitude Estimates from Standard VLBI Sessions

It is difficult to determine how accurate the estimated amplitudes are. In fact, estimation errors of any amplitude may not represent its contribution to modeling the ocean tides caused ERP variations. Hence, we investigated the agreement of the estimated amplitudes using the metrics of time series, Fourier transforms, and phasor plots. For these evaluations, we calculated the time series of x_p, y_p and $\Delta UT1$ at $1 - hour$ intervals through using the estimated amplitudes from least squares, singular value decomposition, and complex demodulation solutions as well as IERS2010 model covering the time period between the beginning of 2000 and the end of 2018. The mean values of the difference vectors between our estimates and those of IERS model are zero for six difference vector combinations. Agreement of two time series can be deduced from the standard deviations of the difference vectors that are shown in Figure (8.5). The most agreed series are those derived from complex demodulation and singular value decomposition for x_p and y_p, and for $\Delta UT1$. Least squares and singular value decomposition shows the best agreement. The most different series are derived from complex demodulation and the IERS2010 model for all ERP. Strictly speaking, agreement of time series is not a criteria for the accuracy of the estimates.
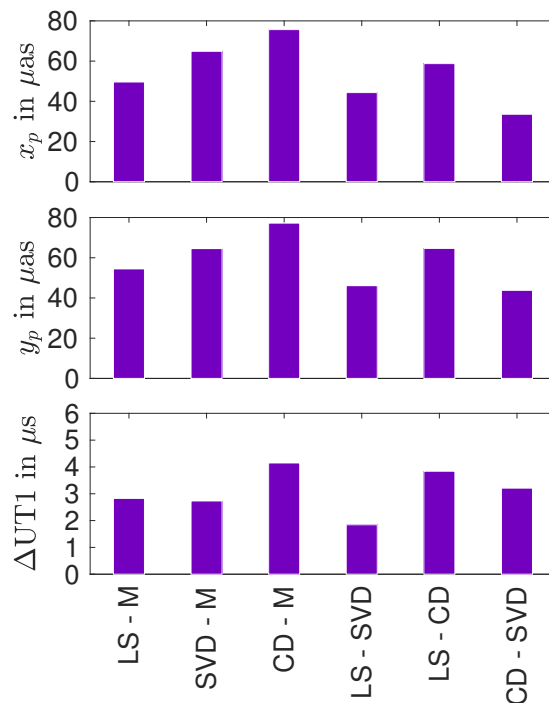

Figure 8.5: Comparisons of the hourly ERP series derived from the IERS2010 model (M), least squares (LS), singular value decomposition (SVD), and complex demodulation (CD) during 2000-2018 based on the metric of standard deviations of the series differences.

The time series are shown in Figure (8.6) for first $60 - days$ of the 2010 year, and also Figure (8.7) shows that the time series derived from estimated amplitudes with respect to the IERS2010 model. Although, a few model amplitudes which might not be correct for some tides (e.g. S_1 and adjacent tide), time series calculated from the estimated models agree well to those of IERS model. That may demonstrate that our estimates would enhance sub-daily ERP variations model.

Figure (8.8) shows phasor plots of major (principle) tides. Phasor plots were drawn for each of the major tides estimated by the solutions of least square, singular value decomposition and complex demodulation besides those predictions of IERS2010 model. The phasor plots were obtained from the coefficients of polar motion coordinates $(x_p - iy_p)$ by an expansion of Euler formulae as follows,

$$P_k^{cos} + iP_k^{sin} = (-B_k + A_k' + iA_k + iB_k')/2$$

$$R_k^{cos} + iR_k^{sin} = (-B_k - A_k' - iA_k + iB_k')/2$$

(8.7)

where, A_k, B_k, A_k', and B_k', given in Tables (8.4, 8.5, 8.6, and 8.7), are coefficients of kth tide for x_p and y_p, respectively. P_k^{cos}, P_k^{sin}, R_k^{cos}, and R_k^{sin} are cosine and sine coefficients of prograde (P) and retrograde (R) motions for k^{th} tide, respectively. i denotes unit imaginary number $i = \sqrt{-1}$. Its seen that P_1 and Q_1 tides have similar amplitudes for all methods, and O_1 and K_1 are well-matched for SVD and CD methods in diurnal prograde motion. But, it should be noted that O_1 and K_1 have larger amplitudes than Q_1 and P_1. Since the diurnal tides do not excite retrograde polar motion, it is not shown in phasor plots. Semi-diurnal tides induce prograde polar motion as well as retrograde. While N_2 and S_2 have alikeness among all techniques in prograde motion, N_2 and K_2 are matching with the IERS2010 model. One more comparison for phasor plots was done with the differences of least squares, singular value decomposition and complex demodulation from the IERS2010 model as shown in Figure (8.9). The least squares technique estimated amplitudes of major tides closest to the IERS2010 model, and complex demodulation estimates most deviated from the model. These deviations are in the order of $10 - 20\mu as$, $5 - 10\mu as$, and $10 - 50\mu as$ for diurnal prograde, semi-diurnal prograde, and semi-diurnal retrograde motions, respectively. If estimated amplitudes are considered, M_2 and its adjacent tide (with period of 0.5175645 cpsd) may not be estimated properly due to their high correlation. Our estimates for this adjacent tides are about two times larger to those of IERS2010 model for polar motion coordinates.

We could plot the Fourier transform for the duration 2000-2018 because our time series derived from the estimated amplitudes are evenly distributed. Figure (8.10) and (8.11) show Fourier transforms of time series derived from estimated amplitudes by three methods with respect to the IERS2010 model for polar motion coordinates $(x_p - iy_p)$ and $\Delta UT1$, re-

spectively. Although, diurnal tides of x_p and y_p are canceled out each other for retrograde motion (e.g. $A_k = B_k'$, and $B_k = -A_k'$ for diurnal tides), in these plots, all three techniques estimated the diurnal retrograde motion as about $10 - 20 \, \mu as$. We set free the estimated amplitudes without any constraint, and estimation of amplitudes for x_p and y_p were performed separately, although this motion is composed by both polar motion components. The Fourier transform plots of $\Delta UT1$ are also given for three methods. The peak differences are less than $1\mu s$ for all methods, and SVD shows the best agreement with the IERS2010 model.

Besides, Figure (8.12) shows Fourier transform of the same difference vectors focused to diurnal prograde, semi-diurnal prograde and semi-diurnal retrograde tides for polar motion coordinates ($x_p - iy_p$), respectively.

Complex demodulation estimates of K_1 and P_1 are the most diverged ones from the model in diurnal motion about $20 - 25 \, \mu as$. Although, prograde motion of K_2 and M_2 estimates from complex demodulation solution are the highest peaks ($8 - 10 \, \mu as$), in retrograde part, K_2 difference is the smallest with respect to the IERS model.

The more focused plots of $\Delta UT1$ are given in Figure (8.13). Even if the differences are of K_1 and O_1 are low for LS and SVD methods, they have the highest peaks for CD method in diurnal tides. Similarly, in semi-diurnal tides K_2 and S_2 differences are highest for CD, whereas, M_2 has large difference w.r.t. IERS model for LS method.
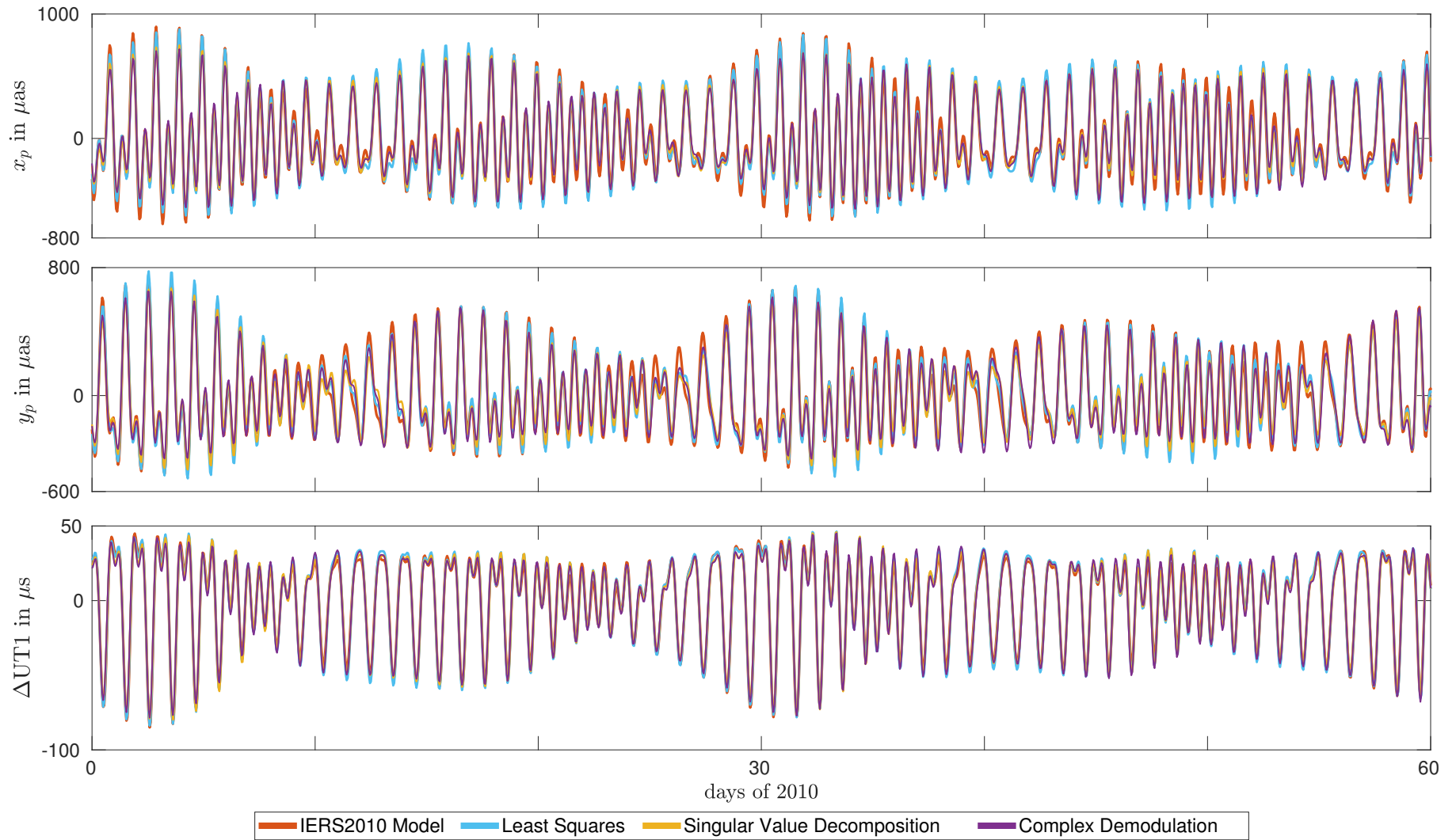
Figure 8.6: Hourly time series of x_p, y_p in μas and ΔUT1 in μs calculated using the IERS2010 model and the models estimated from least squares, singular value decomposition, and complex demodulation over a duration of two months.
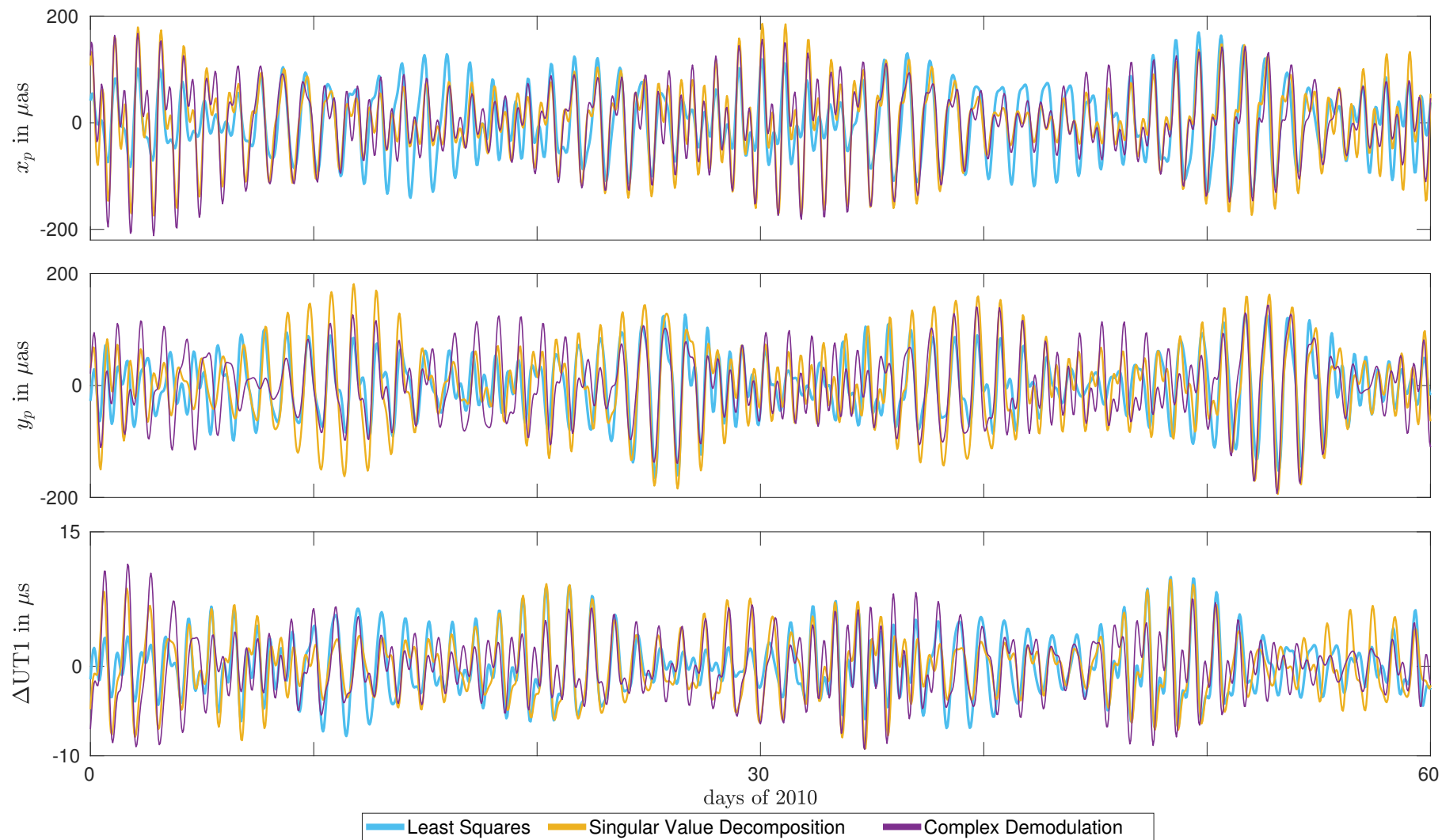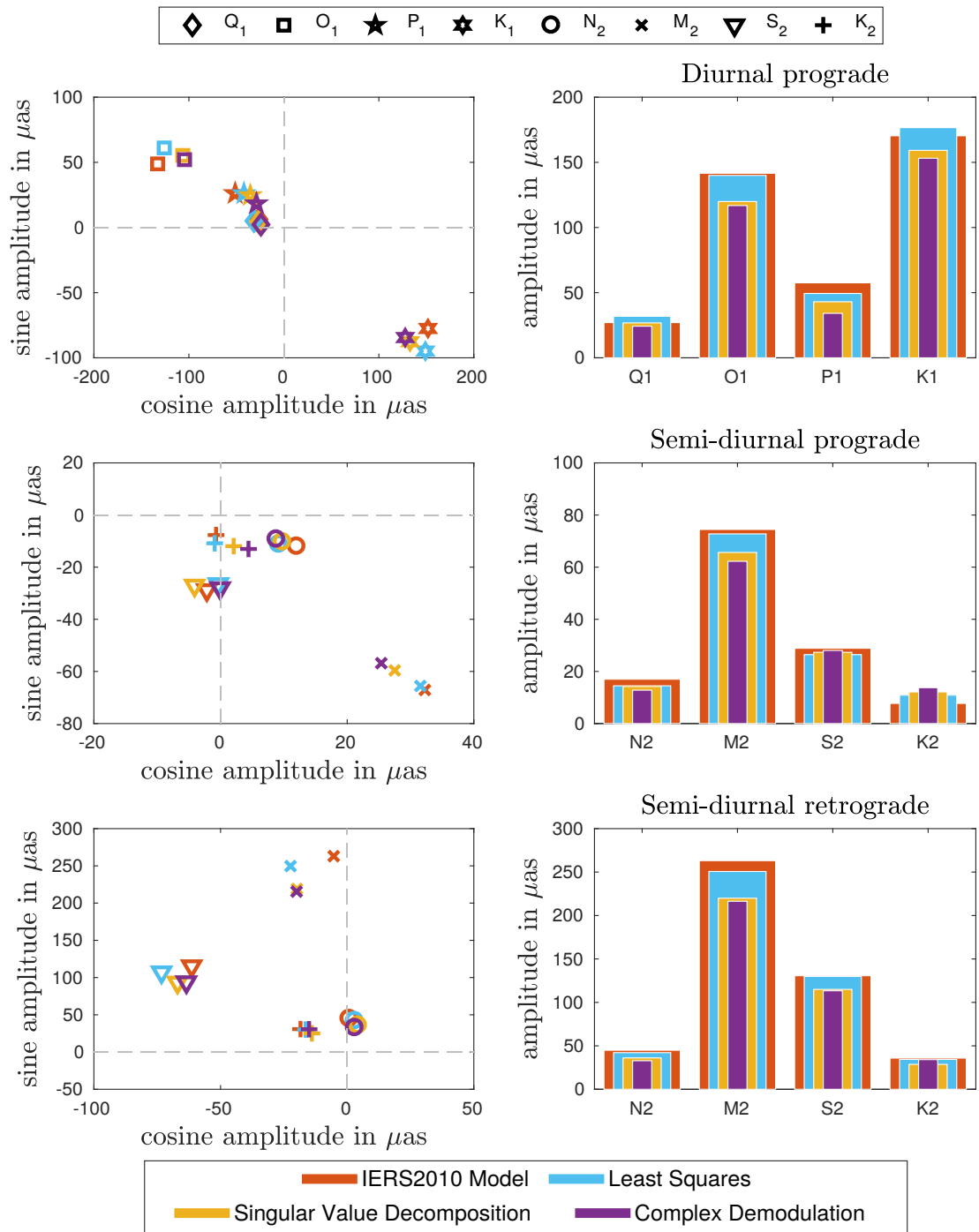
Figure 8.7: Hourly time series of x_p, y_p in μas and ΔUT1 in μs calculated using the models estimated from least squares, singular value decomposition, and complex demodulation **with respect to the IERS2010 model** over a duration of two months.

Figure 8.8: Phasor plots of the major tides estimated from VLBI observations between 2000-2018: Diurnal prograde (upper-left plot), semi-diurnal prograde (middle-left plot), semi-diurnal retrograde (lower-left plot), and the modulus of the diurnal prograde, semi-diurnal prograde and semi-diurnal retrograde phasor vectors are shown in upper-right, middle-right and lower-right plots, respectively.
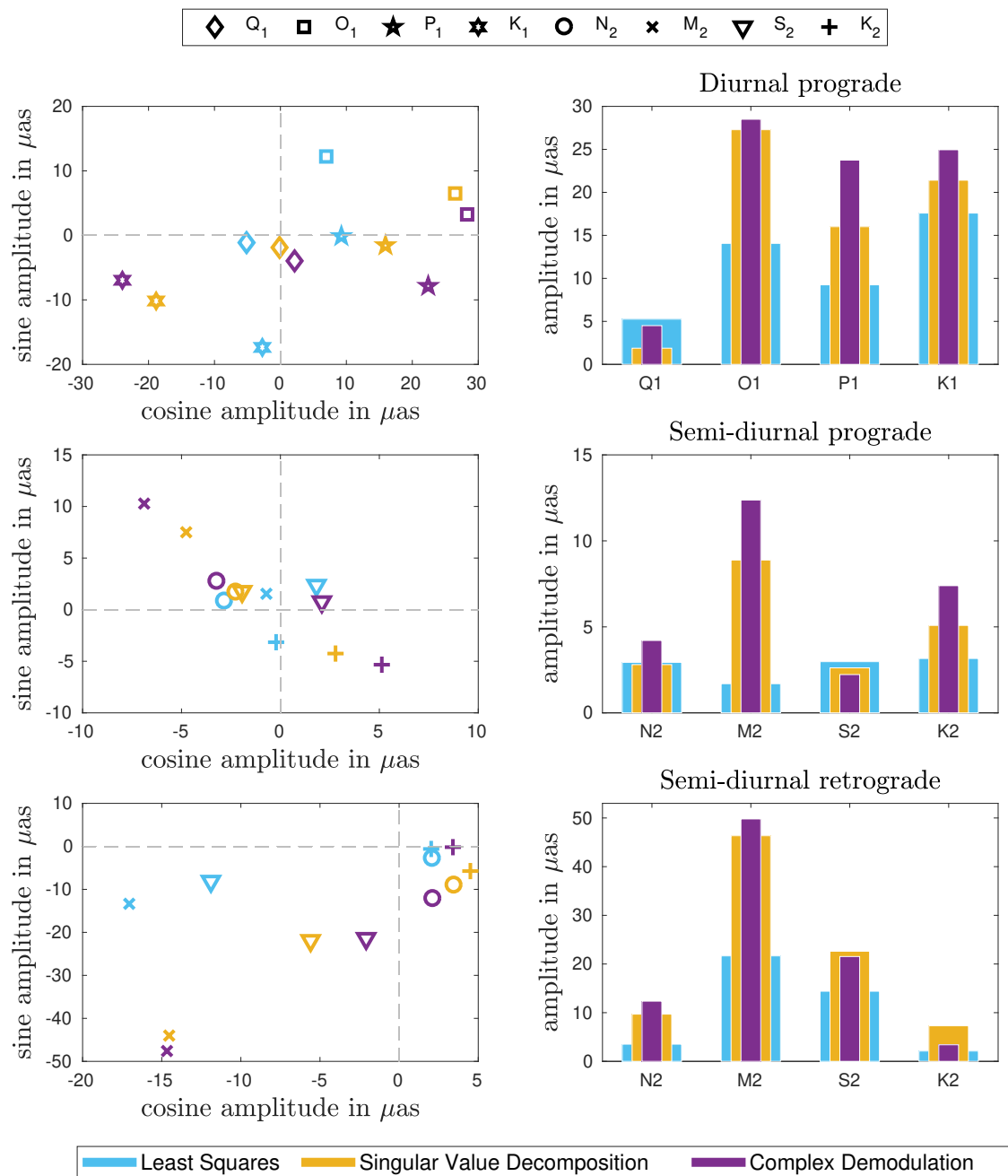
Figure 8.9: Phasor plots of the major tides estimated from VLBI observations **with respect to the IERS2010 model** between 2000-2018: Diurnal prograde (upper-left plot), semi-diurnal prograde (middle-left plot), semi-diurnal retrograde (lower-left plot), and modulus of the diurnal prograde, semi-diurnal prograde and semi-diurnal retrograde are shown in upper-right, middle-right and lower-right plots, respectively.
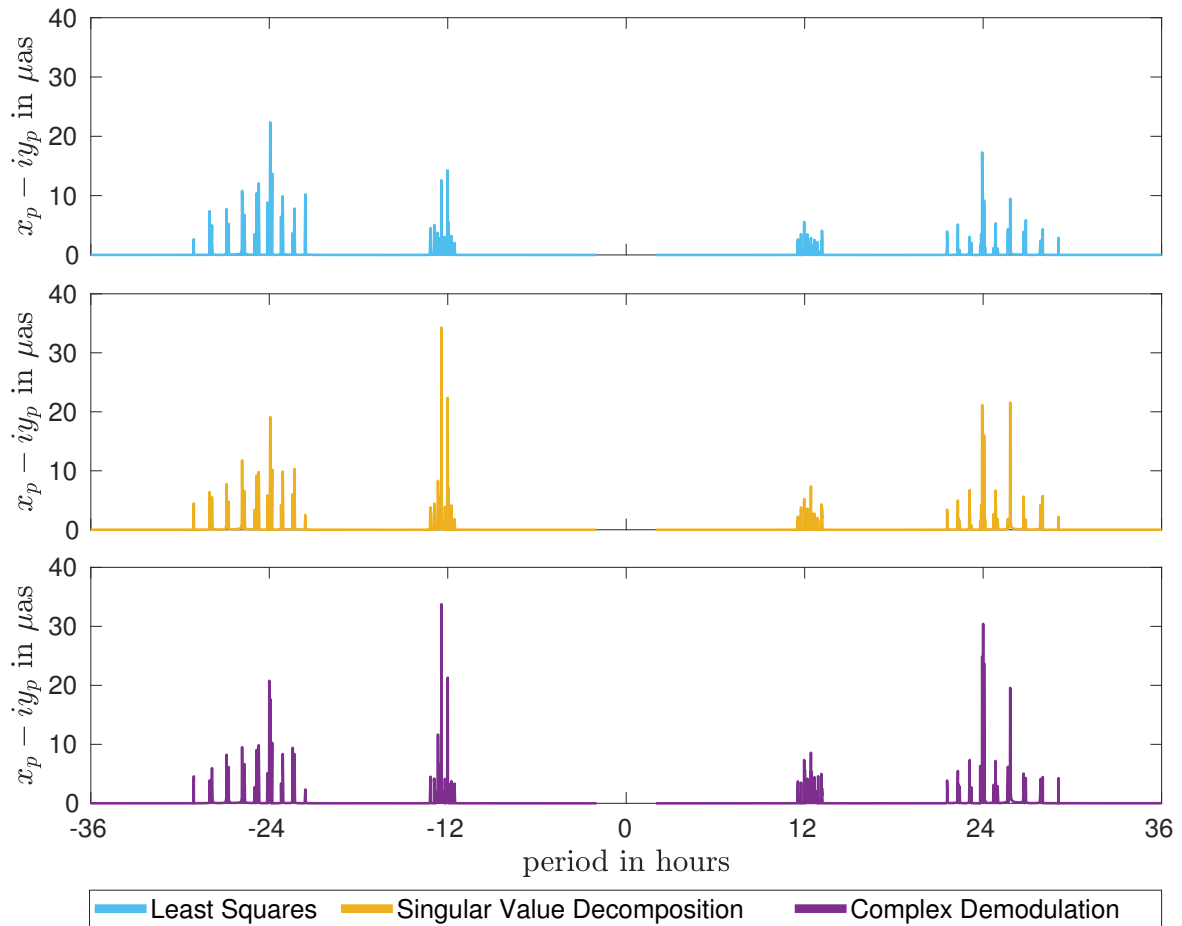
Figure 8.10: Fourier transforms of the hourly $x_p - iy_p$ time series between 2000-2018 derived from estimated amplitudes using least squares, singular value decomposition and complex demodulation **with respect to the IERS2010 model**.
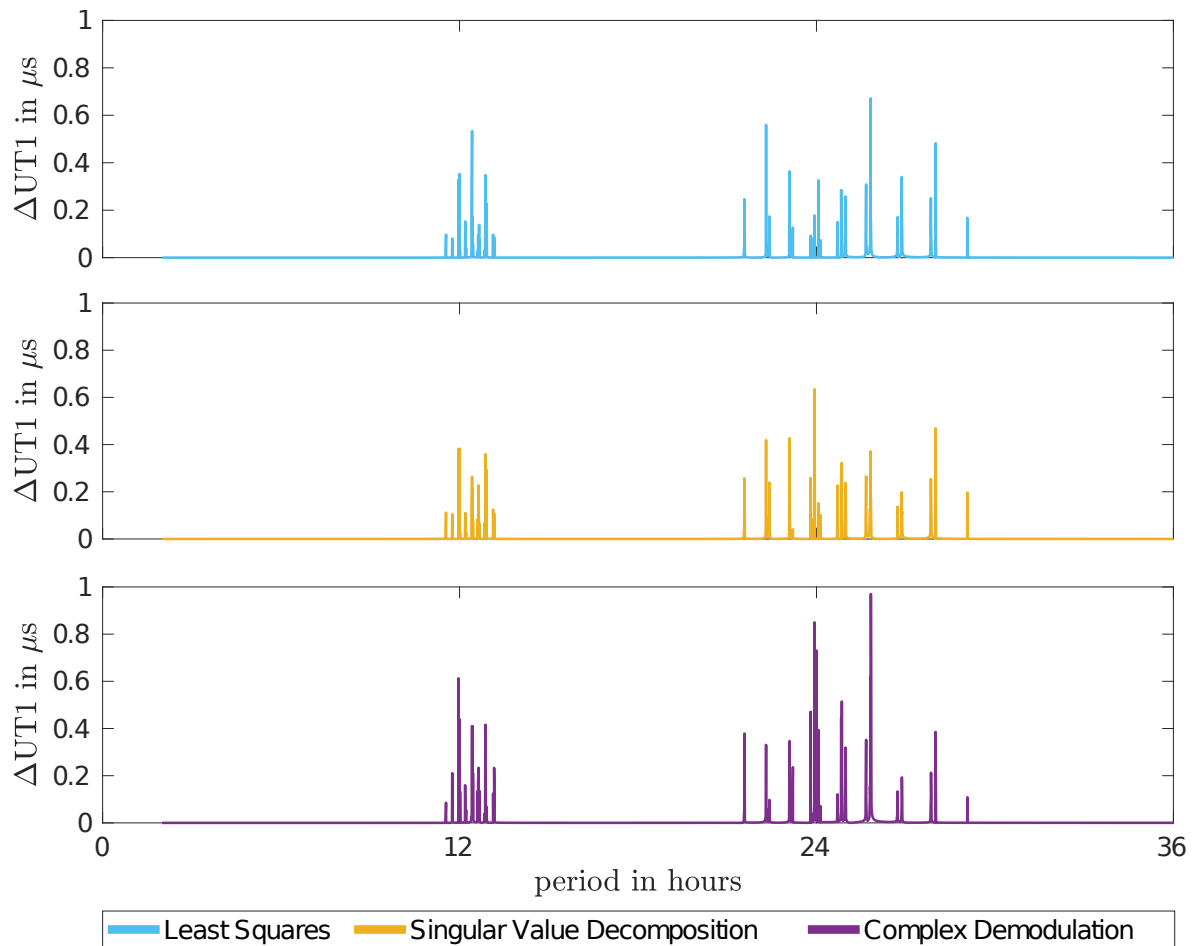
Figure 8.11: Fourier transforms of the hourly ΔUT1 time series between 2000-2018 derived from the estimated amplitudes using least squares, singular value decomposition and complex demodulation **with respect to the IERS2010 model**.
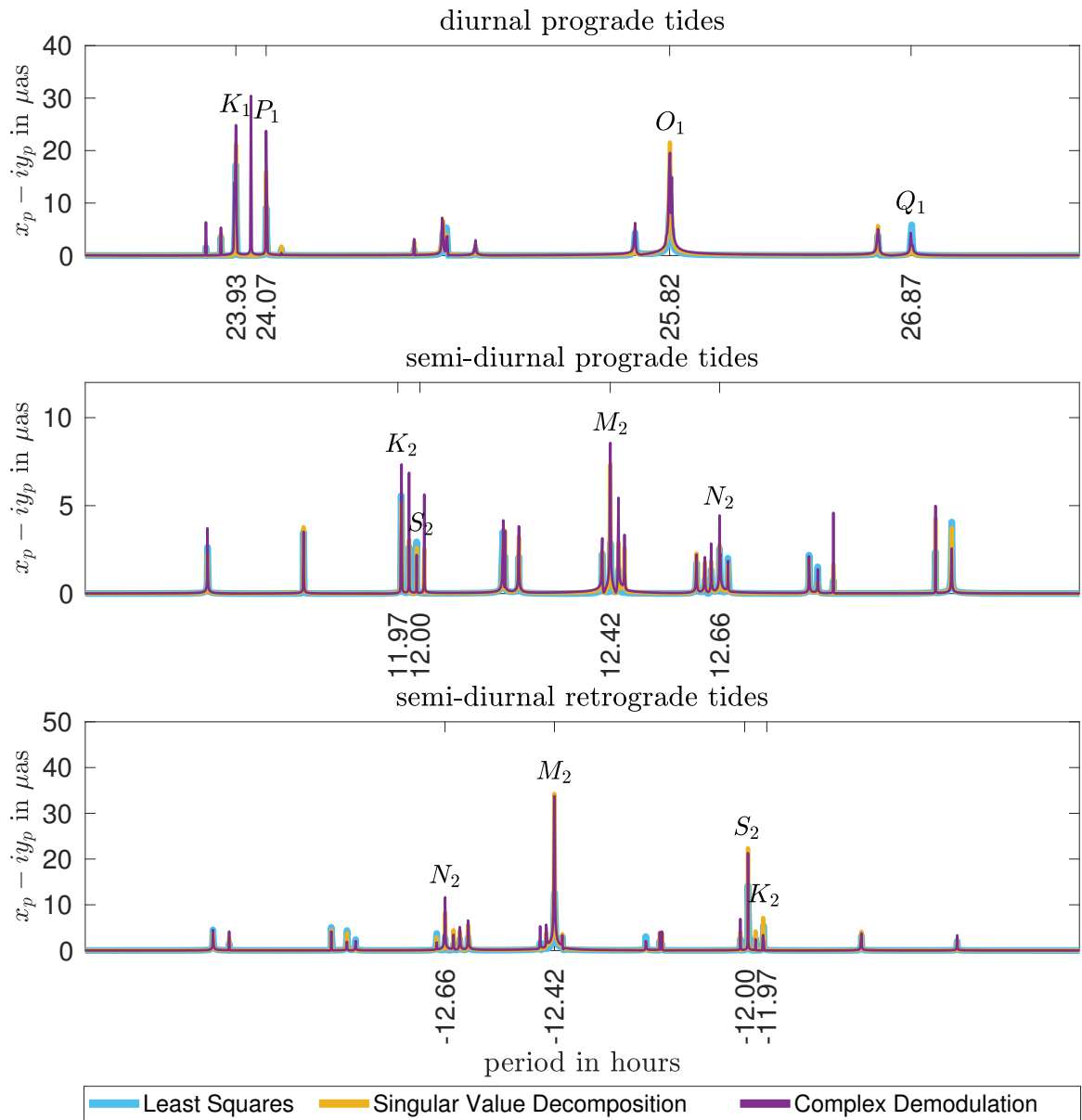
Figure 8.12: Diurnal prograde (upper), semi-diurnal prograde (middle) and semi-diurnal retrograde (lower) plots of Fourier transforms of the hourly $x_p - iy_p$ time series between 2000-2018 derived from estimated amplitudes using least squares, singular value decomposition and complex demodulation **with respect to the IERS2010 model**.

Figure 8.13: Diurnal (upper), semi-diurnal (lower) plots of Fourier transforms of the hourly ΔUT1 time series between 2000-2018 derived from the estimated amplitudes using least squares, singular value decomposition and complex demodulation **with respect to the IERS2010 model**.
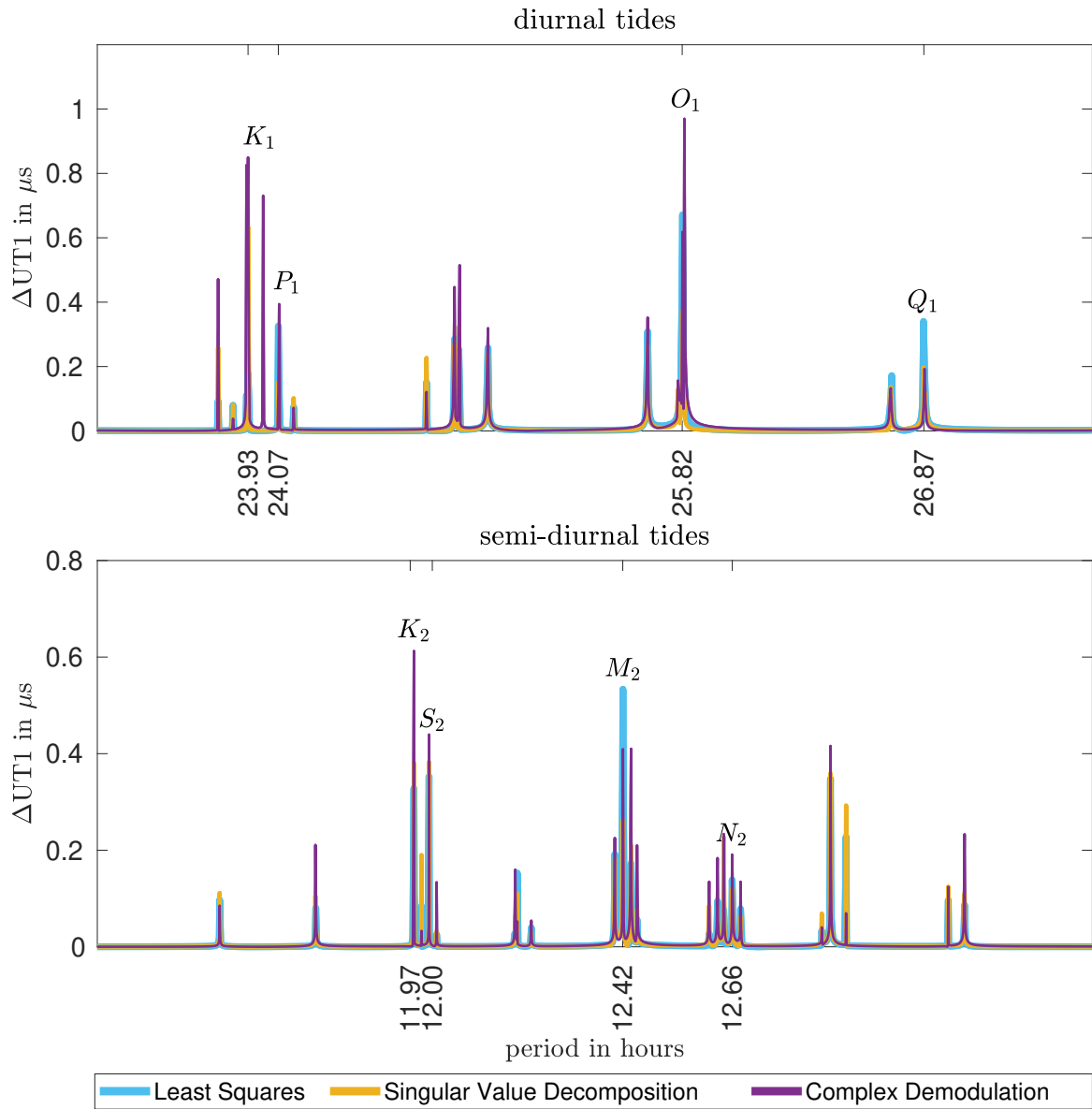
9. CONCLUSIONS AND RECOMMENDATIONS

The accurate estimation of EOP has a significant contribution to space, atmosphere and Earth sciences. These parameters are monitored with several space/satellite geodetic techniques i.e. GNSS, DORIS, SLR/LLR, and VLBI, and concerning products are provided to IERS. This thesis covers monitoring ERP with VLBI observations. The works established in this thesis are actually two distinct parts. It is better to interpret the conclusion and recommendations for each of the following research objectives:

- Accuracy improvement of UT1 monitored by VLBI Intensive sessions (see Chapter 7),

- Estimating a replacement of IERS recommended model for sub-daily ERP variations caused by ocean tides from the analyses of VLBI Standard sessions (see Chapter 8).

9.1. Conclusions

• Conclusions from accuracy improvement of UT1 monitored by VLBI Intensive sessions

The most rapidly changing parameter among the ERP is UT1, that can be monitored by VLBI space geodetic technique only. The VLBI sessions performed for UT1 determination purposes is called as Intensive. In the standard analysis of the VLBI sessions proposed by IVS, whose UT1 estimates are named as StandardUT1(A1) in this thesis, troposphere signal delays in proper time resolution and troposphere gradients are not involved in the estimation process due to the lack of observations of this sessions.

In this study, the troposphere delays obtained from the observations of the GNSS receivers co-located with VLBI stations by IGS were used in the analysis of the VLBI Intensives with two different analyses called as NewUT1(A2) and NewUT2(A3). The length-of-day (LOD) values were calculated from StandardUT1(A1), NewUT1(A2) and NewUT1(A3). These LOD values were compared with LOD time series of IGS analysis centers using WRMS of differences. LOD series derived from NewUT1(A2) and NewUT1(A3) are $2 - 3\ \mu s/day$ close to LOD values of IGS analysis centers compared to LOD obtained from StandardUT1(A1). Thus, more accurate estimates of UT1 compared to IVS standard analysis were produced. Considering the accuracy of UT1 determination from IVS Standard sessions (24-hours) is about $1 - 2\ \mu s$, advances in the accuracy of LOD at a level of $2 - 3\ \mu s/day$ would

be a meaningful contribution.

As a product of this thesis, VLBI research group at Hacettepe University has gained the ability of automatic processes of GNSS as well as VLBI observations. Two workstation computers equipped with highly skilled hardware were dedicated to GNSS and VLBI processes, separately. Besides, a network-attached storage (NAS) device was established online as a repository of analysis outputs of space/satellite geodetic techniques and observation files. The last output for this part of the thesis is setting web service for publishing UT1 results to the community of Earth and space sciences. This web service is being updated regularly, daily and automatically after the results of UT1 is acquired at the web page `http://vlbi.hacettepe.edu.tr/en/menu/tubitak_3501_115y244-20`

● **Conclusions for estimating a replacement of IERS recommended model for sub-daily ERP variations caused by ocean tides from the analyses of VLBI Standard sessions**

The principal reason for ERP variations at sub-daily periods is ocean tides. The IERS model with 71 sub-daily tidal constituents for prediction of this effect (Ray et al., 1994) can be assumed as out-of-date. During the least square adjustment of the observations, due to the usage of Taylor expansion of the non-linear observation model to get linearized form, a priori values of any parameter should be as close as possible to the exact (expected) values for better adjustment. Thus, it is declared by IAG that a model for sub-daily ERP variations due to ocean tides should be developed with modern geodetic techniques for accuracy improvement. Chapter (8) is dedicated to the estimation of a new model as an alternative of the IERS model by examining the performances of several sinusoidal amplitude estimation methods such as least squares (LS), singular value decomposition (SVD), and complex demodulation (CD). Sinusoidal amplitude estimation methods are not a key factor only. In fact, the precise estimation of the time series of ERP from space/satellite geodetic techniques has an impact on this objective beyond the effect of the sinusoidal amplitude estimation methods. However, each method has its own pros and cons.

In order to achieve time series of ERP (x_p, y_p, and $\Delta UT1$), VLBI Standard sessions ($24 - hours$) between 2000 and 2018 observed with at least 6 VLBI stations were analyzed. The sessions with $chi^2 > 4$ and $wrms > 2$ (weighted root-mean-square error) were not included in the analysis. Nonetheless, outlier observations were removed before the time series were estimated.

After time series of ERP were obtained, sinusoidal amplitude estimation methods were applied for each of the ERP, separately. Sine and cosine amplitudes of each of 71 tidal constituents for each of x_p, y_p, and $\Delta UT1$ parameters were derived using LS, SVD and CD methods. LS and SVD methods are based on a simultaneous estimation of all amplitudes

of all constituents. However, the CD method is operated for each of tidal constituents, individually. For this reason, any estimation errors at periods of particular tides would easily propagate to the results of other tides in LS and SVD methods. On the other hand, estimation with CD is restricting the propagation of the error of the certain tides to the others. LS results are found to be more consistent with IERS model. However, strictly speaking, it is not a measure of the accuracy of estimation that being close to the IERS model. A few tides estimated with LS and SVD have very high amplitudes compared to those of IERS2010 model. Besides, in general it could be inferred that the results of LS and SVD methods are in a good agreement.

Excepting sinusoidal amplitude estimation methods, there is one more criterion in the modeling of such variations that is spectral distances of adjacent tides. Rayleigh criterion (Foreman, 1977) for discrimination of two adjacent peaks states that $\Delta f = |f_1 - f_2| = 1/T$ is enough for "just" resolved peaks. Here, f_1 and f_2 denote frequencies of neighboring peaks, and T is the duration of the time series. This criterion becomes $\Delta f = 3/2T$ for "well" resolved peaks. In our particular observation period of $18 - years$, the maximum allowed spectral spacing between two adjacent peaks is $0.00022 - cycle/sidereal\ day$ for well-resolved peaks. That means separation of S_1 tide from its neighbor requires 7500000 days of observation which is neither possible nor logical. As a consequence, de-correlation of these adjacent tides is not probable with the approach of this thesis and any other quantitative approach. Moreover, the propagation of tidal amplitudes into other tides may not be prevented due to the Rayleigh criterion.

9.2. Recommendations

For the objective of UT1 accuracy improvement, followings are suggested for further studies:

- So as to test the limits of UT1 determination accuracy of VLBI Intensive sessions when using external troposphere delays and gradients, different analysis parametrizations of GNSS PPP estimation should be tried. However, usage of troposphere delays and gradients shared by IGS are limiting the mobility of the estimation paradigm. Thus, the derivation of the troposphere products should be executed using a GNSS analysis software by employing different combinations of such parameters: e.g. troposphere mapping functions, troposphere models, a priori hydrostatic delays.

- Bernese software (Dach et al., 2015) is one of the cutting edge GNSS analysis software. However, its computation power reveals when the double-difference solution is carried out with observations of the hundreds of stations. In order for PPP solution,

several basic subroutines, that may provide the estimation of troposphere spending less effort, should be written. This also ensures keeping all estimation procedure under the control.

- Analysis of the GNSS observations in order to derive troposphere is limited to the observations of the GPS and GLONASS for this study. In fact, taking the observations of the other GNSS i.e. Galileo and BeiDou, that will gain global coverage by 2020, would increase the estimation accuracy of the troposphere as well as UT1.

- The automatization of the procedure till the publishing at the Web site is executed in Linux shell scripts, and the troposphere estimation related algorithms were written in MATLAB environment. Although Linux shell scripts are running in parallel, subroutines written in MATLAB are designed to work on a core of processor only. This is a time-consuming process increasing the computation burden of a single central processing unit (CPU). It is better to convert existing software from MATLAB into faster programming languages like C/C++ or Python using parallel and the graphical processing unit (GPU) programming. Although, this suggestion will not affect the estimation accuracy, it would enable to try various strategies in less time. Thus, it will eventually contribute to accuracy in an indirect way.

For the modeling of the sub-daily ERP variations due to ocean tides, the forthcoming studies should consider the following remarks:

- The time interval for the VLBI analysis was chosen between 2000-2018. In fact, expanding this time interval from the beginning of the VLBI observations to the present would be beneficial providing the earlier VLBI sessions should be analyzed more carefully.

- It is exhibited by Rothacher et al. (1999) and Malkin (2009) that GNSS technique is able to estimate more accurate polar motion coordinates than VLBI. Besides, other space/satellite techniques such as DORIS and SLR/LLR are also able to estimate these parameters. Then, only the amplitudes of the model belong to the polar motion coordinates may be estimated from an inter-technique combination of these techniques.

- The principal and only technique of determination of UT1 is VLBI. But, in order to expand the duration as well as the number of sessions in this interval, VLBI Intensive sessions alongside Standard sessions should be analyzed for estimation of model amplitudes for only UT1.

- The other parameter estimation methods that are usable for sinusoidal amplitude estimation such as recursive least squares, Kalman filter, Discrete Fourier transform, and

artificial neural networks should be utilized for the estimation of the tidal amplitudes of the model. As epochs of the time series increases, the volume of variables (e.g. weight matrix of LS method) at the random access memory (RAM) of computer is strikingly increasing. For this reason, batch processing techniques are struggling with computer resource management. It is better to use sequential methods to overcome this issue.

- For evaluation of the acquired model for sub-daily ERP variations, baseline length repeatability should be an objective criteria (metric) instead of comparing them with the IERS recommended model.

- A robust method for de-correlating polar motion coordinates from nutation offsets should be investigated. Because, estimation of nutation offset is not possible due to its high correlation with polar motion in sub-daily periods.

REFERENCES

Abramowitz, M., Stegun, I.A. (Eds.), Handbook of mathematical functions: with formulas, graphs, and mathematical tables, 9. dover print.; [nachdr. der ausg. von 1972] ed., Dover books on mathematics, Dover Publ, New York, USA, **2013**, ISBN 978-0-486-61272-0.

Altamimi, Z., Collilieux, X., Legrand, J., Garayt, B., Boucher, C., ITRF2005: A new release of the International Terrestrial Reference Frame based on time series of station positions and Earth Orientation Parameters, Journal of Geophysical Research, Vol. 112 (**2007**) B9 B09401, doi:10.1029/2007JB004949.

Altamimi, Z., Collilieux, X., Métivier, L., ITRF2008: an improved solution of the international terrestrial reference frame, Journal of Geodesy, Vol. 85 (**2011**) 8 457–473, doi:10.1007/s00190-011-0444-4.

Altamimi, Z., Rebischung, P., Métivier, L., Collilieux, X., ITRF2014: A new release of the International Terrestrial Reference Frame modeling nonlinear station motions, Journal of Geophysical Research: Solid Earth, Vol. 121 (**2016**) 8 6109–6131, doi:10.1002/2016jb013098.

Alter, O., Brown, P.O., Botstein, D., Singular value decomposition for genome-wide expression data processing and modeling, Proceedings of the National Academy of Sciences, Vol. 97 (**2000**) 18 10101–10106, doi:10.1073/pnas.97.18.10101.

Artz, T., Böckmann, S., Nothnagel, A., Steigenberger, P., Subdiurnal variations in the Earth's rotation from continuous Very Long Baseline Interferometry campaigns, Journal of Geophysical Research, Vol. 115 (**2010**) B5, doi:10.1029/2009JB006834.

Artz, T., Tesmer née Böckmann, S., Nothnagel, A., Assessment of periodic sub-diurnal Earth rotation variations at tidal frequencies through transformation of VLBI normal equation systems, Journal of Geodesy, Vol. 85 (**2011**) 9 565–584, doi:10.1007/s00190-011-0457-z.

Ashby, N., Relativity in the Global Positioning System, Living Reviews in Relativity, Vol. 6 (**2003**) 1, doi:10.12942/lrr-2003-1.

Ávila Rodríguez, J.A., On Generalized Signal Waveforms for Satellite Navigation, Ph.D. thesis, University FAF Munich, Faculty of Aerospace Engineering, Munich, Germany, **2008**.

Bar-Sever, Y.E., Kroger, P.M., Borjesson, J.A., Estimating horizontal gradients of tropospheric path delay with a single GPS receiver, Journal of Geophysical Research: Solid Earth, Vol. 103 (**1998**) B3 5019–5035, doi:10.1029/97JB03534.

Baueršíma, I., NAVSTAR/Global Positioning System (GPS) (I)., Mitteilungen der Satelliten Beobachtungsstation Zimmerwald, Astronomical Institute, University of Bern, Vol. 7 (**1982**).

Bizouard, C., Lambert, S., Gattano, C., Becker, O., Richard, J.Y., The IERS EOP 14C04 solution for Earth orientation parameters consistent with ITRF 2014, Journal of Geodesy, (**2018**), doi:10.1007/s00190-018-1186-3.

Bleaney, B.I., Bleaney, B., Electricity and magnetism, 3rd revised ed., Oxford Univ. Press, Oxford, England, **1978**, ISBN 978-0-19-851140-3.

Bloomfield, P., Fourier analysis of time series: an introduction, 2nd ed., Wiley series in probability and statistics. Applied probability and statistics section, Wiley, New York, USA, **2000**, ISBN 0-471-88948-2.

Born, M., Wolf, E., Principles of Optics, 5th ed., Pergamon Press, New York, USA, **1975**.

Borre, K., Akos, D.M., Bertelsen, N., Rinder, P., Jensen, S.H., A Software-Defined GPS and Galileo Receiver, Applied and Numerical Harmonic Analysis, Birkhäuser, Boston, Massachusetts, USA, **2007**, ISBN 978-0-8176-4390-4, doi:10.1007/978-0-8176-4540-3.

Brockmann, E., Combination of solutions for geodetic and geodynamic applications of the Global Positioning System (GPS), Tech. Rep. 55, Geodätisch Geophysikalische Arbeiten in der Schweiz, Schweizerische Geodätische Kommission, **1997**.

Brzeziński, A., On estimation of high frequency geophysical signals in Earth rotation by complex demodulation, Journal of Geodynamics, Vol. 62 (**2012**) 74–82, doi:10.1016/j.jog.2012.01.008.

Brzeziński, A., Böhm, S., Analysis of the high frequency components of Earth rotation demodulated from VLBI data, in H. Schuh, S. Böhm, T. Nilsson, N. Capitaine (Eds.), Earth rotation, reference systems, and celestial mechanics: synergies of geodesy and astronomy ; Journées 2011 Systèmes de référence spatio-temporels, 19-21 September 2011, Vienna, **2012**, ISBN 978-2-901057-67-3 pp. 132–135.

Byram, S., Hackman, C., Tracey, C., Computation of a High-Precision GPS-Based Troposphere Product by the USNO, in 24th International Technical Meeting of the Satellite Division of the Institute of Navigation Proceedings, **2011** pp. 572–578.

Byun, S.H., Bar-Sever, Y.E., A new type of troposphere zenith path delay product of the international GNSS service, Journal of Geodesy, Vol. 83 (**2009**) 3-4 1–7, doi:10.1007/s00190-008-0288-8.

Böhm, J., Böhm, S., Boisits, J., Girdiuk, A., Gruber, J., Hellerschmied, A., Krásná, H., Landskron, D., Madzak, M., Mayer, D., McCallum, J., McCallum, L., Schartner, M., Teke, K., Vienna VLBI and Satellite Software (VieVS) for Geodesy and Astrometry, Publications of the Astronomical Society of the Pacific, Vol. 130 (**2018**) 986 044503, doi:10.1088/1538-3873/aaa22b.

Böhm, J., Böhm, S., Nilsson, T., Pany, A., Plank, L., Spicakova, H., Teke, K., Schuh, H., The New Vienna VLBI Software VieVS, Proceedings of the 2009 IAG Symposium, in S. Kenyon, M.C. Pacino, U. Marti (Eds.), Geodesy for Planet Earth, Vol. 136, Springer Berlin Heidelberg, Berlin, Germany, **2012**, ISBN 978-3-642-20337-4 pp. 1007–1011, doi:10.1007/978-3-642-20338-1_126.

Böhm, J., Möller, G., Schindelegger, M., Pain, G., Weber, R., Development of an improved empirical model for slant delays in the troposphere (GPT2w), GPS Solutions, Vol. 19 (**2015**) 3 433–441, doi:10.1007/s10291-014-0403-7.

Böhm, J., Niell, A., Tregoning, P., Schuh, H., Global Mapping Function (GMF): A new empirical mapping function based on numerical weather model data, Geophysical Research Letters, Vol. 33 (**2006**) 7, doi:10.1029/2005GL025546.

Böhm, J., Schuh, H., Vienna mapping functions in VLBI analyses, Geophysical Research Letters, Vol. 31 (**2004**) 1, doi:10.1029/2003GL018984.

Böhm, J., Schuh, H. (Eds.), Atmospheric Effects in Space Geodesy, Springer Atmospheric Sciences, Springer Berlin Heidelberg, Berlin, Germany, **2013**, ISBN 978-3-642-36931-5, doi:10.1007/978-3-642-36932-2.

Böhm, J., Werl, B., Schuh, H., Troposphere mapping functions for GPS and Very Long Baseline Interferometry from European Center for Medium-Range Weather Forecasts operational analysis data, Journal of Geophysical Research, Vol. 111 (**2006**) B02406.

Böhm, S., Brzeziński, A., Schuh, H., Complex demodulation in VLBI estimation of high frequency Earth rotation components, Journal of Geodynamics, Vol. 62 (**2012**) 56–68, doi:10.1016/j.jog.2011.10.002.

Campbell, J., From Quasar to Benchmarks: VLBI Links Heaven and Earth, in N. Vandenberg, K. Baver (Eds.), International VLBI Service for Geodesy and Astrometry, no. NASA/CP-2000-209893 in General Meeting Proceedings, **2000** pp. 19–34.

Capitaine, N., Guinot, B., McCarthy, D., Definition of the Celestial Ephemeris origin and of UT1 in the International Celestial Reference Frame, Astronomy &

Astrophysics, Vol. 335 (**2000**) 1 398–405.

Capitaine, N., Guinot, B., Souchay, J., A Non-rotating Origin on the Instantaneous Equator: Definition, Properties and Use, Celestial Mechanics, Vol. 39 (**1986**) 3 283–307.

Capitaine, N., Wallace, P.T., Chapront, J., Expressions for IAU 2000 precession quantities, Astronomy & Astrophysics, Vol. 412 (**2003**) 2 567–586, doi: 10.1051/0004-6361:20031539.

Chao, B.F., Dong, D.N., Liu, H.S., Herring, T.A., Libration in the Earth's Rotation, Geophysical Research Letters, Vol. 18 (**1991**) 2007–2010, doi:10.1029/ 91GL02491.

Chao, B.F., Ray, R.D., Gipson, J.M., Egbert, G.D., Ma, C., Diurnal/semidiurnal polar motion excited by oceanic tidal angular momentum, Journal of Geophysical Research: Solid Earth, Vol. 101 (**1996**) B9 20151–20163, doi: 10.1029/96JB01649.

Chao, C., The troposphere calibration model for Mariner Mars 1971, JPL Tech. Rep. 32-1587, Jet Propul. Lab., Pasadena, California, USA, **1974**.

Charlot et al., The Third Realization of the International Celestial Reference Frame, Astronomy & Astrophysics, (**2018**), in preperation.

Chen, G., Herring, T.A., Effects of atmospheric azimuthal asymmetry on the analysis from space geodetic data, Journal of Geophysical Research, Vol. 102 (**1997**) B9 20489–20502.

Cheng, D.K., Field and wave electromagnetics, The Addison-Wesley series in electrical engineering, Addison-Wesley, Reading, Massachusetts, USA, **1989**, ISBN 978-0-201-12819-2.

Choi, D.W., Powers, E.J., Bengtson, R.D., Joyce, G., Brower, D.L., Luhmann, N.C., Peebles, W.A., Digital complex demodulation applied to interferometry, Review of Scientific Instruments, Vol. 57 (**1986**) 8 1989–1991, doi: 10.1063/1.1138762.

Cohen, M., Shaffer, D., Positions of Radio Sources from Long-Baseline Interferometry, The Astronomical Journal, Vol. 76 (**1971**) 91–100.

Dach, R., Lutz, S., Walser, P., Fridez, P. (Eds.), Bernese GNSS Software Version 5.2, User manual, Astronomical Institute, University of Bern, Bern Open Publishing, **2015**, ISBN 978-3-906813-05-9, doi:10.7892/boris.72297.

Davis, J., Elgered, G., Niell, A., C.E., K., Ground-based measurements of gradients in the "wet" radio refractivity of air, Radio Science, Vol. 28 (**1993**) 6 1003–1018.

Davis, J., Herring, T.A., Shapiro, I., Rogers, A., Elgered, G., Geodesy by radio interferometry: effects of atmospheric modeling errors on estimates of baseline length, Radio Science, Vol. 20 (**1985**) 6 1593–1607.

Dee, D.P., Uppala, S.M., Simmons, A.J., Berrisford, P., Poli, P., Kobayashi, S., Andrae, U., Balmaseda, M.A., Balsamo, G., Bauer, P., Bechtold, P., Beljaars, A.C.M., van de Berg, L., Bidlot, J., Bormann, N., Delsol, C., Dragani, R., Fuentes, M., Geer, A.J., Haimberger, L., Healy, S.B., Hersbach, H., Hólm, E.V., Isaksen, L., Kållberg, P., Köhler, M., Matricardi, M., McNally, A.P., Monge-Sanz, B.M., Morcrette, J.J., Park, B.K., Peubey, C., de Rosnay, P., Tavolato, C., Thépaut, J.N., Vitart, F., The ERA-Interim reanalysis: configuration and performance of the data assimilation system, Quarterly Journal of the Royal Meteorological Society, Vol. 137 (**2011**) 656 553–597, doi: 10.1002/qj.828.

Defraigne, P., Smits, I., Length of day variations due to zonal tides for an inelastic earth in non-hydrostatic equilibrium, Geophysical Journal International, Vol. 139 (**1999**) 2 563–572, doi:10.1046/j.1365-246x.1999.00966.x.

DeMets, C., Gordon, R.G., Argus, D.F., Stein, S., Effect of recent revisions to the geomagnetic reversal time scale on estimates of current plate motions, Geophysical Research Letters, Vol. 21 (**1994**) 20 2191–2194, doi:10.1029/94GL02118.

Desai, S.D., Sibois, A.E., Evaluating predicted diurnal and semidiurnal tidal variations in polar motion with GPS-based observations: TIDAL VARIATIONS IN POLAR MOTION, Journal of Geophysical Research: Solid Earth, Vol. 121 (**2016**) 7 5237–5256, doi:10.1002/2016JB013125.

Dickman, S.R., Gross, R.S., Rotational evaluation of a long-period spherical harmonic ocean tide model, Journal of Geodesy, Vol. 84 (**2010**) 7 457–464, doi:10.1007/s00190-010-0383-5.

Dickman, S.R., Nam, Y.S., Revised predictions of long-period ocean tidal effects on Earth's rotation rate, Journal of Geophysical Research: Solid Earth, Vol. 100 (**1995**) B5 8233–8243, doi:10.1029/95JB00028.

Dow, J.M., Neilan, R.E., Rizos, C., The International GNSS Service in a changing landscape of Global Navigation Satellite Systems, Journal of Geodesy, Vol. 83 (**2009**) 3-4 191–198, doi:10.1007/s00190-008-0300-3.

Einstein, A., Die Grundlage der allgemeinen Relativitätstheorie, Annalen der Physik, Vol. 354 (**1916**) 7 769–822, doi:10.1002/andp.19163540702.

Eubanks, T. (Ed.), Proceedings of the U. S. Naval Observatory Workshop on Relativistic Models for Use in Space Geodesy, U. S. Naval Observatory, Washington, D.C., **1991**.

Fey, A., Gordon, D., Jacobs, C., The Second Realization of the International Celestial Reference Frame by Very Long Baseline Interferometry, IERS Technical Note 35, Frankfurt am Main: Verlag des Bundesamts für Kartographie und Geodäsie, **2009**.

Foreman, M., Manual for tidal heights analysis and prediction, Tech. Rep. 77-10, Institute of Ocean Sciences, Department of Fisheries and Oceans, Sidney, Canada, **1977**.

Gasquet, H., Wootton, A.J., Variable-frequency complex demodulation technique for extracting amplitude and phase information, Review of Scientific Instruments, Vol. 68 (**1997**) 1 1111–1114, doi:10.1063/1.1147748.

Golub, G.H., Van Loan, C.F., Matrix computations, 3rd ed., Johns Hopkins studies in the mathematical sciences, Johns Hopkins University Press, Baltimore, USA, **1996**, ISBN 0-8018-5413-X.

Gross, R., Earth Rotation Variations – Long Period, in Treatise on Geophysics, Elsevier, **2015**, pp. 215–261, ISBN 978-0-444-53803-1, doi:10.1016/B978-0-444-53802-4.00059-2.

Gross, R.S., Ocean tidal effects on Earth rotation, Journal of Geodynamics, Vol. 48 (**2009**) 3-5 219–225, doi:10.1016/j.jog.2009.09.016.

Hasan, T., Complex demodulation: Some theory and applications, in Handbook of Statistics, Elsevier, **1983**, Vol. 3, pp. 125–156, ISBN 978-0-444-86726-1, doi: 10.1016/S0169-7161(83)03009-6.

Haykin, S.S., Adaptive filter theory, 5th ed., Pearson, Upper Saddle River, New Jersey, USA, **2014**, ISBN 978-0-13-267145-3.

Hellings, R.W., Relativistic effects in astronomical timing measurements, The Astronomical Journal, Vol. 91 (**1986**) 650, doi:10.1086/114048.

Helmert, F., Die Ausgleichungsrechnung nach der Methode der kleinsten Quadrate, Teubner, Leipzig, **1872**.

Herring, T.A., Modeling atmospheric delays in the analysis of space geodetic data., in J.C. De Munk, T.A. Spoelstra (Eds.), Symposium on Refraction of Transatmospheric Signals in Geodesy, Netherlands Geod. Comm., Delft, Netherlands, **1992**a p. 157–164.

Herring, T.A., Submillimeter horizontal position determination using very long baseline interferometry, Journal of Geophysical Research: Solid Earth, Vol. 97 (**1992**b) B2 1981–1990, doi:10.1029/91jb02649.

Hirvonen, R., Adjustment by least squares in geodesy and photogrammetry, Frederick Ungar Publishing Co. Inc., New York, **1971**, ISBN 0-8044-4397-1.

Hobiger, T., Ichikawa, R., Koyama, Y., Kondo, T., Fast and accurate ray-tracing algorithms for real-time space geodetic applications using numerical weather models, Journal of Geophysical Research, Vol. 113 (**2008**) D20, doi:10.1029/ 2008JD010503.

Hofmann-Wellenhof, B., Lichtenegger, H., Wasle, E., GNSS–global navigation satellite systems: GPS, GLONASS, Galileo, and more, Springer, Wien, Austria, **2008**, ISBN 978-3-211-73012-6.

Hofmeister, A., Böhm, J., Application of ray-traced tropospheric slant delays to geodetic VLBI analysis, Journal of Geodesy, Vol. 91 (**2017**) 8 945–964, doi: 10.1007/s00190-017-1000-7.

IGS, International GNSS Service, Current Network, `http://www.igs.org/ network`, **2019**a, accessed: 05.03.2019.

IGS, International GNSS Service, Products, `http://www.igs.org/products`, **2019**b, accessed: 05.03.2019.

Iribarne, J.V., Godson, W.L., Atmospheric Thermodynamics, Geophysics and Astrophysics Monographs, Vol. 6, D. Reidel Publishing Company, Dordrecht, Netherlands, **1973**.

IVS, International VLBI Service for Geodesy and Astrometry, Observing Programs, `https://ivscc.gsfc.nasa.gov/program/`, **2019**, accessed: 14.03.2019.

Jackson, J.D., Classical electrodynamics, 3rd ed., Wiley, New York, USA, **1999**, ISBN 978-0-471-30932-1.

Kantha, L.H., Stewart, J.S., Desai, S.D., Long-period lunar fortnightly and monthly ocean tides, Journal of Geophysical Research: Oceans, Vol. 103 (**1998**) C6 12639–12647, doi:10.1029/98JC00888.

Kellermann, K.I., Moran, J.M., The Development of High-Resolution Imaging in Radio Astronomy, Annual Review of Astronomy and Astrophysics, Vol. 39 (**2001**) 1 457–509, doi:10.1146/annurev.astro.39.1.457.

Koch, K., Parameter estimation and hypothesis testing in linear models, Springer, Berlin Heidelberg New York, **1988**, ISBN 3-540-18840-1.

Kopeikin, S., Theory of relativity in observational radio astronomy, Sov Astron, Vol. 34 (**1990**) 1 5–10.

Kopeikin, S., Schafer, G., Lorentz covariant theory of light propagation in gravitational fields of arbitrary-moving bodies, Physical Review D, Vol. 60 (**1999**) 12 124002/1–44.

Kouba, J., Improved relativistic transformations in GPS, GPS Solutions, Vol. 8 (**2004**) 3 170–180, doi:10.1007/s10291-004-0102-x.

Kouba, J., Héroux, P., Precise Point Positioning Using IGS Orbit and Clock Products, GPS Solutions, Vol. 5 (**2001**) 2 12–28, doi:10.1007/PL00012883.

Lagler, K., Schindelegger, M., Böhm, J., Krásná, H., Nilsson, T., GPT2: Empirical slant delay model for radio space geodetic techniques: GPT2: EMPIRICAL SLANT DELAY MODEL, Geophysical Research Letters, Vol. 40 (**2013**) 6 1069–1073, doi:10.1002/grl.50288.

Lambert, S., Bizouard, C., Positioning the Terrestrial Ephemeris Origin in the International Terrestrial Reference Frame, Astronomy & Astrophysics, Vol. 394 (**2002**) 1 317–321.

Lambert, S.B., Gontier, A., A Comparison of R1 and R4 IVS Networks, in International VLBI Service for Geodesy and Astrometry, General Meeting Proceedings, **2006** pp. 264–268.

Landskron, D., Böhm, J., VMF3/GPT3: refined discrete and empirical troposphere mapping functions, Journal of Geodesy, Vol. 92 (**2018**) 4 349–360, doi:10.1007/s00190-017-1066-2.

Leandro, R., Langley, R., Santos, M., Estimation of P2-C2 biases by means of Precise Point Positioning, in ION Annual Meeting 2007, **2007** pp. 28–29.

Lewandowski, W., Matsakis, D., Panfilo, G., Tavella, P., The evaluation of uncertainties in [UTC - UTC(k)], Metrologia, Vol. 43 (**2006**) 278–286, doi:10.1088/0026-1394/43/3/010.

Lieske, J.H., Lederle, T., Fricke, W., Morando, B., Expressions for the precession quantities based upon the IAU /1976/ system of astronomical constants, Astronomy & Astrophysics, Vol. 58 (**1977**) 1–16.

Luzum, B., Nothnagel, A., Improved UT1 predictions through low-latency VLBI observations, Journal of Geodesy, Vol. 84 (**2010**) 6 399–402, doi:10.1007/s00190-010-0372-8.

Lyard, F., Lefevre, F., Letellier, T., Francis, O., Modelling the global ocean tides: modern insights from FES2004, Ocean Dynamics, Vol. 56 (**2006**) 5-6 394–415, doi:10.1007/s10236-006-0086-x.

Ma, C., Arias, E.F., Eubanks, T.M., Fey, A.L., Gontier, A.M., Jacobs, C.S., Sovers, O.J., Archinal, B.A., Charlot, P., The International Celestial Reference Frame as Realized by Very Long Baseline Interferometry, The Astronomical Journal, Vol. 116 (**1998**) 1 516–546, doi:10.1086/300408.

MacMillan, D., Atmospheric gradients from very long baseline interferometry observations, Geophysical Research Letters, Vol. 22 (**1995**) 9 1041–1044, doi: 10.1029/95GL00887.

MacMillan, D., Ma, C., Atmospheric gradients and the VLBI terrestrial and celestial reference frames, Geophysical Research Letters, Vol. 24 (**1997**) 4 453–456.

Malkin, Z., On comparison of the Earth orientation parameters obtained from different VLBI networks and observing programs, Journal of Geodesy, Vol. 83 (**2009**) 6 547–556, doi:10.1007/s00190-008-0265-2.

Marini, J., Correction of satellite tracking data for an arbitrary tropospheric profile, Radio Science, Vol. 7 (**1972**) 2 223–231.

Mathews, P.M., Herring, T.A., Buffett, B.A., Modeling of nutation and precession: New nutation series for nonrigid Earth and insights into the Earth's interior: NEW NUTATION SERIES AND THE EARTH'S INTERIOR, Journal of Geophysical Research: Solid Earth, Vol. 107 (**2002**) B4 ETG 3–1–ETG 3–26, doi:10.1029/2001JB000390.

MATLAB, version 9.5 (R2018b), The MathWorks Inc., Natick, Massachusetts, USA, **2018**.

McCarthy, D. (Ed.), IERS Conventions 1996, IERS Techn. Note 21, Central Bureau of IERS, Observatoire de Paris, Paris, France, **1996**.

McCarthy, D.D., Seidelmann, P.K., Time: from Earth rotation to atomic physics, Wiley-VCH, Weinheim, Germany, **2009**, ISBN 978-3-527-40780-4.

Mendes, V.B., Modeling the neutral-atmosphere propagation delay in radiometric space techniques, Ph.D. thesis, University of New Brunswick, Department of Geodesy and Geomatics Engineering, Fredericton, New Brunswick, Canada, **1999**.

Misra, P., Enge, P., Global positioning system: signals, measurements, and performance, 2nd revised ed., Ganga-Jamuna Pr, Lincoln, Massachusetts, USA, **2011**, ISBN 978-0-9709544-2-8.

Montenbruck, O., Hauschild, A., Code biases in multi-GNSS point positioning, in ION ITM 2013, **2013** pp. 616–628.

Moritz, H., Mueller, I.I., Earth rotation: theory and observation, Ungar, New York, USA, **1987**, ISBN 978-0-8044-4671-6.

Munk, W.H., Macdonald, G.J.F., The Rotation of the Earth. A geophyiscal disccusion, Cambridge University Press, New York, USA, **1960**.

Niell, A., Global mapping functions for the atmosphere delay at radio wavelengths, Journal of Geophysical Research, Vol. 101 (**1996**) B2 3227–3246.

Niell, A., Improved atmospheric mapping functions for VLBI and GPS, Earth Planets Space, Vol. 52 (**2000**) 699–702.

Niell, A., Preliminary evaluation of atmospheric mapping functions based on numerical weather models, Phys Chem Earth, Vol. 26 (**2001**) 475–480.

Niemeier, W., Ausgleichungsrechnung, Verlag de Gruyter, Berlin New York, **2002**, ISBN 3110140802.

Nilsson, T., Böhm, J., Schuh, H., Sub-Diurnal Earth Rotation Variations Observed by VLBI, Artificial Satellites, Vol. 45 (**2010**) 2 49–55, doi:10.2478/v10018-010-0005-8.

Nilsson, T., Böhm, J., Schuh, H., Universal time from VLBI single-baseline observations during CONT08, Journal of Geodesy, Vol. 85 (**2011**) 7 415–423, doi:10.1007/s00190-010-0436-9.

Nilsson, T., Heinkelmann, R., Karbon, M., Raposo-Pulido, V., Soja, B., Schuh, H., Earth orientation parameters estimated from VLBI during the CONT11 campaign, Journal of Geodesy, Vol. 88 (**2014**) 5 491–502, doi:10.1007/s00190-014-0700-5.

Nothnagel, A., Schnell, D., The impact of errors in polar motion and nutation on UT1 determinations from VLBI Intensive observations, Journal of Geodesy, Vol. 82 (**2008**) 12 863–869, doi:10.1007/s00190-008-0212-2.

Oppenheim, A.V., Willsky, A.S., Nawab, S.H., Signals & systems, 2nd ed., Prentice-Hall signal processing series, Prentice Hall, Upper Saddle River, New Jersey, USA, **1997**, ISBN 978-0-13-814757-0.

Öztürk, E., Serbetçi, M., Dengeleme hesabı, cilt 2, Karadeniz Technical University, Trabzon, **1989**.

Öztürk, E., Serbetçi, M., Dengeleme hesabı, cilt 3, Karadeniz Technical University, Trabzon, **1992**.

Pelzer, H., Zur Behandlung singulaerer Ausgleichungsaufgaben, ZfV, (**1974**) 181–194.

Petit, G., Luzum, B. (Eds.), IERS Conventions 2010, IERS Techn. Note 36, Verlag des Bundesamts für Kartographie und Geodäsie, Frankfurt am Main, Germany, **2010**, ISBN 3-89888-989-6.

Petrachenko, B., Niell, A., Behrend, D., Corey, B., Böhm, J., Charlot, P., Collioud, A., Gipson, J., Haas, R., Hobiger, T., Koyama, Y., MacMillan, D., Malkin, Z., Nilsson, T., Pany, A., Tuccari, G., A., W., Wresnik, J., Design Aspects of the VLBI2010 System, Progress Report of the IVS VLBI2010 Committee

NASA/TM-2009-214180, International VLBI Service for Geodesy and Astrometry, **2009**.

Petrov, L., Steps towards phase delay VLBI., in W. Schlüter, H. Hase (Eds.), European VLBI for Geodesy and Astrometry, **1999** pp. 144–151.

Petrov, L., Boy, J., Study of the atmospheric pressure loading signal in very long baseline interferometry observations, Journal of Geophysical Research, Vol. 109(B3):B03405 (**2004**), doi:10.1029/2003JB002500.

Povalyaev, A., New Structure for GLONASS Navigation Message, GPS World, Vol. 24 (**2013**) 11 36–38.

Prongle, P., Rayner, A., Generalized invers matrices with applications to statistics, Griffin, London, **1971**.

Rao, C., Mitra, S., Generalized Inverse of Matrices and Its Applications, New York: Wiley, **1971**.

Ray, R.D., Ponte, R.M., Barometric tides from ECMWF operational analyses, Annales Geophysicae, Vol. 21 (**2003**) 8 1897–1910, doi:10.5194/angeo-21-1897-2003.

Ray, R.D., Steinberg, D.J., Chao, B.F., Cartwright, D.E., Diurnal and Semidiurnal Variations in the Earth's Rotation Rate Induced by Oceanic Tides, Science, Vol. 264 (**1994**) 5160 830–832, doi:10.1126/science.264.5160.830.

Richter, G.W., Matzner, R.A., Second-order contributions to relativistic time delay in the parametrized post-Newtonian formalism, Physical Review D, Vol. 28 (**1983**) 12 3007–3012, doi:10.1103/PhysRevD.28.3007.

Robertson, D.S., Carter, W.E., Campbell, J., Schuh, H., Daily Earth rotation determinations from IRIS very long baseline interferometry, Nature, Vol. 316 (**1985**) 6027 424–427, doi:10.1038/316424a0.

Rogers, A.E.E., Very Long Baseline Interferometry with Large Effective Bandwidth for Phase-Delay Measurements, Radio Science, Vol. 5 (**1970**) 10 1239–1247, doi:10.1029/rs005i010p01239.

Rothacher, M., Estimation of station heights with GPS, in H. Drewes, A. Dodson, L. Fortes, P. Sanchez L. Sandoval (Eds.), Vertical reference systems: International Association of Geodesy Symposia, Cartagena, Colombia, February 20-23, 2001, Vol. 124, Springer, Berlin, Germany, **2002**, ISBN 978-3-540-43011-7 pp. 81–90.

Rothacher, M., Beutler, G., Herring, T.A., Weber, R., Estimation of nutation using the Global Positioning System, Journal of Geophysical Research: Solid Earth, Vol. 104 (**1999**) B3 4835–4859, doi:10.1029/1998JB900078.

Rothacher, M., Beutler, G., Weber, R., Hefty, J., High-frequency variations in Earth rotation from Global Positioning System data, Journal of Geophysical Research: Solid Earth, Vol. 106 (**2001**) B7 13711–13738, doi:10.1029/2000JB900393.

Rothacher, M., Springer, T.A., Schaer, S., Beutler, G., Processing Strategies for Regional GPS Networks, in K.P. Schwarz, F.K. Brunner (Eds.), Advances in Positioning and Reference Frames, Vol. 118, Springer, Berlin, Germany, **1998**, ISBN 978-3-642-08425-6 978-3-662-03714-0 pp. 93–100, doi:10.1007/978-3-662-03714-0_14.

Rüeger, J.M., Refractive index formulae for radio waves., in XXII FIG International Congress, Washington DC, USA, **2002**a pp. 1–13.

Rüeger, J.M., Refractive indices of light, infrared and radio waves in the atmosphere, UNISURV report, School of Surveying and Spatial Information Systems, University of New South Wales, Sydney, Australia, **2002**b.

Saastamoinen, J., Atmospheric Correction for the Troposphere and Stratosphere in Radio Ranging Satellites, in S.W. Henriksen, A. Mancini, B.H. Chovitz (Eds.), The use of artificial satellites for geodesy, American Geophysical Union, Washington DC, USA, **1972**, Geophysical Monograph Series, pp. 247–251, ISBN 978-1-118-66364-6, doi:10.1029/GM015p0247.

Saastamoinen, J., Contributions to the theory of atmospheric refraction (in three parts), Bull Geod, Vol. 105, 106, 107 (**1973**) 279–298, 383–397, 13–34.

Sanz Subirana, J., Juan Zornoza, J.M., Hernández-Pajares, M., GNSS Data Processing: Fundamentals and Algorithms, Vol. 1, ESA Communications, Noordwijk, Netherlands, **2013**, ISBN 978-92-9221-886-7.

Schaer, S., Overview of GNSS biases, in IGS Workshop on GNSS Biases, University of Bern, Switzerland, **2012** .

Scherneck, H.G., Explanatory supplement to the section "Local site displacement due to ocean loading" of the IERS Conventions (1996) Chapters 6 and 7, in H. Schuh (Ed.), DGFI Report 71, Deutsches Geodätisches Forschungsinstitut, München, Germany, **1999**, pp. 19–23.

Schlüter, W., Behrend, D., The International VLBI Service for Geodesy and Astrometry (IVS): current capabilities and future prospects, Journal of Geodesy, Vol. 81 (**2007**) 6-8 379–387.

Schmid, R., Dach, R., Collilieux, X., Jäggi, A., Schmitz, M., Dilssner, F., Absolute IGS antenna phase center model igs08.atx: status and potential improvements, Journal of Geodesy, Vol. 90 (**2016**) 4 343–364, doi:10.1007/s00190-015-0876-3.

Schubert, S.D., Rood, R.B., Pfaendtner, J., An Assimilated Dataset for Earth Science Applications, Bulletin of the American Meteorological Society, Vol. 74 (**1993**) 12 2331–2342, doi:10.1175/1520-0477(1993)074⟨2331:AADFES⟩2.0.CO;2.

Schuh, H., Behrend, D., International VLBI Service for Geodesy and Astrometry (IVS), in H. Drewes, H. Hornik (Eds.), Report of the International Association of Geodesy 2007-2009, Travaux de l'Association Internationale de Géodésie, **2009**, Vol. 36, pp. 297–306.

Schuh, H., Behrend, D., VLBI: A fascinating technique for geodesy and astrometry, Journal of Geodynamics, Vol. 61 (**2012**) 68–80, doi:10.1016/j.jog.2012. 07.007.

Schuh, H., Böhm, J., Very Long Baseline Interferometry for Geodesy and Astrometry, in G. Xu (Ed.), Sciences of Geodesy - II: Innovations and Future Developments, Springer Berlin Heidelberg, Berlin, Germany, **2013**, pp. 339–376, ISBN 978-3-642-28000-9, doi:10.1007/978-3-642-28000-9_7.

Schuh, H., Estermann, G., Crétaux, J.F., Bergé-Nguyen, M., van Dam, T., Investigation of Hydrological and Atmospheric Loading by Space Geodetic Techniques, in F. Sansò, C. Hwang, C.K. Shum, J. Li (Eds.), Satellite Altimetry for Geodesy, Geophysics and Oceanography, Springer Berlin Heidelberg, Berlin, Germany, **2003**, Vol. 126, pp. 123–132, ISBN 978-3-642-62329-5 978-3-642-18861-9, doi:10.1007/978-3-642-18861-9_15.

Seeber, G., Satellite geodesy, 2nd ed., Walter de Gruyter, Berlin, Germany, **2003**, ISBN 978-3-11-017549-3.

Seidelmann, P.K., 1980 IAU Theory of Nutation: The final report of the IAU Working Group on Nutation, Celestial Mechanics, Vol. 27 (**1982**) 1 79–106, doi:10. 1007/BF01228952.

Seidelmann, P.K. (Ed.), Explanatory supplement to the Astronomical almanac, rev. ed., University Science Books, Mill Valley, California, USA, **1992**, ISBN 978-0-935702-68-2.

Seidelmann, P.K., Fukushima, T., Why new time scales?, Astronomy & Astrophysics, Vol. 265 (**1992**) 833–838.

Shahid-Saless, B., Hellings, R.W., Ashby, N., A picosecond accuracy relativistic VLBI model via Fermi normal coordinates, Geophysical Research Letters, Vol. 18 (**1991**) 6 1139–1142, doi:10.1029/91GL01187.

Shapiro, I.I., Fourth Test of General Relativity, Physical Review Letters, Vol. 13 (**1964**) 26 789–791, doi:10.1103/PhysRevLett.13.789.

Shapiro, I.I., New Method for the Detection of Light Deflection by Solar Gravity, Science, Vol. 157 (**1967**) 3790 806–808, doi:10.1126/science.157.3790.806.

Shi, J., Gao, Y., A comparison of three PPP integer ambiguity resolution methods, GPS Solutions, Vol. 18 (**2014**) 4 519–528, doi:10.1007/s10291-013-0348-2.

Simon, J.L., Bretagnon, P., Chapront, J., Chapront-Touzé, M., Francou, G., Laskar, J., Numerical expressions for precession formulae and mean elements for the Moon and the planets, Astronomy & Astrophysics, Vol. 282(2) (**1994**) 663–683.

Soffel, M., Müller, J., Wu, X., Xu, C., Consistent relativistic VLBI theory with picosecond accuracy, Astron J, Vol. 101 (**1991**) 6 2306–2310.

Sovers, O., Fanselow, J., Jacobs, C., Astrometry and geodesy with radio interferometry: experiments, models, results, Reviews of Modern Physics, Vol. 70 (**1998**) 4 1393–1453.

Sovers, O., Jacobs, C., Observation model and parameter partials for the JPL VLBI parameter estimation software "MODEST" - 1994, Rev. 5, Vol. 83-39, Jet Propulsion Laboratory, Pasedana, California, USA, **1994**.

Steigenberger, P., Hugentobler, U., Lutz, S., Dach, R., CODE contribution to the IGS reprocessing, Tech. Rep. No. 1, TU München, Institut für Astronomische und Physikalische Geodäsie, München, Germany, **2011**.

Steigenberger, P., Rothacher, M., Dietrich, R., Fritsche, M., Rülke, A., Vey, S., Reprocessing of a global GPS network: REPROCESSING OF A GLOBAL GPS NETWORK, Journal of Geophysical Research: Solid Earth, Vol. 111 (**2006**) B5, doi:10.1029/2005JB003747.

Strang, G., Linear algebra and its applications, 4th ed., Thomson, Brooks/Cole, Belmont, California, USA, **2006**, ISBN 0-03-010567-6.

Takahashi, F., Kondo, T., Takahashi, Y., Koyama, Y. (Eds.), Very long baseline interferometer, Wave summit course, IOS Press Inc., Amsterdam, Netherlands, **2000**, ISBN 978-1-58603-076-6.

Teke, K., Sub-daily parameter estimation in VLBI data analysis, Ph.D. thesis, Vienna University of Technology, Fakultät für Mathematik und Geoinformation, **2011**.

Teke, K., Böhm, J., Madzak, M., Kwak, Y., Steigenberger, P., GNSS zenith delays and gradients in the analysis of VLBI Intensive sessions, Advances in Space Research, Vol. 56 (**2015**) 8 1667–1676, doi:10.1016/j.asr.2015.07.032.

Teke, K., Böhm, J., Spicakova, H., Pany, A., Plank, L., Schuh, H., Piecewise Linear Offsets for VLBI Parameter Estimation, in G. Bourda, P. Charlot, A. Collioud

(Eds.), 19th European VLBI for Geodesy and Astrometry Working Meeting, **2009** pp. 63–67.

Teke, K., Kayıkçı, E.T., Böhm, J., Schuh, H., Modelling Very Long Baseline Interferometry (VLBI) observations, Journal of Geodesy and Geoinformation, Vol. 1 (**2012**) 1 17–26, doi:10.9733/jgg.120512.1.

Thaller, D., Inter-technique combination based on homogeneous normal equation systems including station coordinates, Earth orientation and troposphere parameters, Scientific technical report str08/15, Fakultät für Bauingenieur- und Vermessungswesen der Technischen Universität München, **2008**.

Thaller, D., Krügel, M., Rothacher, M., Tesmer, V., Schmid, R., Angermann, D., Combined Earth orientation parameters based on homogeneous and continuous VLBI and GPS data, Journal of Geodesy, Vol. 81 (**2007**) 6-8 529–541, doi:10.1007/s00190-006-0115-z.

Treuhaft, R., Thomas, J., Incorporating atmospheric delay into the relativistic VLBI time delay, IOM 335 6-91-016, JPL Technical Memorandum, **1991**.

Tsui, J.B.Y., Fundamentals of Global Positioning System Receivers: A Software Approach, Wiley Series in Microwave and Optical Engineering, Wiley, New York, USA, **2000**, ISBN 978-0-471-38154-9.

United Nations, Current and planned global and regional navigation satellite systems and satellite-based augmentation systems of the International Committee on Global Navigation Satellite Systems Providers' Forum, United Nations, New York, USA, **2010**.

Uppala, S.M., KÅllberg, P.W., Simmons, A.J., Andrae, U., Bechtold, V.D.C., Fiorino, M., Gibson, J.K., Haseler, J., Hernandez, A., Kelly, G.A., Li, X., Onogi, K., Saarinen, S., Sokka, N., Allan, R.P., Andersson, E., Arpe, K., Balmaseda, M.A., Beljaars, A.C.M., Berg, L.V.D., Bidlot, J., Bormann, N., Caires, S., Chevallier, F., Dethof, A., Dragosavac, M., Fisher, M., Fuentes, M., Hagemann, S., Hólm, E., Hoskins, B.J., Isaksen, L., Janssen, P.A.E.M., Jenne, R., Mcnally, A.P., Mahfouf, J.F., Morcrette, J.J., Rayner, N.A., Saunders, R.W., Simon, P., Sterl, A., Trenberth, K.E., Untch, A., Vasiljevic, D., Viterbo, P., Woollen, J., The ERA-40 re-analysis, Quarterly Journal of the Royal Meteorological Society, Vol. 131 (**2005**) 612 2961–3012, doi:10.1256/qj.04.176.

Urlichich, Y., Subbotin, V., Stupak, G., Dvorkin, V., Povalyaev, A., Karutin, S., Bakitko, R., Glonass Modernization, GPS World, Vol. 22 (**2011**) 11 34–39.

U.S. Naval Observatory, Current GPS Constellation, `https://tycho.usno.navy.mil/gpscurr.html`, **2019**, accessed: 21.02.2019.

vanDam, T.M., Blewitt, G., Heflin, M.B., Atmospheric pressure loading effects on Global Positioning System coordinate determinations, Journal of Geophysical Research: Solid Earth, Vol. 99 (**1994**) B12 23939–23950, doi:10.1029/94JB02122.

Vey, S., Calais, E., Llubes, M., Florsch, N., Woppelmann, G., Hinderer, J., Amalvict, M., Lalancette, M.F., Simon, B., Duquenne, F., Haase, J.S., GPS measurements of ocean loading and its impact on zenith tropospheric delay estimates: a case study in Brittany, France, Journal of Geodesy, Vol. 76 (**2002**) 8 419–427, doi:10.1007/s00190-002-0272-7.

Wahr, J., Bergen, Z., The effects of mantle anelasticity on nutations, earth tides, and tidal variations in rotation rate, Geophysical Journal International, Vol. 87 (**1986**) 2 633–668, doi:10.1111/j.1365-246X.1986.tb06642.x.

Wahr, J.M., Body tides on an elliptical, rotating, elastic and oceanless earth, Geophysical Journal of the Royal Astronomical Society, Vol. 64 (**1981**a) 3 677–703, doi:10.1111/j.1365-246X.1981.tb02690.x.

Wahr, J.M., The forced nutations of an elliptical, rotating, elastic and oceanless earth, Geophysical Journal of the Royal Astronomical Society, Vol. 64 (**1981**b) 3 705–727, doi:10.1111/j.1365-246X.1981.tb02691.x.

Wallace, P.T., Capitaine, N., Precession-nutation procedures consistent with IAU 2006 resolutions, Astronomy & Astrophysics, Vol. 459 (**2006**) 3 981–985, doi:10.1051/0004-6361:20065897.

Webb, F., Zumberge, J. (Eds.), An Introduction to GIPSY-OASIS II, Report JPLM D-11088, Jet Propulsion Laboratory, Pasadena, California, USA, **1995**.

Weir, M.D., Hass, J., Heil, C. (Eds.), Thomas' calculus, 13th ed., Pearson, Boston, USA, **2014**, ISBN 978-0-321-87896-0.

Wolf, P., Ghilani, C., Adjustment Computations Statistics and Least Squares in Surveying and GIS, John Wiley and Sons Inc. New York, **1997**, ISBN 0-471-16833-5.

Wu, J.T., Wu, S.C., Hajj, G.A., Bertiguer, W.I., Lichten, S.M., Effects of antenna orientation on GPS carrier phase measurements, Manuscripta Geodaetica, Vol. 18 (**1993**) 91–98.

Yoder, C.F., Williams, J.G., Parke, M.E., Tidal variations of Earth rotation, Journal of Geophysical Research: Solid Earth, Vol. 86 (**1981**) B2 881–891, doi:10.1029/JB086iB02p00881.

Zumberge, J., Heflin, M., Jefferson, D., Watkins, M., Web, F., Precise point positioning for the efficient and robust analysis of GPS data from large networks,

HACETTEPE UNIVERSITY
GRADUATE SCHOOL OF SCIENCE AND ENGINEERING
THESIS/~~DISSERTATION~~ ORIGINALITY REPORT

HACETTEPE UNIVERSITY
GRADUATE SCHOOL OF SCIENCE AND ENGINEERING
TO THE DEPARTMENT OF GEOMATİCS ENGINEERING

Date: 18/06/2019

Thesis Title / Topic: ACCURACY ASSESSMENT OF POLAR MOTION AND UNIVERSAL TIME (UT1) OBSERVED BY VLBI AT SUB-DIURNAL PERIODS

According to the originality report obtained by my thesis advisor by using the *Turnitin* plagiarism detection software and by applying the filtering options stated below on 18/06/2019 for the total of 119 pages including the a) Title Page, b) Introduction, c) Main Chapters, d) Conclusion sections of my thesis entitled as above, the similarity index of my thesis is 9 %.

Filtering options applied:
1. Bibliography/Works Cited excluded
2. Quotes excluded
3. Match size up to 5 words excluded

I declare that I have carefully read Hacettepe University Graduate School of Sciene and Engineering Guidelines for Obtaining and Using Thesis Originality Reports; that according to the maximum similarity index values specified in the Guidelines, my thesis does not include any form of plagiarism; that in any future detection of possible infringement of the regulations I accept all legal responsibility; and that all the information I have provided is correct to the best of my knowledge.

I respectfully submit this for approval.

18/06/2019

Name Surname:	Mehmet Fikret Öcal
Student No:	N16127131
Department:	Geomatics Engineering
Program:	Geomatics Engineering
Status:	☒ Masters ☐ Ph.D. ☐ Integrated Ph.D.

ADVISOR APPROVAL

APPROVED.

Assist. Prof. Dr.Kamil Teke

CURRICULUM VITAE

Name, Surname	:	Mehmet Fikret Öcal
Place of Birth	:	Boğazlıyan, Yozgat, TURKEY
Date of Birth	:	20 September 1991
Marital Status	:	Married
Mail Address	:	Geomatics Engineering Department of Hacettepe University, Beytepe, Ankara, TURKEY
Telephone	:	+90 505 487 1552
E-mail	:	fikret.ocal@hacettepe.edu.tr
Foreign Languages	:	English (fluent)

Education

BSc.	:	Hacettepe University, Electrical and Electronics Engineering, Ankara, 2015.
MSc.	:	Hacettepe University, Geomatics Engineering, Ankara, 2019.
PhD.	:	-

Work Experience

2017-...	Research Assistant	Hacettepe University
2016-2018	TUBITAK Project Scholar	Hacettepe University
2016-2016	Electronics R&D Engineer	ATEL Technology and Defence Industry Inc.

Areas of Experiences

Space Geodetic Techniques (VLBI, GNSS), MATLAB, Linux Shell Scripting, Software Defined Radios, Machine Learning, Signal Processing

Publications

Teke, K., **Ocal, M.F.**, Nohutcu, M., Ahi, G.O., VLBI Intensive Oturumlarının Analizi ile Evrensel Zamanın (UT1) İzlenmesi, *Afyon Kocatepe Üniversitesi Fen ve Mühendislik Bilimleri Dergisi*, 17(3):1004-1018, **2017**.

Teke, K., **Ocal, M.F.**, Yüksek-Frekanslı Yer Dönme Parametrelerinin IVS-CONT14 Kampanyasının Analizi ile Kestirimi ve IERS2010 Modeli ile Karşılaştırılması, *Afyon Kocatepe Üniversitesi Fen ve Mühendislik Bilimleri Dergisi*, 17(2):628-637, **2017**.

Kayıkcı, E.T., Teke, K., Karaaslan, O., **Ocal, M.F.**, KTU-GEOD IVS Analysis Center Biennial Report (2015–2016), *In: International VLBI Service for Geodesy and Astrometry 2015 2016 Biennial Report*, Baver, K.D., Behrend, D., Armstrong, K.L. Eds., NASA STI Report Series 238-241, **2017**.

Oral and Poster Presentations

Ocal, M.F., Teke, K., Okyanus Gel-gitleri Kaynaklı Yarı-Günlük ve Günlük Periyotlarda Oluşan Yer Dönüklükleri Değişimi IERS2010 Harmonik Tahmin Modeli Katsayılarının IVS-CONT17 Oturumları Ölçülerinden Kestirimi, *17. Türkiye Harita Bilimsel ve Teknik Kurultayı 25 - 27 Nisan 2019*, Ankara, **2019**.

Altuntas, C., **Ocal, M.F.**, Teke, K., IVS-CONT17 Süresince VLBI ve GNSS (PPP) Tekniklerinden Elde Edilen Günlük Koordinat ve Baz Uzunluğu Tekrarlanabilirlikleri, *17. Türkiye Harita Bilimsel ve Teknik Kurultayı 25 - 27 Nisan 2019*, Ankara, **2019**.

Ocal, M.F., Teke, K., Yer Dönme Parametrelerinin Okyanus Gelgitleri Kaynaklı Güniçi Değişimlerinin VLBI ile İzlenmesi, *72. Türkiye Jeoloji Kurultayı, 28 Ocak - 1 Şubat 2019*, Ankara, **2019**.

Kayıkcı, E.T., Teke, K., Kurt, O., Karaaslan, O., **Ocal, M.F.**, Yavuzdogan, A., Yalcinkaya, M., Türkiye'de Jeodezik VLBI Çalışmaları, *21. Ulusal Astronomi Kongresi, 3 - 7 Eylül 2018*, Kayseri, **2018**.

Ocal, M.F., Teke, K., VLBI Ölçülerinden ve IERS2010 Modelinden elde edilen Yüksek-Frekanslı Yer Dönme Parametrelerinin Karşılaştırılması, *16. Türkiye Harita Bilimsel ve Teknik Kurultayı 3 - 6 Mayıs 2017*, Ankara, **2017**.